# Strong-field ionization of ultracold quantum gases: From ultracold plasma to Rydberg gases

Dissertation
zur Erlangung des Doktorgrades
an der Fakultät für Mathematik, Informatik und
Naturwissenschaften
der Universität Hamburg

vorgelegt von
Mario Sebastian Grossmann
Hamburg
2023

**Gutachter/innen der Dissertation:**

Prof. Dr. Klaus Sengstock
Prof. Dr. Markus Drescher

**Zusammensetzung der Prüfungskommission:**

Prof. Dr. Klaus Sengstock
Prof. Dr. Markus Drescher
Prof. Dr. Andreas Hemmerich
Prof. Dr. Ludwig Mathey
Prof. Dr. Ralf Riedinger

Datum der Disputation: 11. Juli 2023

| | |
|---|---|
| Vorsitzender des Promotionsausschusses Physik: | Prof. Dr. Günter H.W. Sigl |
| Leiter des Fachbereichs Physik: | Prof. Dr. Wolfgang J. Parak |
| Dekan der Fakultät für Mathematik, Informatik und Naturwissenschaften: | Prof. Dr.-Ing. Norbert Ritter |

**Erklärung:**
Hiermit versichere ich an Eides statt, die vorliegende Dissertationsschrift selbst verfasst und keine anderen als die angegebenen Hilfsmittel und Quellen benutzt zu haben.

Hamburg, 31. August 2023

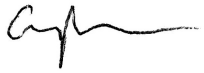

Mario Sebastian Großmann

# Abstract

Combining ultracold quantum gases with femtosecond laser pulses allows for the investigation of fundamental questions regarding atoms in strong light fields, the ultrafast manipulation of coherent matter waves as well as the creation of charged few- to many-body systems via strong-field ionization.

This thesis focuses on such many-body systems with long-range Coulomb interactions triggered by local ionization of a $^{87}$Rb Bose-Einstein condensate (BEC) using femtosecond laser pulses. At a pulse wavelength of 511 nm, the photoelectrons obtain a high excess energy of 0.68 eV, yielding a plasma where the temperature of the electrons is five orders of magnitude larger than the temperature of the ions. Due to the high density inherited from the BEC and the negligible kinetic energy of the atomic ensemble, the plasma exhibits an initially strongly coupled ion component with $\Gamma_\mathrm{i} = 4800$. After ionization, the charge separation and expansion of the system leads to an ultrafast electron cooling, reducing the electron temperature from initially 5250 K to 10 K in less than 500 ns. Molecular dynamics simulations provide insights into the full dynamics and reveal a rapid electron cooling rate of 400 K/ps.

Furthermore, we report on the investigation of the interplay between a highly charged ultracold microplasma and a dense Rydberg gas by tuning the wavelength of the femtosecond laser pulse across the two-photon ionization threshold. Above the threshold, this allows us to tune the initial kinetic energy of the photoelectrons, below the threshold we are able to address Rydberg states down to the $n = 8d$ states.
We experimentally record the electrons from plasma dynamics, three-photon ionization as well as electrons emerging from controlled ionization of Rydberg states and estimate their corresponding energies. Our ion detector provides insight into the Coulomb expansion of the system. Both, above and below the two-photon ionization threshold, we find evidence for the formation of ultracold plasma. Above the threshold, plasma formation from two-photon ionization is expected, yet below the threshold the underlying dynamics differ profoundly. Here, we observe a transfer from excited Rydberg states into ultracold plasma.
The experimental results are complemented by classical molecular dynamics simulations including free ions and electrons as well as bound Rydberg states. Exploiting the small system size, we are able to simulate the dynamics by taking the ionization volume, Rydberg excitation as well as two- and three-photon ionization into account. The simulations reveal that three-photon ionization suppresses recombination processes above the threshold and seeds the formation of an ultracold plasma below the threshold.

# Zusammenfassung

Die Kombination von ultrakalten Quantengasen und Femtosekundenlaserpulsen ermöglicht das Untersuchen von fundamentalen Fragestellungen bezüglich Atomen in starken Lichtfeldern, der ultraschnellen Manipulation von kohärenten Materiewellen und der Erzeugung von Wenig- bis Vielteilchensystemen aus Ladungsträgern mittels Starkfeldionisation.

Der Schwerpunkt dieser Arbeit liegt auf solchen Vielteilchensysteme mit langreichweitiger Coulombwechselwirkung, die durch lokale Ionisation eines $^{87}$Rb Bose-Einstein-Kondensat mittels Femtosekundenlaserpulsen erzeugt werden. Die Photoelektronen haben bei einer Pulswellenlänge von 511 nm eine Überschussenergie von 0.68 eV, was zur Bildung eines Plasmas führt, in dem die initiale Elektronentemperatur fünf Größenordnungen über der Ionentemperatur liegt. Aufgrund der hohen Dichte und der vernachlässigbaren kinetischen Energie der Atome, weist das Plasma anfangs eine stark gekoppelte Ionenkomponente mit einem Kopplungsparameter von $\Gamma_\mathrm{i} = 4800$ auf. Nach der Ionisation führen Ladungstrennung und Expansion des Systems zu ultraschnellem Elektronenkühlen. Hierbei wird die Elektronentemperatur von anfangs 5250 K innerhalb von weniger als 500 ns auf 10 K reduziert. Molekulardynamiksimulationen ermöglichen uns tiefere Einblicke in die Dynamik des Systems und zeigen eine Elektronenkühlrate von 400 K/ps.

Des Weiteren wird das Zusammenspiel zwischen dem ultrakalten Mikroplasma mit großem Ladungsungleichgewicht und dichten Rydberggasen untersucht, indem die Wellenlänge des Femtosekundenlaserpulses über die Zwei-Photonen-Ionisationsschwelle hinaus durchgestimmt wird. Somit lässt sich oberhalb der Ionisationsschwelle die Überschussenergie der Photoelektronen variieren und unterhalb der Schwelle können Rydbergzustände hinunter bis zum $n = 8d$ - Zustand angeregt werden.
Die Detektion von Elektronen, die an der Plasmadynamik teilnehmen, sowie von Elektronen, die aus Drei-Photonen-Ionisation stammen oder durch kontrollierte Ionisation der adressierten Rydbergzustände erzeugt werden, erlaubt uns eine Abschätzung ihrer kinetischen Energien. Der Ionendetektor am Experiment gibt zusätzlich Einblicke in die Coulombexpansion des Systems. Sowohl unter als auch oberhalb der Zwei-Photonen-Ionisationsschwelle beobachten wir die Entwicklung ultrakalter Plasmen. Über der Schwelle ist die Enstehung von Plasmen aufgrund der Zwei-Photonen-Ionisation zu erwarten, unter der Schwelle ergibt sich eine fundamental andere Dynamik - hier beobachten wir einen Transfer von angeregten Rydbergzuständen in ein ultrakaltes Plasma.
Die experimentellen Ergebnisse werden durch klassische Molekulardynamiksimulationen ergänzt, die sowohl freie Ionen und Elektronen als auch gebundene Rydbergzustände enthalten. Aufgrund der geringen Anzahl an involvierten Teilchen kann die zugrundeliegende Dynamik bei gleichzeitiger Berücksichtigung des Ionisationsvolumens, der Rydberganregung und der Zwei- und Drei-Photonen-Ionisation reproduziert werden. Die

Simulationen zeigen dabei, dass Drei-Photonen-Ionisationsprozesse in den beobachteten Systemen über der Zwei-Photonen-Ionisationsschwelle die Rekombination von freien Elektronen und Ionen in Rydbergzustände verhindern, während sie unter der Schwelle die Bildung von ultrakalten Plasmen aus vorhandenen Rydbergatomen begünstigen.

# Contents

# 1 Introduction

*Haiku*
A hole in a cloud
Filled with opposite partners
A loosely bound dance

Since the first experimental realizations of Bose-Einstein condensates (BEC) in the 90s [1–3], ultracold quantum gases have evolved into a major platform for quantum simulation as envisioned by Richard Feynman [4].
While first experiments focused on the fundamental properties of these coherent macroscopic ensembles of atoms demonstrating matter wave interference [5] and excitation properties [6], the rapid developments in experimental techniques now enable us to use them as a toolbox with an extraordinary degree of control. Feshbach resonances can be used to arbitrarily tune from attractive to repulsive interatomic interaction [7], while the dipole interaction of Rydberg states and the associated blockade effect sets the ground for quantum information technologies [8].
Setups of interfering laser beams form optical lattices replicating the periodic structures in solid state systems [9, 10]. From first experiments demonstrating the quantum phase transition from a coherent superfluid to a Mott insulator [11, 12] to the utilization of periodic lattice driving to specifically tailor the properties of the underlying Hamilitionian in the Floquet formalism [13], ultracold atoms in optical lattices have evolved into a powerful tool for quantum simulation.
In the last two decades single-site resolution in optical lattices was achieved by the development of quantum gas microscopes [14–16] and imaging procedures which exploit matter wave optics to magnify the density distribution of the atomic cloud [17]. Another recent advancement in the imaging of ultracold atoms uses charged particle optics in ion microscopes, circumventing the fundamental limit to the optical resolution given by the wavelength of the imaging light [18, 19].
The advent of pulsed laser sources is another breakthrough in experimental physics [20]. The technologies of chirped-pulse amplification [21] and Kerr-lens mode-locking [22] enables probing of ultrafast dynamics on unprecedented timescales as well as light-matter interaction in the strong-field regime.
The use of few-cycle pulses in and near the visual range in pump-probe experiments allows to resolve chemical reactions on femtosecond timescales opening the field of femtochemistry [23, 24]. This time resolution can be further improved to attosecond resolution [25] for light in the XUV to X-ray range granting access to the electron dynamics in atomic systems [26, 27].
Besides the innovations in performing time-resolved measurements, ultrashort laser pulses also provide very high peak intensities exceeding the peak intensities of con-

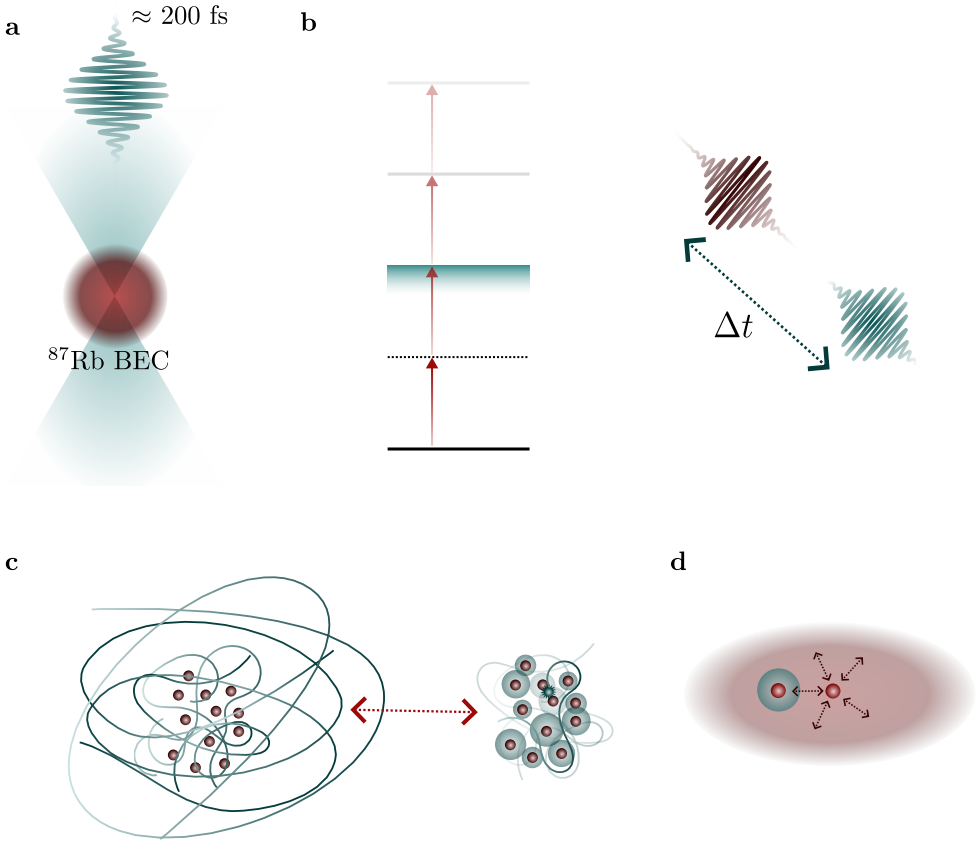


**Fig. 1.1: Combining femtosecond laser pulses with ultracold quantum gases.**
**a.** A laser pulse with a pulse duration of ≈200 fs is focused into a $^{87}$Rb Bose-Einstein-Condensate combining the advantages of a coherent macroscopic ensemble of atoms as a very pure target with negligible kinetic energy with the unique properties of strong coherent light fields in ultrashort laser pulses. **b.** Exposing ultracold atoms to strong light fields allows the investigation of strong field ionization. In the regime accessed during the work of this thesis the dominating mechanism is multi-photon ionization. Besides strong field physics, ultrashort laser pulses provide a powerful toolbox for time-resolved measurements. Due to their ultrashort duration, they allow for instantaneous triggering of complex ultrafast dynamics and pump-probe experiments granting access to time-resolved measurements with femtosecond resolution. **c.** Excitation of a large number of ultracold atoms with ultrashort laser pulses allows the investigation of ultracold plasma, dense Rydberg gases and the transition between these two systems. **d.** By ionizing single atoms in a BEC, hybrid atom-ion quantum systems are in reach. The interaction between the ultracold atoms and the ions can be further manipulated by dressing the BEC with Rydberg states.

tinuous wave lasers by orders of magnitude. The electric fields in these pulses can be comparable or even larger than the electric field between an electron and the ionic core within an atom [28].
Experiments and theoretical considerations concerning noble gases in strong laser fields [29, 30] have elaborated on strong-field ionization processes like multiphoton ionization, above threshold ionization (ATI) and tunneling ionization. However, the study of al-

kali metals subjected to strong laser fields, has been a more recent advancement [31–33].

Ionization of an ensemble of ultracold atoms can lead to the creation of an ultracold plasma and allows for the investigation of many-body systems with long-range Coulomb interactions. The study of ultracold neutral plasma ionized from ultracold atoms in a magneto-optical trap has become an active field of research [34, 35] since the first experiments performed at the end of the 90s [36]. In these systems, ion and electron temperatures below 10 K can be achieved, while the density of the plasma is inherited from the target yielding unconfined plasma systems with lifetimes on the order of 100 µs.
Of particular interest is the regime of strongly coupled plasma. Here, the Coulomb interaction between the ions predominates over the thermal energy. Strongly coupled one-component plasma can for example be used as model systems to describe the crust of a neutron star [37]. The predicted crystallization [38] for strong ion coupling has been realized in one-component systems consisting of confined ions exhibiting a transition from a liquid phase to a Coulomb crystal [39–41] as well as in experiments using dusty plasmas consisting of charged fine particles [42].
In the aforementioned ultracold neutral plasma the ion coupling is limited due to disorder induced heating [34, 43] and so far this has prevented the realization of similarly strongly coupled systems. To counteract the decrease of the coupling by unwanted heating, recent efforts employed laser cooling of the ion component in the plasma [44]. By tuning the wavelength of the ionizing laser pulse the temperature of the electron component can be controlled. At low electron temperatures Rydberg recombination by three-body-collisions becomes relevant and leads to heating of the remaining electron gas [45].

Tremendous progress has been made in trapping, cooling and controlling single to few ions since the invention of Penning and Paul traps [46, 47]. Laser cooling of the trapped ions allowed to reach temperatures on the order of a few millikelvin [48–50], yet the minimal temperature of the trapped ions is still limited by the persisting micromotion in these state-of-the-art techniques.
In the past two decades, the use of ultracold buffer gases to further cool the ions, has pushed the quantum limit of atom-ion s-wave-scattering into reach [51, 52]. While cooling an ion with a buffer gas of the same species is expected to be limited to a temperature above the s-wave-scattering regime [53, 54], the use of heavy ions (e.g. $Yb^+$) combined with a buffer gas of light atoms (e.g. Li) can bypass this restriction [55, 56]. Lately, atom-ion feshbach resonances between a single $^{138}Ba^+$ ion and ultracold $^6Li$ atoms have been reported [57].
Besides cold atom-ion collisions, hybrid quantum systems consisting of ultracold atoms and single to few ions [58, 59] have experienced a growing interest from the realization of ion-Rydberg molecules with bond length of several micrometers [60] to the transport of an ion through a BEC [61]. Theoretical treatment of single ions in a BEC [62–65], the prediction of polaron formation [66], proposals to tune the interaction between the atoms and ions by using the large dipole moment of an atom in a Rydberg state [67] and sophisticated schemes to implement quantum-gates using the interaction between cold atoms in a lattice and a trapped ion [68] have been conceived and complement

recent experimental efforts.

The work presented in this thesis focuses on combining a $^{87}$Rb Bose-Einstein condensate with femtosecond laser pulses (see figure 1.1a). Here, the ultracold quantum gas serves as a pure atomic sample with negligible kinetic energy. The ultrashort laser pulses allow for local ionization of a part of the atoms via multiphoton ionization on timescales that can be considered instantaneous for all unfolding dynamics (see figure 1.1b).
By ionizing a few hundred to thousand atoms in a BEC, we create micrometer sized plasma systems showing an unprecedented ultrafast electron cooling [69]. Here the density inherited from the BEC exceeds the density in ultracold neutral plasma created from magneto-optical traps [36] by orders of magnitudes. Also, the geometry of the microplasma is distinctively non-Gaussian due to the cylindrical ionization volume originating in the non-linear ionization probability of two-photon ionization and the Thomas-Fermi density profile of the condensate in a crossed dipole trap. The relatively small number of particles involved in the dynamics enable us to compare the experimental results to molecular dynamics simulations and reproduce the dynamics at a microscopic level and picosecond timescales. The small system size and density of these microplasmas opens up a new regime between ultracold neutral plasma ionized from a magneto-optical trap [34–36] and ionized nanoclusters [70–72].
When the wavelength of the femtosecond laser pulse is tuned below the two-photon ionization threshold, dense Rydberg samples can be created by ultrafast Rydberg excitation [73] which self-ionize depending on the principal quantum number and in turn form an ultracold plasma (see figure 1.1c) [74–77]. Here, the large bandwidth of the femtosecond laser pulses allows to circumvent the Rydberg blockade that prevents the excitation of multiple Rydberg atoms in dense atomic targets with narrow-bandwidth lasers.
Ionizing single atoms in a BEC with ultrashort laser pulses can be used to create hybrid quantum systems (see figure 1.1d), since the ions created in such a manner exhibit temperatures on the order of 1 mK comparable to the temperatures of a laser-cooled ion in a Paul trap. Yet the absence of a Paul trap eliminates the heating associated with the micromotion in such traps providing a completely new approach to reach the quantum limit for atom-ion interactions.

## 1.1 Structure of this thesis

This thesis is structured into three main chapters and an outlook in the following manner:

- **Chapter 1** contains the introduction and structuring of the thesis.
- **Chapter 2** gives an overview of the experimental apparatus used to investigate the combination of an ultracold ensemble of $^{87}$Rb with femtosecond laser pulses. The main focus of the chapter lies on the improvements made to the existing setup including the implementation of a Λ-enhanced gray molasses as well as optical improvements to the beamline of the femtosecond laser and the introduction of a

more precise synchronization and timebase of the experiment. The chapter closes with a thorough study of the setup for (time-resolved) charged particle detection used to image the electrons and ions emerging from ionization events triggered by the ultrashort laser pulse.

- **Chapter 3** presents the results regarding a highly charged microplasma created by local ionization of a $^{87}$Rb Bose-Einstein condensate with a femtosecond laser pulse with a wavelength of 511 nm. We present the unique properties of the microplasma created at our experiment and our methods to reproduce the underlying dynamics in molecular dynamics simulations with excellent agreement to our experimental data followed by an in-depth analysis of the unprecedented ultrafast electron cooling observed in these systems.

- **Chapter 4** elaborates on the ultracold microplasma when the initial kinetic energy of the electrons emerging from the ionization process is varied by tuning the wavelength of the femtosecond laser pulse across the two-photon ionization threshold. This allows us to study the smooth transition from an ultracold plasma to a dense Rydberg gas. A summary of the motivation and experimental conditions is followed by a thorough analysis of the experimental data. We are able to isolate electron signatures for three-photon ionization, plasma dynamics and Rydberg excitation, while the recorded ion signal gives insight into the Coulomb energy in the system. The discussion of the experimental results is complemented by a detailed study of the underlying dynamics using classical molecular dynamics simulations including bound states between single ions and electrons as a model for Rydberg atoms. The simulations comprise simple model systems as well as full simulations of the conditions in the experiment.

- **Chapter 5** gives a outlook on future experiments regarding the ultracold microplasma and transition to Rydberg gas transcending the well-known regime of ultracold neutral plasma, as well as hybrid quantum systems realized by ionizing single atoms. The chapter concludes with a brief introduction of the new detector setup, that is currently installed at the experiment [78].

# 2 Upgrades to the experimental setup of the *Ultracold and Ultrafast* project

Investigating hybrid systems consisting of ultracold atoms and ions requires experiments that are specifically designed for this challenging task.
The experimental work in this thesis has been carried out at such an experiment employing local photoionization of a $^{87}$Rb Bose-Einstein-Condensate (BEC) via tunable femtosecond laser pulses. A comprehensive description of the machine can be found in the PhD-thesis of Tobias Kroker [69].
This chapter focuses on the recent improvements made to the existing setup, however a short introduction to the existing machine can be found in section 2.1. Section 2.2 describes the implementation of a gray molasses for $^{87}$Rb. Minor changes to the beamline of the femtosecond laser greatly improved the available laser power at the experiment and can be found in section 2.3. In an effort to better capture the dynamics of the observed systems, the synchronization and timebase of the setup was refined, the details are explained in section 2.4. The last section 2.5 revolves around the apparatus for time-resolved imaging of the charged ionization products, deepening the understanding of our recorded electron and ion images.
The gray molasses was set up with Linn Hamester. Julian Fiedler contributed to the optimization of the new cycle, the focusing optics and pulse pickup of the femtosecond laser system, the synchronization and time base as well as the time-resolved detection for the ions. The framework for the COMSOL Multiphysics® simulations for the detector setup was developed in close cooperation with Tobias Kroker. The time-resolved charge particle detection was set up in cooperation with Tobias Kroker and improved upon with contributions from Julian Fiedler.

## 2.1 The *Ultracold and Ultrafast* experiment

The *Ultracold and Ultrafast* experiment is based on a quantum gas machine for $^{87}$Rb combined with a tunable femtosecond laser system for photoionization of the ultracold atoms.
As stated above an in-depth discussion of the experiment can be found in the PhD thesis of Tobias Kroker [69] and early stages of the design are already discussed in the PhD thesis of Bernhard Ruff [79] while details to various key systems are explicated in a number of bachelor [80–87], master [88–91] and diploma [92] theses.
Figure 2.1 shows the vacuum chambers of the experiment and a brief description of the experimental cycle. The general vacuum setup can be split into two parts: in the first part the preparation of the atomic target takes place and the $^{87}$Rb atoms get cooled to near-quantum degeneracy. Since the employed techniques require magnetic fields and also occupy most of the viewports to the vacuum chamber, detection of charged

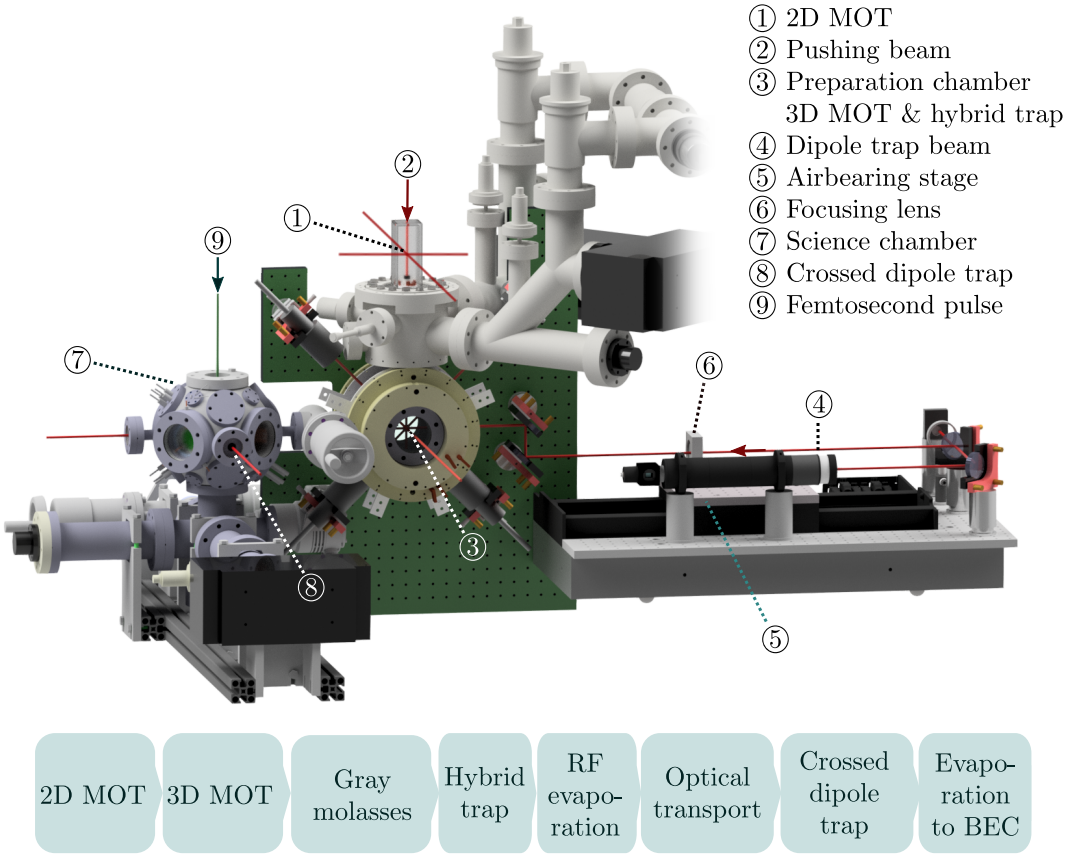


**Fig. 2.1: Vacuum chambers of the *Ultracold and Ultrafast* quantum gas machine.** In the glass cell at the top of the setup, a thin vapor of Rubidium is released into the vacuum by alkali metal dispensers. A continuous 2D-MOT precools the atoms in a vertically elongated volume which is overlapped with a near-resonant pushing beam. This pushing beam transports the atoms through a differential pumping stage into the central chamber where a 3D-MOT traps and cools the atoms. A gray molasses scheme then cools the atoms to sub-Doppler temperatures. The ultracold ensemble is loaded into a hybrid trap which consists of a magnetic trap provided by water cooled copper coils outside the vacuum chamber and a superimposed dipole trap beam. After forced radio frequency evaporation the sample is transported into the science chamber by moving the focus of the dipole trap beam via an airbearing stage. In the science chamber a second dipole trap beam perpendicular to the transport beam is switched on. In this crossed dipole trap the sample can be evaporated to quantum degeneracy, eventually yielding a $^{87}$Rb BEC.

particles and neutral atoms is not feasible at this point. Therefore, we transport the atoms with optical tweezers into a spatially separated second chamber, where we have excellent control over electric and magnetic fields and sufficient optical access for trapping, ionization and absorption imaging.
Starting with $^{87}$Rb atoms dispersed in the top-most glass chamber, a continuous 2D-

MOT is used to precool and capture the atoms in a vertically elongated volume. A near-resonant pushing laser beam overlayed onto the 2D-magneto optical trap (MOT) then pushes these atoms through a differential pumping stage down into the preparation chamber where a 3D-MOT [93] is used to further cool and trap the ensemble.
A gray molasses provides cooling to sub-Doppler temperatures before the atoms are transferred into a hybrid trap [94] consisting of a quadrupole magnetic trap realized through water cooled copper coils outside the chamber and an optical dipole trap at 1064 nm. The focusing lens for the dipole trap is set up on an air bearing translation stage to allow using the trapping beam as optical tweezers.
In the hybrid trap the ensemble's temperature is further reduced by forced radio frequency evaporation [95] provided by a small loop antenna attached to the window of the chamber. Afterwards, the optical tweezers are used to transport the cold atoms into the science chamber by simply moving the focusing lens of the optical dipole trap. This shifts the focus of the beam and thus the trapping potential for the atoms from one chamber to the next.
In the science chamber, a second dipole trap beam is ramped up providing a spherically symmetric trapping potential in the center of the chamber. By exponentially decreasing the laser power in the crossed dipole trap, the cold atomic ensemble is evaporated to quantum degeneracy and eventually forms a BEC.
Within the science chamber the ultracold atoms can be observed via absorption imaging after time-of-flight. A tunable femtosecond laser pulse can be applied through a microscope objective with a small focus of $w_0 \approx 1\,\mu\text{m}$. The arising high peak intensities in a small volume of the target lead to local photoionization of a few hundred to several thousand atoms by multi-photon ionization. Figure 2.2 illustrates the possible multiphoton processes for 511 nm as well as 593.7 nm. For a two-photon process the former wavelength yields electrons with a relatively high excess energy of 0.68 eV, the latter leads to vanishing excess energy. Yet, the pulses used in the experiment at 593.7 nm wavelength have a pulse duration of only 166(30) fs [96] and thus the excess energy at the two-photon ionization threshold is limited by two times the spectral width of $2 \times \sigma_E = 9.1\,\text{meV}$ corresponding to a minimal electron temperature of 70.4 K. Processes involving more photons are less probable in the accessible intensity regime. However, three-photon processes with 3.1 eV at 511 nm or respectively 2.1 eV at 593.7 nm can also be observed at our experiment.
The charged particles created in these ionization processes can be observed with the detector setup shown in the cut through the science chamber illustrated in figure 2.3. To avoid accumulating charges on the glass surface of the re-entrant viewport that houses the focusing microscope objective by the ionization products, it is shielded by a grounded and gold plated copper mesh. Two similar extraction meshes installed symmetrically to both sides of the central interaction region and set to voltages typically between $\pm V_{\text{ext}} = \pm 5\,\text{V}$ to 300 V draw the electrons and ions to their corresponding detectors on opposite sides of the chamber. The electron and ion detectors itself consist of microchannel plate detectors (MCPs) combined with phosphor screens. Inciding particles on the MCP result in an avalanche of electrons triggering a small flash of light on the phosphor screen which then can be recorded by highspeed cameras outside of the vacuum chamber.

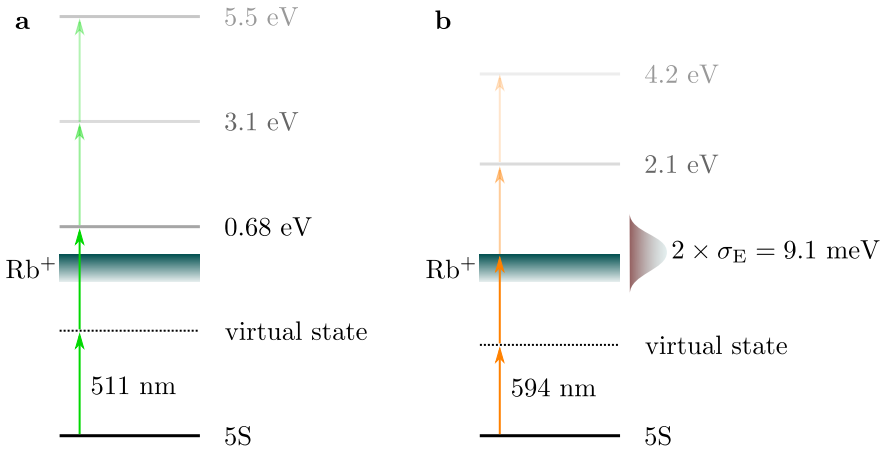


**Fig. 2.2: Multiphoton ionization of $^{87}$Rb.**
**a.** At 511 nm $^{87}$Rb can be ionized via a non-resonant two-photon process resulting in an excess energy of 0.68 eV. This excess energy is mostly imposed as kinetic energy on the electrons due to the high mass ratio between the ions and electrons. Further above-threshold-ionization-processes (ATIs) are less probable. However, the signature of the three-photon process at 3.1 eV can still be observed in our experiments.
**b.** A decrease of the excess energy of the ionization products can be achieved by tuning the wavelength of the ionizing laser pulse. For a two-photon process the ionization threshold would correspond to a wavelength of 593.7 nm. The excess energy is then determined by two times the spectral bandwidth $\sigma_E$ of the femtosecond laser pulse, which in this case amounts to 9.1 meV.

## 2.2 Implementation of gray molasses cooling

The fundamental temperature limit of a 3D-MOT is given by the Doppler limit $T_D = \hbar\Gamma/(2k_B) \approx 146\,\mu K$ (for $^{87}$Rb), where $\hbar$ is the reduced Planck constant, $k_B$ is the Boltzmann constant and $\Gamma$ the atomic line width of the transition used for the cooling light. To overcome this limit, sub-Doppler cooling schemes are necessary. In the past, we used a bright molasses to reach temperatures of 47(1) µK [87]. In this section we discuss the implementation of gray molasses cooling.

### 2.2.1 Sisyphus cooling

Subceeding the Doppler limit in a molasses setup is made possible by an effect referred to as Sisyphus-cooling [97]. This effect can be illustrated by means of a simplified 1D-model (see figure 2.4a ): Let us assume our 1D-molasses is formed by two counter propagating beams along the $z$-axis with perpendicular linear polarizations. In this case there is no spatial interference of the intensity of the two beams, however the polarization of the light field oscillates between $\sigma^-$ and $\sigma^+$ over a distance of $\lambda/2$ (where $\lambda$ is the wavelength of the laser in use). This spatial oscillation of the polarization leads to a spatially oscillating AC-Stark energy shift of the hyperfine states $|\pm 1/2\rangle$.
Let us observe an atom in the $|+1/2\rangle$-state moving along the $z$-axis. This atom has to expend kinetic energy to climb the potential hill of the oscillating energy shift. Arriving at the top of the potential hill, the polarization of the light field at this point ($\sigma^-$) allows the atom to get pumped into the $|-1/2\rangle$-hyperfine state of the excited state from which

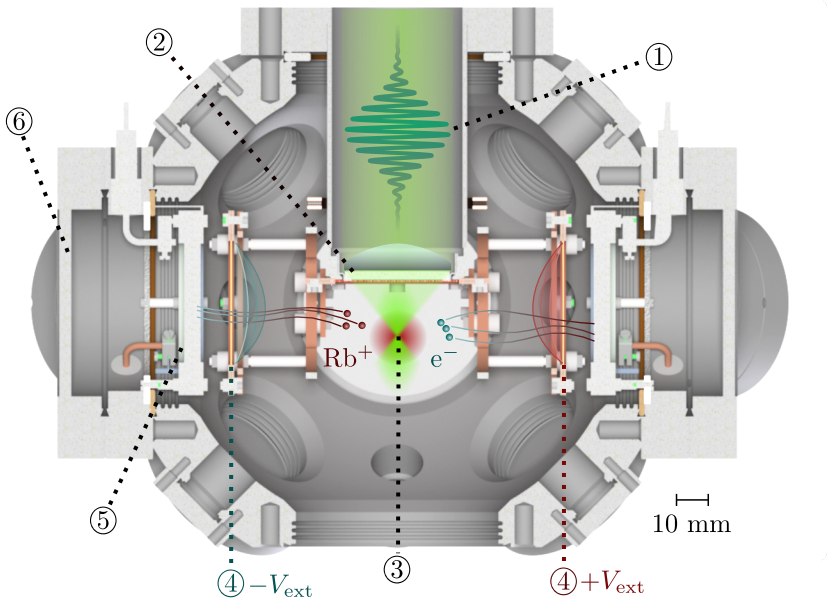


① Focusing objective in re-entrant viewport, ② Grounded mesh,
③ Ultracold $^{87}$Rb, ④ Extraction mesh,
⑤ MCP with phosphor screen, ⑥ Viewport

**Fig. 2.3: Detector setup inside the science chamber.**
In the center of the chamber the ultracold $^{87}$Rb target is overlapped with a femtosecond laser pulse entering from above. The pulse is applied through a microscope objective located in a re-entrant viewport and locally ionizes a fraction of the atoms in the ultracold atomic cloud within a focus with a waist of $w_0 \approx 1\,\mu\text{m}$ . A grounded copper mesh right beneath the re-entrant viewport prevents the accumulation of charge on the glass surface. Extraction meshes set to $\pm V_{\text{ext}}$ draw the emerging ions and electrons to opposite sides of the chamber where they can be detected by microchannel plate detectors with phosphor screens.

it can fall back into the $|-1/2\rangle$-hyperfine ground state. Like its mythical counterpart Sisyphus, it now has to start again at the foot of the hill. The loss of kinetic energy on the way up the potential hills over many cycles leads to an effective cooling of the atoms and a final temperature below the Doppler limit.
An improvement to the bright molasses is the gray molasses (see figure 2.4b) [98–100]. If we stay within our simplified model, the only thing that we have to add is a dark state $|\text{dark}\rangle$ which does not couple to the light field. While the principle of Sisyphus cooling still applies, an atom that gets pumped into the excited state, can now also fall back into the dark state and decouple from the light field.
However, atoms in the dark state are not lost to the molasses: If they are still moving fast enough along $z$ they can overcome the small energy gap between $|\text{dark}\rangle$ and the minima of $|\pm 1/2\rangle$ via a motional Landau-Zener transition and get back into the cooling cycle. Cold and thus slow atoms will remain in the dark state and - being decoupled from the light field - experience no unwanted heating such as spontaneous scattering, allowing even lower temperatures.

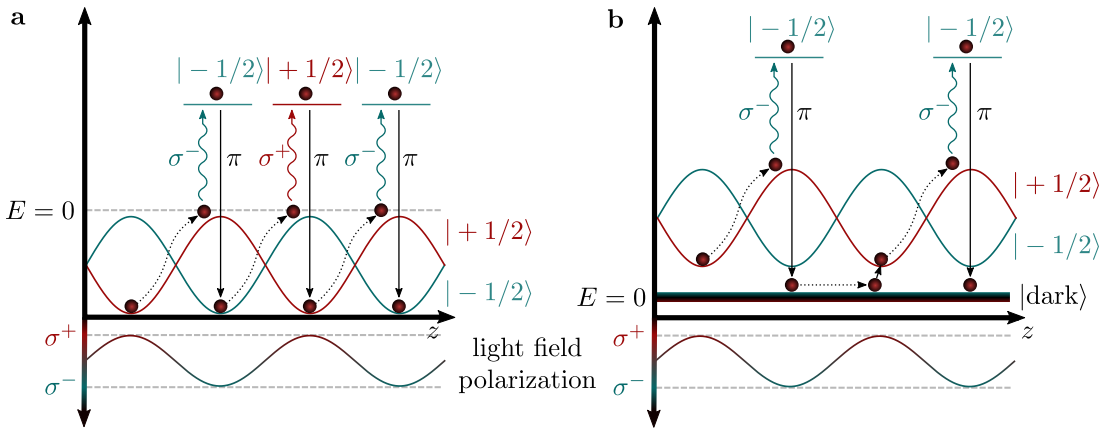


**Fig. 2.4: Sisyphus cooling in a bright and gray molasses.**
**a.** In a simplified 1D-model two counter propagating laser beams with perpendicular linear polarization form a bright molasses with a polarization lattice that spatially oscillates between $\sigma^+$ and $\sigma^-$. This leads to an oscillating AC-Stark shift on the hyperfine states $|\pm 1/2\rangle$. An atom in one of these states moving along the $z$-axis has to expend kinetic energy to climb up the potential hills. At the maximum of the potential the polarization of the light field matches the transition to the other hyperfine state of the excited state and the atom absorbs a photon from the light field. Excited atoms can then fall back into the ground state by spontaneous emission, restarting the process at the foot of the potential hill.
**b.** In a gray molasses the same principle applies, but a dark state is added to the system. After climbing the potential hill and getting pumped into the excited state, atoms can fall back into the dark state where they decouple from the light field. These atoms will re-enter the Sisyphus cooling only if their velocity is high enough to allow a motional Landau-Zener transition from the dark state into one of the potential minima of the bright states, leaving slow and thus cold atoms in the dark state. Since these atoms are decoupled from the light field, they do not experience heating by spontaneous scattering.

### 2.2.2 Λ-enhanced gray molasses for $^{87}$Rb

The first gray or dark molasses cooling schemes have already been proposed and realized more than 15 years ago [98–101]. Implementing a Λ-enhanced gray molasses on the $D_2$-line of $^{87}$Rb however, is a very recent advancement [102]. This method offers a simple upgrade for common $^{87}$Rb quantum gas experiments since the same laser source can be used for the magneto optical trap and the gray molasses.
Following the results of this publication we implemented a Λ-scheme on the $F = 1, 2 \rightarrow F' = 2$ transitions (see figure 2.5a). In this scheme the cooling light drives the $F = 2 \rightarrow F' = 2$ transition while a *coherent* repumper with much lower intensity drives the $F = 1 \rightarrow F' = 2$ transition. Both light sources are blue detuned with the detunings $\Delta_{\mathrm{RP}}$ for the repumper and $\Delta_{22}$ for the cooling light as well as the corresponding Raman-detuning $\delta_{\mathrm{R}} = \Delta_{\mathrm{RP}} - \Delta_{22}$.
This setup yields a gray molasses where the dark states are superpositions of states from both the $F = 2$ and $F = 1$ hyperfine manifolds.
A complete description of a Λ-enhanced gray molasses is not within the scope of this section, since the polarization pattern formed by the six counter propagating beams of a 3D-molasses and the numerous hyperfine states of the transitions involved form a

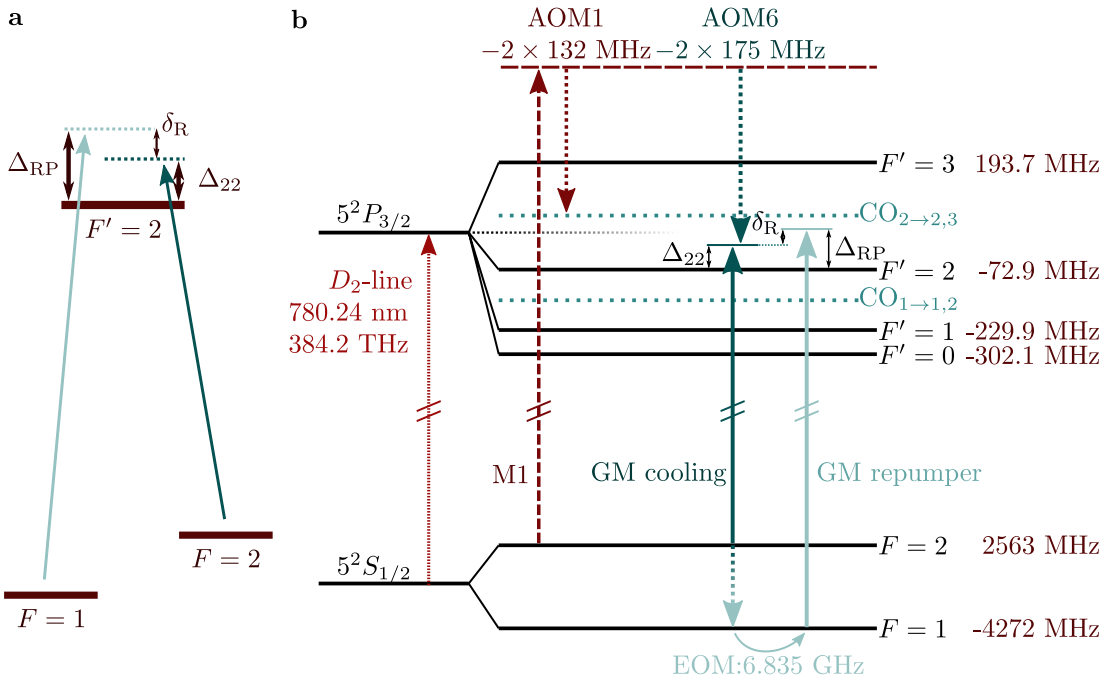


**Fig. 2.5: Implementation of a Λ-enhanced gray molasses cooling for $^{87}$Rb.**
**a.** Realization of the three-level Λ scheme requires simultaneous and coherent driving of the $F = 1 \rightarrow F' = 2$ as well as the $F = 2 \rightarrow F' = 2$ transitions. Both coupling light fields should be blue detuned with $\Delta_{\mathrm{RP}}$ and $\Delta_{22}$ respectively. The difference $\delta_{\mathrm{R}}$ is the Raman-detuning.
**b.** Implementation of the gray molasses in the existing laser system is done by using the master laser M1 that also drives the 3D-MOT cooling. This laser is locked $2 \times 132\,\mathrm{MHz}$ above the $F = 2 \rightarrow F' = 2, 3$ crossover line. For the gray molasses cooling the light from M1 is shifted by AOM6 so that it is blue detuned by $\Delta_{22}$ to the $F = 2 \rightarrow F' = 2$ transition. The low intensity gray molasses repumper is realized by creating sidebands at a frequency offset of $\Delta_{\mathrm{HFS}+\delta_{\mathrm{R}}}$ on the cooling light with a phase modulating EOM.

complex problem to be solved. A still simplified but illustrative model for $^7$Li can be found for example in the publication of A. Grier et al. [103]
Figure 2.5b shows the hyperfine structure of the $D_2$-line of $^{87}$Rb [104] and the implementation of the Λ-scheme from figure 2.5a. We use the same master laser M1 that is already set up and locked for the 3D-MOT (details in [89] and [87]). This laser is locked to the $F = 2 \rightarrow F' = 2, 3$ crossover line. Before going into the spectroscopy setup the light is red-detuning by $2 \times 132\,\mathrm{MHz}$ via an acousto-optic modulator (AOM) in double pass configuration. This results in M1 being blue detuned by $130.7\,\mathrm{MHz}$ to the $F = 2 \rightarrow F' = 3$ transition. To prepare the light for the gray molasses cooling which is blue detuned to $F' = 2$, we employ another AOM in double pass configuration to shift the light from M1 by $-2 \times 175\,\mathrm{MHz}$. Additionally, we use a resonant electro-optic phase modulator (EOM) specifically designed for this purpose[1] to create the coherent sidebands of the gray molasses repumper with a frequency offset from the cooling light by $\Delta_{\mathrm{HFS}+\delta_{\mathrm{R}}} = \delta_{\mathrm{R}} + 6.835\,\mathrm{GHz}$.

[1] Qubig PM-Rb87-6.8M2

The process of optimizing the detunings, intensity and ratio of cooling intensity versus repumper intensity is thoroughly described in [87] and shall not be repeated here. With the bright molasses we used before, we achieved a minimum temperature of 46.87(111) µK with a phase space density of $1.29(32) \times 10^{-6}$. The gray molasses used in the experimental cycle exhibits a temperature of 7.44(50) µK and a phase space density that is a factor five larger with a value of $6.54(68) \times 10^{-6}$. For this we use a molasses duration of 8 ms at detunings of $\Delta_{22} = 8.23\ \Gamma$ and $\delta_R = -0.014\ \Gamma$ where $\Gamma = 6.065$ MHz is the natural width of the $D_2$-line. However, this is not necessarily the coldest and densest gray molasses possible in the setup but the configuration that works best in the cycle, i.e. yields the best loading efficiency into the hybrid trap.

### 2.2.3 Adjustments to the cooling cycle

The increased phase space density and lower temperature after the gray molasses requires a number of changes to the experimental cycle for the preparation of a BEC as characterized in detail in [69]. In a first step the current through the coils of the magnetic trap has to be decreased by more than 40 % from 115 A to 65 A and the cycle adapted accordingly. Before, it was necessary to use two power supplies[2] connected in series to drive the magnetic coils, the reduction in current makes one of these supplies now obsolete. A further advantage is the reduced resistive heating of the magnetic coils increasing stability by decreasing temperature fluctuations. We also expect an increased lifetime of the coils since the water pressure in the housings can be reduced.
The quadrupole magnetic field created by the two coils in anti-Helmholtz configuration can be characterized by the gradients in radial and axial directions. The radial gradient of the magnetic field in the new setup is now 51.4(13) G/cm while the axial gradient is 98.5(5) G/cm. This reduction in gradient also decreases the Zeemann energy splitting of the $m_F$ states within the trap, making it necessary to adapt the frequency sweep for the forced radio frequency evaporation accordingly to an exponential sweep from 9.5 MHz to 2.8 MHz within 4 s. Before an exponential sweep from 30 MHz to 2.8 MHz within 6 s was used.
Figure 2.6 compares the hybrid trap configurations of the previous cycle and the current cycle, beginning directly after the bright or gray molasses, respectively. Besides the aforementioned decrease in current, another major change is the avoidance of a pure magnetic trap-phase. We achieved a better loading efficiency of the magnetic trap when directly activating the tweezer axis of the dipole trap, i.e. directly loading from the gray molasses into a hybrid trap.
The temporal overlap between the optical transport and the amplitude of the exponential intensity ramp of the crossing dipole trap has also been reduced to get a more efficient transfer in the crossed dipole trap. A small asymmetry is introduced to the intensity ramp providing the evaporation to quantum degeneracy, improving its efficiency. This is probably an effect of a slight intensity calibration mismatch between the two beams, originating in the introduction of two dichroic mirrors in the beam line of the dipole trap [105]. The new hybrid trap sequence is 2 s shorter than the old one, the 3D-MOT duration is also reduced by 1 s resulting in an overall reduction in cycle

[2] DELTA Electronica, SM45 - 140

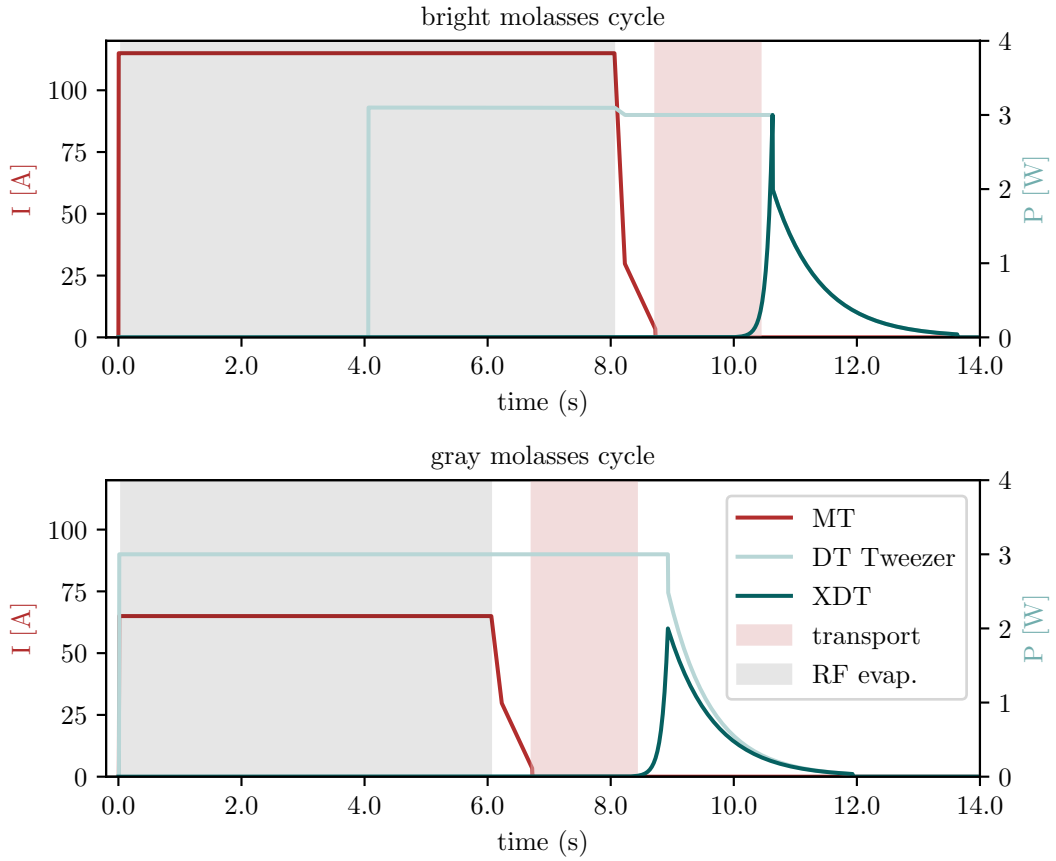


**Fig. 2.6: Comparison of the experimental cycles starting directly after the bright (top figure) and gray (bottom figure) molasses phase.**
The plot shows the current in the coils of the magnetic trap (dark red) and power in the transport beam (light turquoise) and the crossing dipole trap (dark turquoise) in dependency on the time. The shaded regions mark the duration of the forced radio frequency evaporation in the magnetic trap (gray) and the duration of the optical transport (light red).
After implementation of the gray molasses the current driving the magnetic trap could be reduced from 115 A to 65 A. Avoiding the purely magnetic trap by simultaneously switching on the dipole trap tweezer leads to a more efficient loading of the hybrid trap after the gray molasses. Furthermore the duration of the forced radio frequency evaporation was shortened by 2 s and the frequencies adapted according to the reduced Zeemann splitting in the weaker magnetic trap.
The temporal overlap between the exponential increase of power in the crossing dipole trap and the optical transport was reduced for more efficient loading of the crossed dipole trap while a minor asymmetry in the evaporation ramps of the dipole trap branches improved condensation to a BEC probably due to a calibration mismatch between the two beams.

length of 10 %.

## 2.3 Improvements to the femtosecond beamline

To increase the available pulse energy of the femtosecond laser pulses at the experiment the optics that collimate the beam of the existing setup were modified. Furthermore a pulse pickup was installed to get direct access to the intensity and timing of each applied pulse.

### 2.3.1 Femtosecond laser system

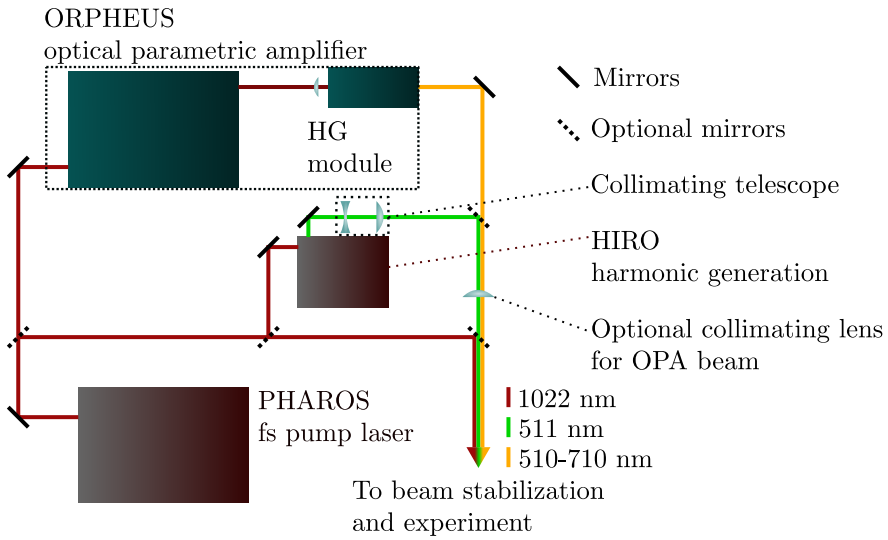


**Fig. 2.7: Overview of the femtosecond laser setup.**
The PHAROS laser provides femtosecond pulses at 100 kHz repetition rate with a wavelength of 1022 nm. Removable mirrors on index mounts allow to use these pulses directly or to route them through either the HIRO or the ORPHEUS module. With the HIRO harmonic generation module the second, third and fourth harmonic of the pump wavelength can be generated. So far, only the second harmonic at 511.4 nm generated by this module has been used at the experiment.
The ORPHEUS optical parametric amplifier can produce light from 210 nm to 2700 nm when combined with the downstream harmonic generation module. In the experiments discussed in this thesis, the second harmonic of the idler is used which covers a range between 510 nm and 710 nm.
Improvements to the beamline focus on the alignment and rebuilding of the collimating telescope for the HIRO and the collimating lense for the beam from the ORPHEUS OPA.

The femtosecond laser pulses used in the experiments are generated by a commercially available laser system[3] which employs Kerr-lens mode-locking and chirped-pulse amplification (CPA). The laser uses an ytterbium doped potassium-gadolinium tungstate oscillator (Yb:KGW) and produces pulses with a wavelength of 1022 nm and a full width at half maximum (FWHM) bandwidth of 4.36 nm. The repetition rate of the oscillator is 83 MHz, however, after the CPA in the regenerative amplifier the pulse repetition rate of the system is set to 100 kHz. A pulse picker allows to generate arbitrary pulse

[3] Light Conversion, PHAROS PH1-06

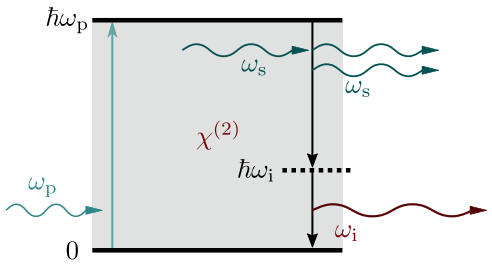


**Fig. 2.8: Illustration of difference frequency generation.**
In an optical parametric amplifier difference frequency generation is used to generate a wide range of wavelengths. A non-linear optical medium is pumped at the frequency $\omega_\mathrm{p}$. Depending on the phase matching condition of the crystal, the pump photon is converted into two photons with $\omega_\mathrm{s}$ and $\omega_\mathrm{i}$. Efficiency of this effect increases, when the crystal is seeded with a weak beam at the frequency $\omega_\mathrm{s}$ (or $\omega_\mathrm{i}$ if the idler is used).

trains within this repetition rate. At full repetition rate the maximum output power is 6 W and the pulse duration is $300^{+30}_{-23}$ fs [69].
Besides the PHAROS femtosecond laser itself, the setup comprises a HIRO harmonic generation (HG) module[4] and an ORPHEUS optical parametric amplifier (OPA) with subsequent HG[5]. The setup of the devices on the optical table can be seen in figure 2.7. So far, mainly the 1022 nm light of the PHAROS itself or the second harmonic at a wavelength of 511.4 nm with a pulse duration of $215^{+20}_{-15}$ fs from the HIRO module have been used for experiments [33, 106]. In most of the recent experimental work described in this thesis, the second harmonic of the idler of the ORPHEUS OPA was used.
The principal of difference frequency generation is illustrated in figure 2.8: A nonlinear optical medium is pumped with photons with angular frequency $\omega_\mathrm{p}$. Depending on the phase-matching (i.e. the angle of the crystal) this photon is converted into a signal photon with angular frequency $\omega_\mathrm{s}$ and an idler photon with $\omega_\mathrm{i}$. Energy conservation requires that $\omega_\mathrm{s} + \omega_\mathrm{i} = \omega_p$. The efficiency of this process can be greatly improved by seeding the medium with a weak signal beam with frequency $\omega_\mathrm{s}$ (or $\omega_\mathrm{i}$ if the idler is used).
In the ORPHEUS system the pump beam is generated by second harmonic generation of the 1022 nm light from the PHAROS. The variable signal wavelength is generated from a white light continuum, and selected by changing the temporal (and thus spectral) overlap of a chirped white light pulse with the pump light pulse in the crystal for the difference frequency generation. To amplify the generated signal and idler pulses, they pass the crystal after difference frequency generation a second time in temporal overlap with a pump pulse using it effectively as a gain medium. A second amplification stage with a separate crystal is used in a single-pass configuration right before the output, in the same manner. Since signal and idler both get amplified in the amplification stages, both can be used in experiments. A HG stage behind the OPA offers further flexibility by allowing to generate the second and fourth harmonic of either signal or idler. Using the second harmonic of the idler, a range of 510 nm to 710 nm with a pulse duration of 166(3) fs (determined at 593.7 nm) [96] can be covered.

[4]Light Conversion, HIRO Customizable Harmonic Generator for PHAROS
[5]Light Conversion, ORPHEUS Collinear Optical Parametric Amplifier

### 2.3.2 Collimating optics

To be able to generate diffraction-limited foci in the center of the ultracold atomic cloud, we use a microscope objective[6] with a high numerical aperture of 0.5. The short working distance of 15.08 mm requires us to mount the objective in a re-entrant viewport in close distance to the atomic target (compare figure 2.3). To ensure that most of the pulse power of our femtosecond pulses is applied onto the atoms, the beam should have a waist equal or similar to the 4 mm-sized aperture of the objective at this point.
Our experiment is distributed over two adjacent laboratories: one room is occupied by the quantum gas machine, while the other contains the PHAROS laser system. This leads to a beam line with a length of 9.5 m [86] from the output of the HIRO or OPA to the aperture of the microscope objective. For laser safety reasons the beam is transported through a pipe leading from one lab to the other. To ensure pointing stability at the aperture of the microscope objective, the beamline is actively stabilized with a commercial piezo-driven 4D-beam stabilization system[7]. Due to the long beam line, collimation of the beams coming from the femtosecond laser system is crucial to obtain sufficient laser power behind the objective.
In theory the beam leaving the HIRO HG should already be collimated, in practice the internal collimation telescope yields rather insufficient results for our purpose and most of the laser power is lost on the way to the science chamber when no additional optics are added to the setup. To better collimate the 511.4 nm beam coming from the HIRO HG, an uncoated plano-convex lens with $f_1 = 100\,\text{mm}$ and an uncoated plano-concave lens with $f_2 = -40\,\text{mm}$ are set up in a distance of $d = 54\,\text{mm}$ as a Galilean telescope. This design avoids an intermediate focus which can be problematic at high peak intensities causing filamentation in the air. Despite the simple design, the beam width of the HIRO-beam at the microscope could be significantly reduced.
In former experiments we reached 90 mW [106] at a power setting of 1.8 W for the regenerative amplifier of the PHAROS pump laser. The power was measured through an aperture with a diameter of 4 mm, matching the aperture of the focusing microscope objective installed at the science chamber. With the new telescope the power at the same setting was more than tripled to 283 mW. Maximum power was achieved at 4.5 W output power of the PHAROS resulting in 1.2 W power in the second harmonic in front of the microscope objective, corresponding to a pulse energy of 12 µJ. There is still significant loss of power, since the beam has approximately twice the diameter as the 4 mm aperture at the microscope objective and the collimation telescope was set up with uncoated lenses. Since we use different wavelengths at the experiment, the beamline from the PHAROS to the science chamber was set up with silver mirrors instead of specialized high reflectivity mirrors for single wavelengths, introducing further losses into the setup.
For most of the experiments discussed in this thesis, the second harmonic of the idler of the OPA was used. For this purpose the collimated idler beam emitted by the OPA is focused into a beta Barium borate (BBO) crystal in the adjacent HG module to generate the second harmonic. This harmonic generation is optional and activated by

[6] Mitutoyo, G Plan Apo 50x
[7] TEM Aligna 4D

introducing an additional lens into the beam line leading to a divergent emerging beam from the HG module.
This divergent beam was collimated using a single achromatic doublet with $f_{\mathrm{OPA}} = 750\,\mathrm{mm}$ and an anti-reflective coating ranging from 400 nm to 700 nm. The realized maximum output power of the OPA and the measurement of the pulse energies at the experiment are discussed in the next subsection.

### 2.3.3 Pulse energy pickup

The energy of the pulses generated by the OPA is subject to significant shot-to-shot fluctuations. For this reason we implemented a simple means of measuring the energy of each applied pulse during an experimental cycle. A glass microscope slide is installed in the beam line, reflecting a small fraction of the pulse onto a fast biased photodiode[8] with a typical rise time of 1 ns. The amplitude of the voltage signal of the photodiode is then proportional to the pulse energy and can be recorded with an oscilloscope.
To calibrate the proportionality, the laser power is measured with a powermeter while at the same time the voltage pulses on the photodetector are recorded and averaged. Since there is a wavelength dependency on the sensitivity of the photodetector as well as in the reflectivity of the glass slide, this measurement is repeated for all relevant wavelengths. To avoid depletion of the (photodiode) powermeter head, a low repetition rate for the applied femtosecond laser pulses should be chosen, also this calibration should be repeated each time the alignment of the femtosecond beamline is adjusted.
In figure 2.9a the pulse energy $E_{\mathrm{P}} = P/f$ (where $f$ is the repetition rate of the pulse train and $P$ the measured laser power through a 4 mm aperture) is plotted for wavelengths ranging from 570 nm to 640 nm. The power is averaged over a time period of $\approx 60\,\mathrm{s}$ and the error bars mark the standard deviation.
Figure 2.9b depicts the averaged voltage signal on the photodetector for a few thousand pulses at a wavelength of 595 nm and figure 2.9c the completed calibration curve, where $E_{\mathrm{P}}$ is divided by the maximum of the averaged photodiode signals $U_{\mathrm{PD,max}}$ and the deviations are calculated via Gaussian error propagation.

## 2.4 Synchronization and time base

During the experimental work conducted for this thesis, the synchronization between femtosecond laser and quantum gas machine was modified and improved.
In figure 2.10a the three layers of the time base of our experimental setup are illustrated: The *SYNC2*-output of the PHAROS laser is used as a master clock. We configure this output to provide a copy of the logic signal that switches the Pockels cell of the regenerative amplifier (*RA OFF*) after amplification of a pulse, yielding a 100 kHz clock signal synchronous to the generation of pulses (This can of course also be achieved with the *SYNC1*-output). This clock signal is fed into a delay generator[9] to adjust the width of the pulses for compatibility with the ADwin[10]-system that controls all further analog

[8] Thorlabs Det10A/M
[9] Quantum Composers 9524
[10] Jäger Computergesteuerte Messtechnik GmbH, ADwin-Pro II

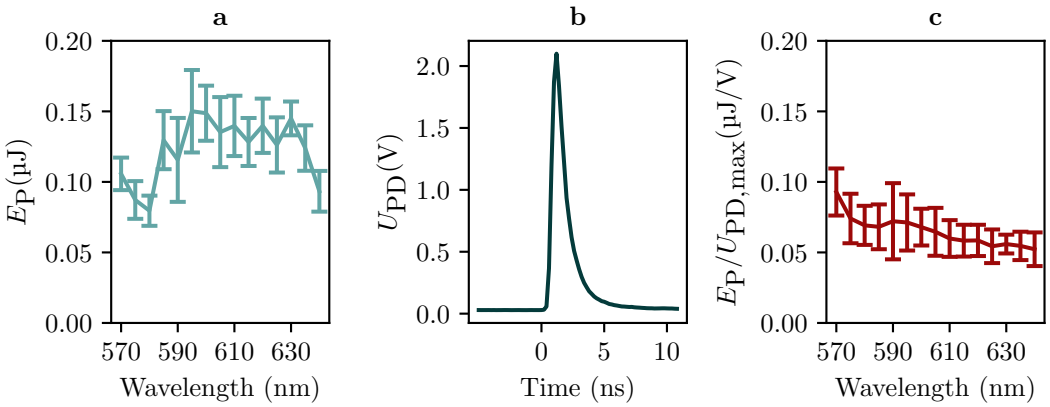


**Fig. 2.9: Calibration of the pulse pickup for measuring the pulse energy.**
**a.** Measured pulse energy $E_P$ of the OPA output and standard deviation near the science chamber in dependency on the wavelength. **b.** Example of an averaged photodiode signal for 595 nm over a few thousand pulses. **c.** The pulse energy is divided by the maximum of the recorded averaged pulses for each wavelength and $E_P/U_{PD,max}$ and its standard deviation is plotted against the wavelength to complete the calibration curve.

and digital signals.
With the ADwin we can generate arbitrary TTL-signals within the temporal frame of the clock, i.e. every 10 µs each channel can be switched from HIGH to LOW and vice versa. The jitter between these logic signals and the femtosecond laser pulses measured at the pulse pickup described in the previous chapter is $\sigma_{ADwin} = 7.6$ ns and limited by the clock rate of the ADwin processor.
Since the ultrafast dynamics in the ultracold plasma systems created in our experiments significantly subceed the time resolution of the ADwin, a delay generator[11] with a much finer resolution with a minimum step size of 5 ps is used for triggering the high-speed cameras and applying voltage pulses to the extraction meshes of the charged particle detection. When this delay generator is directly triggered by the clock signal and the ADwin is only used to gate the clock signal (i.e. arm the device at a specific time in the experimental cycle), the jitter between femtosecond laser pulses and voltage pulses is not limited by the jitter of the ADwin system.
In figure 2.10b two successive pulses of the femtosecond laser (dark red) and an arbitrary TTL pulse from the delay generator (dark turquoise) are illustrated. The jitter $\sigma_J$ of the TTL pulse in relation to the femtosecond laser pulse is $\sigma_J \approx 420$ ps and sets a lower bound to our time resolution. This jitter is the combined jitter of the clock of the PHAROS, the jitter of the pulse shaping delay generator and the jitter of the second delay generator that is used for higher time resolution. Furthermore, the interval between two pulses coming from the regenerative amplifier varies arbitrarily by one period $T_{osc} = 12$ ns of the PHAROS oscillator adding a much larger uncertainty. By recording the timing of the laser pulse as well as the output of the delay generator for each cycle of the experiment this uncertainty can be overcome, yielding sub-nanosecond time resolution.

[11] Stanford Research Systems DG645

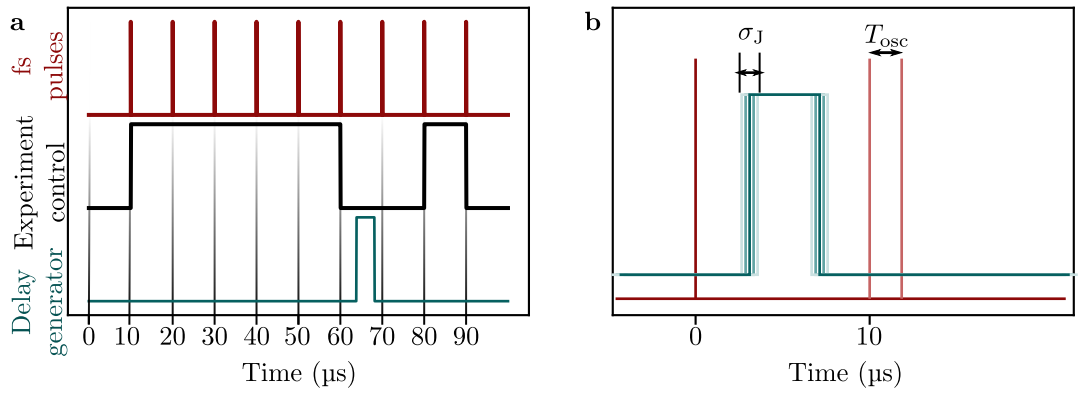


**Fig. 2.10: Time base of the experimental setup.**
**a.** The time base of the experimental setup can be divided into three layers: As a clock the RA OFF signal at the *SYNC2* output of the PHAROS laser system is used coinciding with the switching of the regenerative amplifier (dark red). The ADwin-Pro II system controlling the experiment is synchronized to this 100 kHz signal and provides TTL signals (black) with a minimum resolution of 10 µs and a jitter of $\sigma_{\mathrm{ADwin}} = 7.6\,\mathrm{ns}$ . For finer resolution, a delay generator (dark turquoise) can be used to create arbitrary pulse trains. **b.** The jitter $\sigma_J$ of an arbitrary pulse from the delay generator (dark turquoise) to a femtosecond laser pulse (dark red) is only $\sigma_J \approx 420\,\mathrm{ps}$. However, the interval between two femtosecond pulses has an uncertainty of one oscillator period of the PHAROS oscillator $T_{\mathrm{osc}} = 12\,\mathrm{ns}$. If necessary, this uncertainty can be overcome by measuring the timing of the femtosecond pulses and the TTL from the pulse generator for each cycle of the experiment.

## 2.5 Detection of charged particles

For the detection of the charged ionization products, there are two symmetrically fitted detector assemblies within the science chamber (see figure 2.3) - one for the electrons and one for the ions. A detailed illustration of the design is shown in figure 2.11: An extraction mesh usually set to a voltage of $V_{\mathrm{ext}} = \pm 300\,\mathrm{V}$ draws the electrons (or ions respectively) to a microchannel plate detector. For this purpose we use gold plated copper meshes with a high permeability of $t_{\mathrm{mesh}} = 70\,\%$ to $80\,\%$ [84, 90]. Even when we work with smaller voltages at the extraction meshes (details on the purpose of different extraction voltages can be found in the following sections), the applied potential at the front of the MCP accelerates the particles to a kinetic energy of 268 eV for the electrons and 1 keV for the ions. The natural energy scales in the systems we investigate are on the order of meV up to a few eV. Without the acceleration after the meshes, these energies have vanishing quantum efficiencies for detection at the MCP detectors. Counteracting this, the post-acceleration guarantees a constant quantum efficiency on the order of $QE_{\mathrm{e}} \approx 80\,\%$ [69] for the electrons, while it is significantly lower for the ions with $QE_{\mathrm{i}} \approx 20\,\%$ [107].
Besides the transparency of the extraction mesh and the quantum efficiency of the MCP detectors, we also have to take the open area ratio of $\eta_A$ of the MCPs into account.

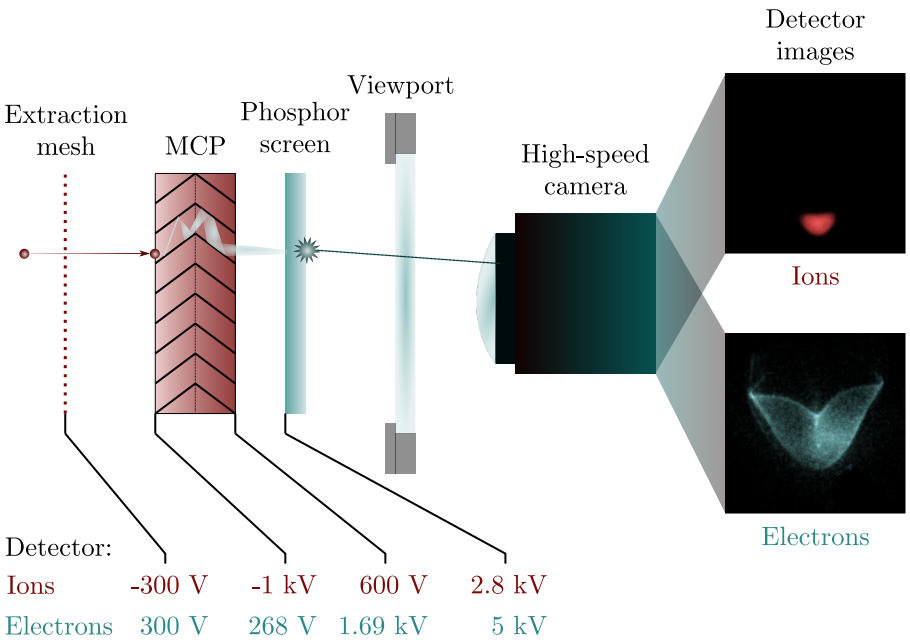


**Fig. 2.11: Charged particle detection.**
The charged ionization products are drawn by an extraction mesh set to an attractive potential towards a microchannel plate detector and post-accelerated towards the front of the MCPs. At the MCP the particles trigger electrons in the material, which then get accelerated within the MCP channel triggering an avalanche of secondary electrons. These multiplied electrons in turn get accelerated towards a phosphor screen behind the MCP where they trigger photons which can be recorded by a high-speed camera set up outside of the vacuum chamber. Two exemplary false color images for both the ion and the electron detector signal are shown on the right. The voltages listed show the applied voltages to the electrodes of the two detectors.

The detection efficiency of a particle that hits the detector is then given by:

$$\eta_{\mathrm{e,i}} = t_{\mathrm{mesh}} \cdot \cdot QE_{\mathrm{e,i}} \cdot \eta_A \tag{2.1}$$

and amounts to $\eta_{\mathrm{e}} \approx 40\,\%$ for the electrons and $\eta_{\mathrm{i}} \approx 10\,\%$ for the ions.
The MCPs used in the setup have a nominal gain of $\geq 4 \times 10^6$ [12] for a voltage difference of 2 kV, thus a detected particle can create avalanches of approximately $10^6$ electrons. These electrons emerging form the backside of the MCP get further accelerated by applied potentials, eventually hitting a P46 phosphor screen with decay times on the order of 300 ns.
Here, a single inciding electron yields a few dozen photons which then can be detected outside the vacuum chamber by a simple camera setup. Due to the fast timescales expected in our experiments, we use high-speed cameras with a maximum frame rate of 120 kHz with commercially available objectives[13]. An example false color image for each detector is also shown in the figure. The shape of the detector signals will be discussed in the corresponding subsections 2.5.2 and 2.5.4.

[12] GIDS MCP-45-2-40-P46-N
[13] Camera: Vision Research, Phantom Miro 310, Objective: Nikon, AF-S NIKKOR 50 mm 1:1.4 G

The voltages set to the extraction meshes, MCPs and phosphor screens are listed in figure 2.11. For the electron side, a single power supply provides the voltages for the MCP and phosphor screen via a voltage divider designed specifically for this purpose [69]. The ion detector is supplied by separate supplies for each potential. Here, the potential difference between the backside of the MCP and the phosphor screen is significantly smaller than the recommended value due to a defect in the assembly that causes the detector to spark at higher voltages. This suboptimal potential difference decreases the efficiency of the phosphor screen leading to less photons per detected particle at the MCP (i.e. the brightness of the detector images is reduced).
Aside from the detection efficiency discussed in this section, the incidence probability should also be taken into account: Electrons and ions with higher initial kinetic energies will escape the field-of-view of the detector with a higher probability than electrons with lower initial kinetic energies. The energy dependence of the incidence probability of both electrons and ions will be discussed in the corresponding subsections 2.5.2 and 2.5.4.

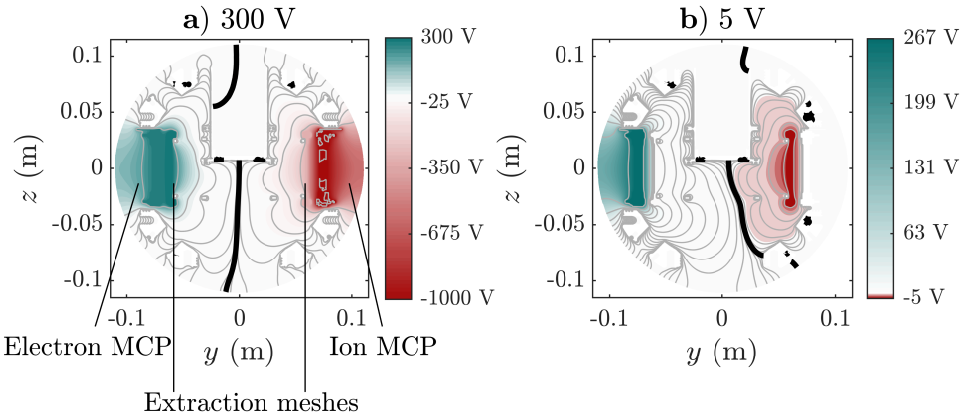


**Fig. 2.12: Calculated electric potentials in the science chamber.**
**a.** The extraction meshes are set to $V_{\text{ext}} = \pm 300\,\text{V}$ and the MCPs to the voltages listed in figure 2.11. The lines show equipotential lines to illustrate the geometry of the field. Potentials from 0 V to 300 V are shaded in turquoise , while potentials from 0 V to $-1000\,\text{V}$ are shaded in red. The thick black line marks an equipotential of 0 V, revealing a slight asymmetry along the central axis of the setup. **b.** In the low-voltage mode of operation the extraction meshes are set to $V_{\text{ext}} = \pm 5\,\text{V}$ and the ion MCP detector is switched off. Potentials between 0 V to $-5\,\text{V}$ are shaded in red, while potentials between 0 V to 268 V are shaded in turquoise. Again the equipotential lines and the thick black line marking the ground potential reveal the asymmetry in the electric field configuration, which is exacerbated by the low extraction potentials compared to the high potential of the electron MCP.

### 2.5.1 Electric field configuration

Although the detector setup has a vertical symmetry plane right in the center of the science chamber, full cylindrical symmetry along the detector axis is broken by the rectangular shape of the mesh holders, the grounded spherical vacuum chamber and most notably the grounded shielding mesh below the re-entrant viewport close to the atoms. This leads to an asymmetric configuration of the electric field along the detector, impeding the usage of the setup as a common velocity map imaging (VMI) spectrometer. In our experiments we generally employ two modes of operation (with possible minor variations):
If the interest is focused on the energy spectra of the electrons and simultaneous detection of the ions, the extraction meshes are set to $V_{\text{ext}} = \pm 300\,\text{V}$ and the MCPs to 268 V and $-1000\,\text{V}$ as stated in figure 2.11. This is close to the upper voltage limit of the vacuum feedthroughs for the extraction meshes.
If precise time-resolved detection of electrons is necessary or the focus lies on electrons with low kinetic energy, the extraction meshes are set to potentials of $V_{\text{ext}} = \pm 5\,\text{V}$. The electron MCP is then still set to 268 V to achieve constant quantum efficiency. However, the ion detector is switched off in this setup, since it significantly distorts the fields in the center of the chamber when set to a potential of $-1000\,\text{V}$. At lower extraction mesh voltages also the asymmetric field from the electron MCP detector becomes dominant and only few electrons hit the detector.
Knowledge of the electric fields within the chamber is crucial to understand the features appearing in the detector images. To this end we employ finite element method (FEM) simulations of the static electric fields within a 3D computer-aided design (CAD) geometry of the fully equipped science chamber. We use the electrostatics module of the COMSOL Multiphysics® [108] software to calculate the fields and the charged particle tracing (CPT) module to trace the trajectories of the charged particles to generate simulated detector images.
For the meshing of the geometry the predefined option *physics-controlled* with a *finer* setting is used, resulting in mesh elements between 0.88 mm and 12 mm, resolving the geometry with details down to the heads of the mounting screws of the mesh holders.
In figure 2.12a the equipotential lines for the aforementioned voltage configuration for simultaneous detection of electrons and ions with extraction potentials of 300 V are shown. Positive potentials from 0 V to 300 V are shaded in turquoise, while negative potentials from 0 V to $-1000\,\text{V}$ are shaded in red. The thick black line marks an equipotential line of 0 V revealing a slight asymmetry in the electric field in the interaction volume of the ultracold target and the femtosecond laser in the center of the chamber. This is caused by the asymmetry in the potentials of the front electrodes of the MCPs. The electric field in the interaction volume is $E_{300\,\text{V}} \approx 162\,\text{V/m}$.
In the low-voltage detection mode for the electrons (2.12b) with the meshes set to 5 V, the asymmetry in the equipotential lines is far more pronounced, since the potential set to the meshes is much smaller than the potential at the front electrode of the electron MCP. The front electrode of the ion MCP is set to ground increasing the asymmetry. The electric field in the interaction region is $E_{5\,\text{V}} \approx 4.6\,\text{V/m}$. The reproducibility of our measurements and good agreement with CPT simulations in this setting indicate that stray fields are still smaller than this value.

The slight asymmmetry in the field configuration could be eliminated by setting the front of the MCP of the ion detector to −268 V. In the past, a voltage divider was used at the ion detector, limiting the flexibility in setting arbitrary voltages to the elements of the detector assembly. Furthermore, the aforementioned defect in the ion detector assembly that quickly generates sparks, suppressed further experimentation. More recent results were recorded with the same asymmetric setup to allow for comparability. Although the geometry of the assembly is well reproduced with a fine mesh and the voltages at the electrodes are well known, one minor uncertainty remains: the mesh electrodes are modeled as continuous circular planes set to $\pm V_{\text{ext}}$. In reality these meshes have a grid size of 8 lines per millimeter, possibly allowing for the field of the MCP to penetrate the mesh. This field penetration is neglected in the simulations.

### 2.5.2 Understanding the electron detector signal

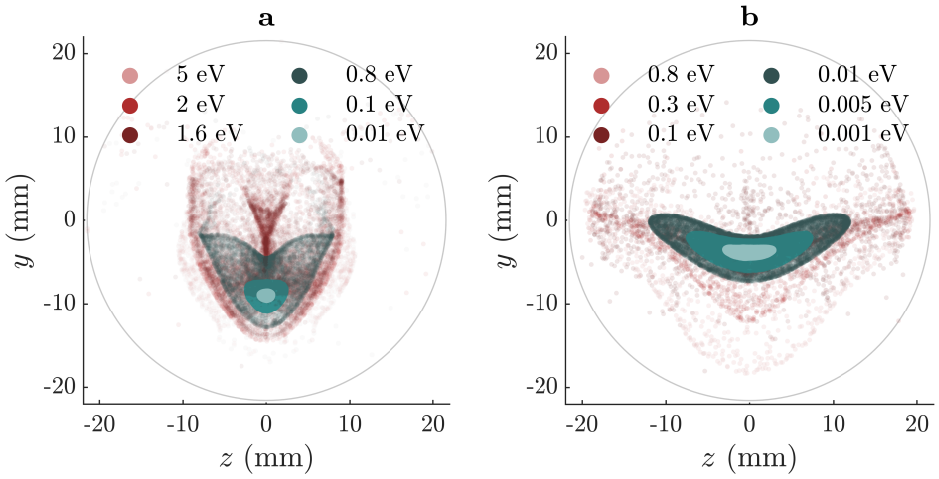


**Fig. 2.13: Simulated electron detector images for different initial energies.**
**a.** Simulated detector images at $V_{\text{ext}} = \pm 300\,\text{V}$ for different initial kinetic energies. Due to the high kinetic energy in comparison to the Coulomb repulsion, the Coulomb interaction between the electrons can usually be neglected. While an ensemble of electrons with low kinetic energies barely expands on its way to the detector, increasing kinetic energies form heart-shaped structures with increasing size on the detector. While it is difficult to distinguish between energies that differ by only a few meV, this mode of operation allows to detect energies that span two orders of magnitude. **b.** Simulated detector images at $V_{\text{ext}} = \pm 5\,\text{V}$ for different initial kinetic energies. While energies from 1 meV to 10 meV form well distinguishable structures with sharp edges, higher energies get more and more washed out over the detector, making this mode of detection more suited for very low kinetic energies.

As the cylindrical symmetry of the detector assembly and the electric fields within is broken, analyzing the resulting detector images is not a trivial task. Conventional means like e.g. the Abel inversion used in common velocity map imaging devices are not applicable in this setup.

However, the use of charged particle tracing simulations offers a way to generate simulated detector images with precisely defined intial conditions. By comparing these images with experimental images similarly precise conclusions can be drawn. An alternative approach to estimate the electron energies with purely experimental techniques is illustrated in appendix A.1.
For the electron side of the detector, the electric potential landscape is calculated as described in the previous subsection. As a spatial distribution for the electrons a cylinder with a radius $r = 1.35\,\mu\text{m}$ and a height $h = 5\,\mu\text{m}$ iss chosen in the center of the chamber. This volume corresponds to the expected ionization volume for a 511 nm pulse with an intensity of $I_0 = 1.9 \times 10^{13}\,\text{W/cm}^2$ applied to a BEC [69, 106]. To estimate the energy-dependence of the electron signal, Coulomb interaction between the electrons was neglected and they are given a fixed initial kinetic energy. In the experiment this holds true as long as the Coulomb energy of the particles is much smaller than the kinetic energy. As a crude estimation of the energy scales, let us look at the Coulomb energy between two electrons:

$$E_\text{C} = \frac{e^2}{4\pi\epsilon_0 r} \tag{2.2}$$

with the elementary charge $e$, the vacuum permittivity $\epsilon_0$ and the distance between the two particles $r = 2 \cdot a$ where a is the Wigner-Seitz radius. This energy at a typical density of a BEC of $\rho_\text{BEC} = 2 \times 10^{20}\,\text{m}^{-3}$ amounts to $E_\text{C,BEC} = 6.8\,\text{meV}$ which is much smaller than the excess energy of 678 meV at 511 nm. Even when ionizing at the threshold with 593.7 nm and vanishing excess energy, the energy width of the laser pulse for a two-photon process $2 \times \sigma_\text{E}$ and thus the energy of the electrons is on the same order of magnitude.
Figure 2.13a shows the results of the CPT simulations for the mode of operation with $V_\text{ext} = \pm 300\,\text{V}$. For each depicted kinetic energy from 0.01 eV to 5 eV, 10000 electrons are initially placed in the cylindrical volume with an isotropic velocity distribution. From these detector images it is possible to distinguish low initial kinetic energies from higher kinetic energies by comparing the extent of the signal on the detector. While a cloud of initially slow electrons barely expands on its way to the detector and incides within a small elliptical area near the center of the screen, an ensemble of faster electrons significantly expands in the inhomogeneous field and forms a heart-shaped structure on the screen. This mode of operation does not allow to determine the initial energy of the electrons with meV resolution but it allows to clearly distinguish between classes of electrons that energetically span two orders of magnitude.
In figure 2.13b, the same principle is applied to the mode of operation with $V_\text{ext} = \pm 5\,\text{V}$. The signal on the detector becomes significantly larger and the energies above 0.1 eV are more difficult to distinguish. Low energies from 1 meV to 10 meV are well represented here and can be differentiated. To get a suitable image of these small energies in the experiment (and the simulation), a constant magnetic field of 370 mG has to be applied perpendicular to both the detector axis as well as the propagation axis of the femtosecond pulse. Without magnetic field the electrons will not arrive at the detector but hit the mesh holder assembly instead.
Since very low extraction fields are used here, the time of flight of the electrons is significantly prolonged. The small voltages allow for fast pulsing of the meshes in order

to execute precise time-resolved measurements of the electrons arriving at the detector (see subsection 2.5.6).

Figure 2.14a shows the energy dependence of the incidence probability of the elec-

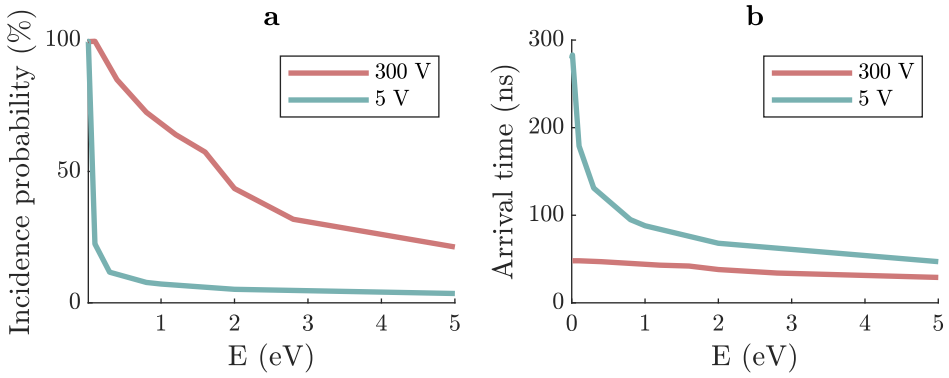


**Fig. 2.14: Incidence probability and arrival times of the electrons on the detector.** **a.** The plot shows the energy dependence of the incidence probability of the simulated electron distributions with an isotropic velocity distribution for $V_{\text{ext}} = \pm 300\,\text{V}$ (red) and for $V_{\text{ext}} = \pm 5\,\text{V}$ (turquoise). While the incidence probability for the high voltage mode decreases from 100 % for 10 meV to 76 % for 678 meV to a minimum of 21 % for 5 eV, with the low voltage mode the incidence probabilty quickly drops below 9 % for energies higher than 678 meV. **b.** The point in time, when half the total of the detected electrons have arrived at the detector is plotted for $V_{\text{ext}} = \pm 300\,\text{V}$ (red) and $V_{\text{ext}} = \pm 5\,\text{V}$ (turquoise). While the arrival time for the high voltage mode never exceeds 50 ns, the arrival time of the low voltage mode is much more sensitive to the initial kinetic energy of the electrons ranging from 283 ns at 1 meV to 47 ns at 5 eV.

trons at the detector for both voltage configurations for an initially spatially uniform velocity distribution. The incidence probability should not be confused with the detection probability $\eta_{\text{e,i}}$ discussed before: While the incidence probability is the probability that a particle starting in the ionization volume reaches the detector, the detection probability is the probability that a particle hitting the detector will be detected. The mesh transmission could of course be accounted to either of the two probabilities, for simplicity we included it in the detection probability (since it is not included in the CPT simulations).

For the 300 V configuration the probability to reach the detector approaches 100 % for an initial kinetic energy of 10 meV but quickly decreases to 76 % for 678 meV and down to 21 % for the highest simulated energy of 5 eV.

For the 5 V configuration the effect is even more pronounced: while the lowest calculated energy of 1 meV can be detected with an incidence probability of 100 %, the incidence probability of 678 meV only amounts to 9 % and for 5 eV it is only 4 %. Due to the small extraction field, only electrons that initially fly towards the detector can be detected here.

In figure 2.14b the arrival time of the electrons at the detector is plotted, again, for both configurations and varying kinetic energy. Here, the arrival time is given by the point in time when half of the detected electrons have hit the detector. There is a qualitative difference between the two curves: For the 300 V configuration the curve is almost flat,

with an arrival time of 48 ns for 10 meV decreasing to 29 ns for 5 eV. For the low voltage configuration the difference in arrival times ranges from 283 ns for 1 meV decreasing to 47 ns for 5 eV. This confirms that for the high voltage configuration the electron trajectories are dominated by the acceleration through the extraction field, while for the low voltage configuration the arrival time and the trajectories are more sensitive to the initial velocity and kinetic energy of the particles.

### 2.5.3 Effect of the polarization of the femtosecond pulse

In the previous subsection the energy dependence of the electron detector signal was investigated using isotropic velocity distributions. Yet in reality, the angular distribution of the emerging photoelectrons is not expected to be isotropic. For photoionization using a single photon of linearly polarized light the angular distribution of photoelectrons can be expressed as:

$$\frac{\mathrm{d}\sigma}{\mathrm{d}\Omega} = \frac{\sigma_{\mathrm{tot}}}{4\pi}(1 + \beta_2 P_2 \cos\theta) \tag{2.3}$$

Here $\theta$ is the angle between the polarization axis and the velocity vector of the emerging electron, $\sigma_{\mathrm{tot}}$ is the total ionization cross section and $P_2$ the second order Legendre polynomial. $\beta_2$ is the anisotropy parameter, restricted to the interval between -1 and 2. For $\beta_2 = 0$ the distribution becomes isotropic, while the anisotropy becomes maximal at $\beta_2 = -1$ and $\beta_2 = 2$. The determination of the $\beta$-parameter is not trivial and depends among other things on the initial state of the atom and the polarization of the laser light.
For multiphoton processes a similar expression can be found: [109]

$$\frac{\mathrm{d}\sigma^{(N)}}{\mathrm{d}\Omega} = \frac{\sigma_{\mathrm{tot}}}{4\pi}\sum_{k=0}^{N}\beta_{2k}P_{2k}(\cos\theta) \tag{2.4}$$

Where $N$ is the number of photons involved in the process and $P_{2k}$ is the Legendre-polynomial of the $2k$-th order. The anisotropy parameters $\beta_{2k}$ can not be calculated ab-initio for the parameters in the experiment here. Internal communications with Andrey Kazansky and Andrei Borissov granted access to calculations of the electron spectra for strong-field ionization of $^{87}$Rb acquired by solving the time-dependend Schrödinger equation for a suitable model potential. Earlier results of similar calculations with a focus on the ionization cross-section were published in [33]. The resulting angular distribution for 511 nm and a peak intensity of $I_0 = 10\times10^{11}$ W/cm$^2$ is plotted in figure 2.15a (turquoise). The dotted red-line is a fit with the angular distribution in equation (2.4) and suggests the anisotropy parameters $\beta_2 = 1.052(1)$ and $\beta_4 = 1.147(1)$.
To see the effects of this angular distribution on the detector images, corresponding CPT simulations are performed. Figure 2.15b shows the results of these simulations in a polar plot (red dotted line). The angular axis in this plot marks the angle between the polarization angle and the detector axis. For each angle an electron distribution of 10000 particles is propagated through the detector assembly in the configuration with $V_{\mathrm{ext}} = 5$ V and the inciding particles on the detector are counted and normalized to their respective maximum. The pronounced lobes of the angular distribution in at 0°

and 180° are still quite visible, the smaller maxima in the angular distribution at 90° and 270° are slightly suppressed due to the field configuration in the chamber.
The same principle is applied to the experiment: by including a $\lambda/2$-waveplate in a rotation mount in front of the focusing objective of the femtosecond laser, the polarization of a 511 nm pulse from the HIRO is rotated from 0° to 360° in steps of 10° and applied to a thermal cloud with a density of $\rho = 8 \times 10^{17}\,\mathrm{m}^{-3}$. For each data point 44 experimental cycles are recorded. In each experimental cycle 10 images of the electron detector are taken, each capturing the emerging electrons from a pulse train of 100 pulses to obtain sufficient statistics. In the figure, the mean brightness of the detector image is plotted and normalized to the maximum brightness, the error bars mark the standard deviation. Comparing the simulated *counts* to the experimentally recorded *brightness* is valid as long as the detector is not saturated. Depending on the MCP and camera gains the incidents on the MCP are proportional to the brightness in the recorded image. The angular distribution agrees well with the simulated case, with two distinct maxima at 0° and 180°, however the secondary maxima are more pronounced here and have an angular offset of approximately 30° and do not appear to be exactly perpendicular to the primary maxima. It is possible that the focused beam from the femtosecond laser is not perfectly perpendicular to the detector axis. This would tilt the rotation axis of the angular distribution and distort the projection on the detector and could explain the small angular offset.
Figure 2.16 shows a selection of averaged and normalized detector images for multiple angles from 0° to 180° from this measurement. While the shape of the overall signal remains constant for different angles, the density distribution of the counts within the shape varies. At 0°, 120° and 180°, when one of either the primary or the (offset) secondary maxima of the angular distribution are aligned with the detector axis, the shape is homogeneously filled. For angles in between the density of counts has a rather distinct maximum in either the right or left part of the shape.
This comparison shows, that for the low voltage mode of operation, the angle of polarization will significantly influence the incidence probability of the electrons. For a uniform velocity distribution we determined a incidence probability of 9 % for the 511 nm pulse. The simulations with the realistic angular distribution show that this incidence probability can be tuned to 14 % when the primary maxima are aligned with the detector axis, improving the detection efficiency. If the axis is misaligned the detection efficiency is decreased to a minimum of 4 %.

### 2.5.4 Understanding the ion detector signal

Because of the symmetric design of the detector assemblies the ion detector functions in much the same way as the electron detector. This means, that again the shape of the signal depends on the energy of the ions. While the electron detector directly images the initial kinetic energy that is given to the electrons during the ionization process, the energies measured by the ion detector are a result of the Coulomb interaction between the ions. This can be estimated by the same considerations we made for the electron detector. The Coulomb energy between two neighboring ions is the same as for the electrons (see equation (2.2)) at BEC density: $E_{\mathrm{C,BEC}} = 6.8\,\mathrm{meV}$, yet the initial kinetic energy from the ionization process is more than three orders of magnitude lower and

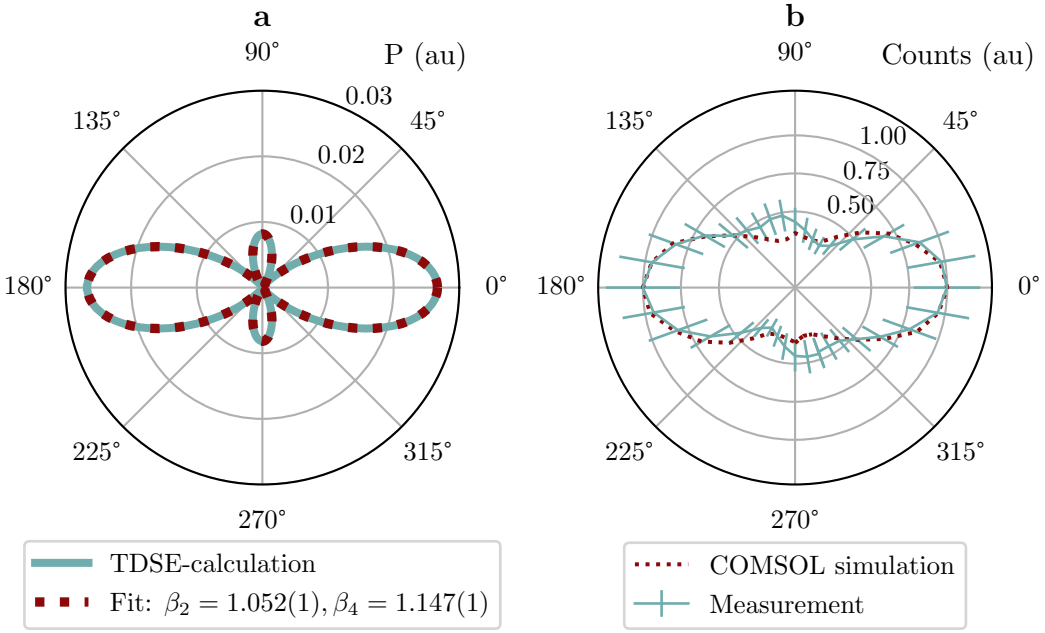


**Fig. 2.15: Angular distribution of the photoelectrons at 511 nm.**
**a.** TDSE calculations of the angular distribution of photoelectrons at wavelength of 511 nm with a peak intensity of $I_0 = 10^{11}\,\mathrm{W/cm^2}$ (turquoise) and fit with equation (2.4), yielding the anisotropy parameters $\beta_2 = 1.052(1)$ and $\beta_4 = 1.147(1)$. **b.** The detector counts from COMSOL Multiphysics® simulations (red dotted line) with the same angular distribution for a varying angle of polarization are compared to the detector brightness of an experimental realization (turquoise). The polarization in the experiment is rotated using a $\lambda/2$-waveplate and for each angle 44 realizations with $10 \times 100$ pulses are averaged. The error bars mark the standard deviation of the detector brightness. The measured angular distribution shows a small deformation where the secondary maxima that should be perpendicular to the primary maxima are now located at approximately 120° and 280°.

amounts to only 4.3 µeV for 511 nm. This suggests that the Coulomb repulsion between the ions clearly dominates the energy spectrum of the ions.
To gain a better understanding of the experimental images, simulated detector images are generated with a range of initial conditions. In the same cylindrical volume mentioned above with $r = 1.35\,\mu\mathrm{m}$ and a height $h = 5\,\mu\mathrm{m}$ within our virtual detector model, a distribution of ions is generated. The initial kinetic energy is set to zero and instead the number of particles in the volume is varied from N=100 to 5000 yielding ion densities of $\rho = 3.5 \times 10^{18}\,\mathrm{m^{-3}}$ to $1.7 \times 10^{20}\,\mathrm{m^{-3}}$ and the particles are propagated through the electric potential landscape taking Coulomb interaction between the particles into account. This is comparable to the situations in the experiment when using a thermal cloud with densities of $\rho_{\mathrm{th}} \geq 10^{17}\,\mathrm{m^{-3}}$ or a BEC with densities up to $\rho_{\mathrm{BEC}} = 2 \times 10^{20}\,\mathrm{m^{-3}}$ as target, neglecting the shielding by the electrons.
Figure 2.17 shows the simulated detector images for these densities. Since the ion detection is only possible in the mode of operation with $V_{\mathrm{ext}} = 300\,\mathrm{V}$, the low voltage mode is omitted. While the lower densities produce a small half-moon-shaped signal,

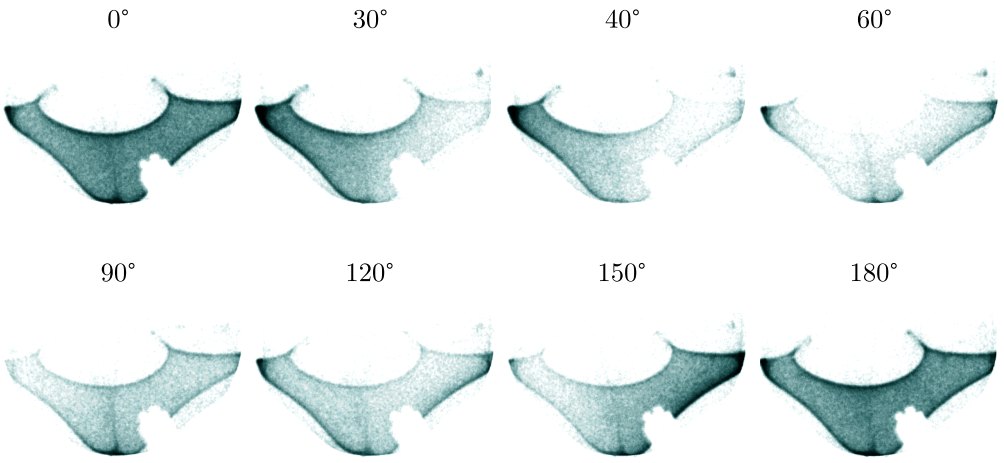


**Fig. 2.16: Exemplary detector images of the polarization scan.**
At 0° the maximum of the angular distribution shown in figure 2.15 is aligned with the detector axis and the shape of the signal is homogeneously filled with counts. With increasing angle between polarization axis and detector axis the center of mass of the counts moves to the left and leaves the detector until at $\approx 120°$ the secondary maximum is aligned with the detector axis. For larger angles the opposite primary maximum becomes visible on the right side of the detector until it is in alignment with the detector at 180°.

the higher density of a BEC produces a much larger signal with pronounced wings protruding to the top-left and top-right, occupying a much larger area of the detector.

Aside from looking qualitatively at the shape of the detector signals, the simulations offer insight into the incidence probability and the timescales, analogue to the electron signals discussed above. Figure 2.18a shows the incidence probabilty of the simulated ion distributions. For particle ensembles with densities up to $\rho = 10^{19}\,\mathrm{m}^{-3}$, almost all particles arrive at the detector - a minor fraction of 3 % will hit the grounded shielding mesh of the re-entrant viewport right above the ionization zone. For the highest simulated density of $\rho = 1.7 \times 10^{20}\,\mathrm{m}^{-3}$, approaching the typical density of our BEC, the incidence probability is reduced to 46 %.
In figure 2.18b the arrival times of the ions are plotted for the simulated particle distributions. Like in the electron case discussed above, here the arrival time is given by the point in time when half of the total inciding particles has arrived at the detector. Compared to the electron detector, the timescales are more than two orders of magnitude larger ranging from 18.4 µs to 14.8 µs due to the larger mass of the ions. This large difference of the timescales requires different schemes for time-resolved detection for both detectors, which will be discussed in the following subsections 2.5.5 and 2.5.6.

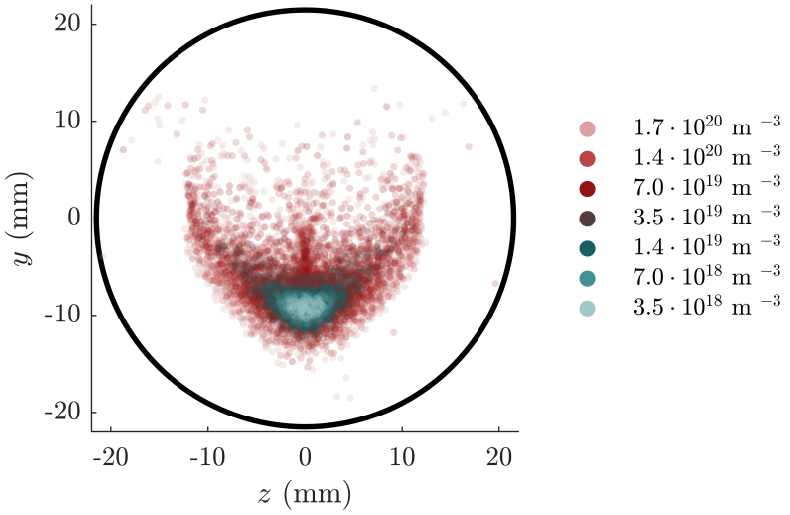


**Fig. 2.17: Simulated ion detector images for $V_{\mathrm{ext}} = \pm 300\,\mathrm{V}$.**
The shape and size of the ion signal is determined by the energy distribution of the particles. Unlike the electrons, the energy of the ions is not dominated by the excess energy of the ionization process, but by the Coulomb interaction. The number of ions in a fixed cylindrical volume with $r = 1.35\,\mu\mathrm{m}$ and a height $h = 5\,\mu\mathrm{m}$ is varied while the initial kinetic energy is set to zero. The resulting ensembles with particle densities of $\rho = 3.5 \times 10^{18}\,\mathrm{m}^{-3}$ to $1.7 \times 10^{20}\,\mathrm{m}^{-3}$ are propagated through the detector under consideration of Coulomb interactions. Increasing densities yield structures that occupy larger areas of the detector with more pronounced wings.

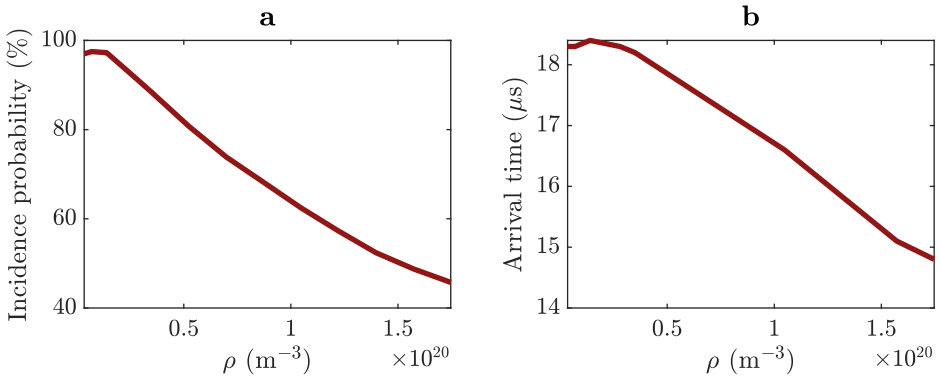


**Fig. 2.18: Incidence probability and arrival times of the ions on the detector.**
**a.** Incidence probability of the simulated ion distributions for different densities. For the densities of an ultracold thermal cloud at the lower range of the simulated spectrum the incidence probability is close to 100 % while it is reduced to 46 % for a density of $\rho = 1.7 \times 10^{20}\,\mathrm{m}^{-3}$. **b.** The plotted arrival time is given by the time when half of the total detected ions has arrived at the detector. For the ions it ranges from 18.4 µs to 14.8 µs which is more than two orders of magnitude higher than for the electrons due to the larger mass of the ions.

### 2.5.5 Time-resolved ion detection

The ion images alone contain only information about the Coulomb energy as discussed above. However the combination of high-speed cameras and the microsecond timescales of the ion trajectories to the detector allow for simple time-resolved measurements. Figure 2.19 illustrates the procedure used. The ions emerging from the ultracold target get drawn by the extraction meshes to the detector assembly and arrive here over a span of a few microseconds. The high-speed camera has a minimum exposure time of $T_{\mathrm{exp}} = 1\,\mu\mathrm{s}$ which sets the minimum time resolution for the detection. The temporal distribution of the ions can then be scanned by simply shifting the frame delay $T_{\mathrm{frame}}$ of the camera in respect to the femtosecond pulse resulting in images similar to the false color example images given in the figure. From these images the arrival time spectrum can be reconstructed.
The frame delay is currently realized with a Stanford Research Systems DG645 delay generator synchronized to the ADwin-Pro II used as central experimental control. Thus, the timing uncertainty of the aforementioned jitter is almost three orders of magnitude smaller than the exposure time and can be neglected.

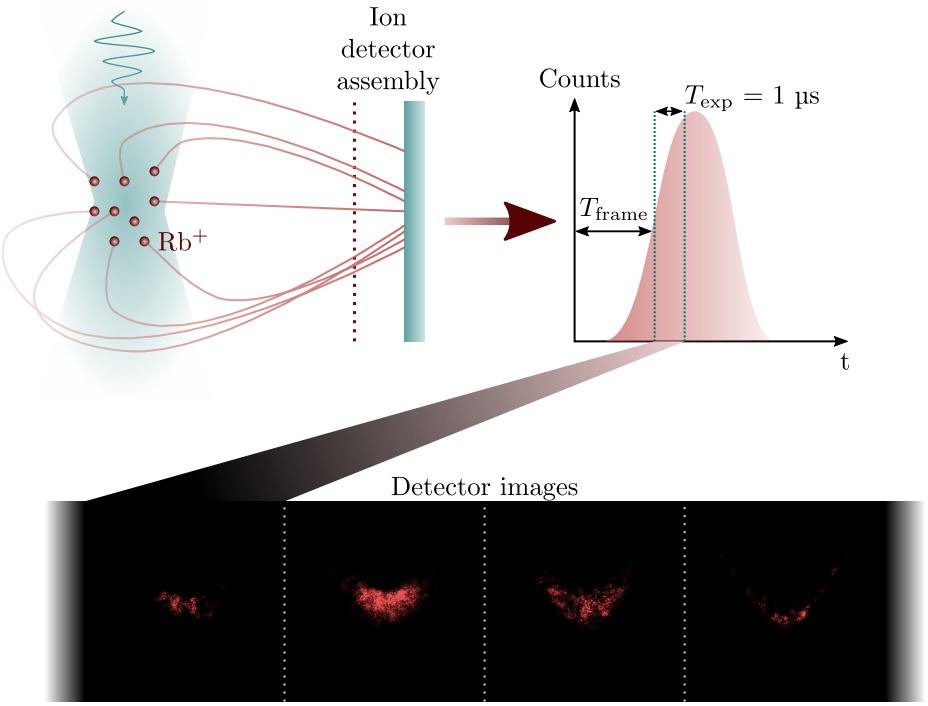


**Fig. 2.19: Time-resolved ion detection.**
After the photoionization process, the ions get drawn towards the ion detector assembly by the extraction meshes. They hit the detector over a time span of a few microseconds, which can be resolved by the minimum exposure time of $T_{\mathrm{exp}} = 1\,\mu\mathrm{s}$ of the high-speed cameras. By scanning the delay of the frame trigger $T_{\mathrm{frame}}$ in respect to the ionizing femtosecond laser pulse the ion arrival time distribution can be scanned over the course of multiple experimental cycles. The exemplary false color detector images show an averaged ion signal recorded this way.

### 2.5.6 Time-resolved electron detection

Time-resolved detection of the electrons is much more challenging than for the ions. The electrons only need a few tens to hundreds of nanoseconds to reach the detector, hence they can not be resolved with the $T_{\mathrm{exp}} = 1\,\mu\mathrm{s}$ time resolution of the scheme used for the ion detector. In previous works [106] a gated detection scheme illustrated in figure 2.20 was used. Here, instead of applying a constant positive voltage $V_{\mathrm{ext}}$ to the extraction mesh, the voltage is switched to a repulsive negative voltage with the same magnitude $-V_{\mathrm{ext}}$ after a delay $T_{\mathrm{pulse}}$. Electrons arriving at the extraction mesh after $T_{\mathrm{pulse}}$ will then be prevented from hitting the MCP detector. The measured counts on the detector then yield the integrated counts up to $t = T_{\mathrm{pulse}}$.
The technical implementation of this detection scheme was discussed in detail in the PhD thesis of Tobias Kroker [69]. For the mode of operation with $V_{\mathrm{ext}} = 300\,\mathrm{V}$ it proved to be challenging, since the rise time of the corresponding voltage pulse from 300 V to $-300\,\mathrm{V}$ amounted to 30 ns is on the order of the timescale of the electron dynamics. Best results were achieved with $V_{\mathrm{ext}} = 5\,\mathrm{V}$ due to the longer timescales of the electron trajectories and the shorter rise times.
In recent measurements we were able to improve upon this scheme by exchanging the DEI HV-1000-N high voltage pulser with a self-built pulser that supplies voltage pulses up to $\pm 50\,\mathrm{V}$ with better rise times. Furthermore, the improved synchronization described in section 2.4 combined with simultaneous measurement of the exact timing of the voltage pulse in respect to each individual femtosecond pulse now allows for sub-nanosecond resolution on the order of the jitter $\sigma_{\mathrm{J}} \approx 420\,\mathrm{ps}$ of the timebase.

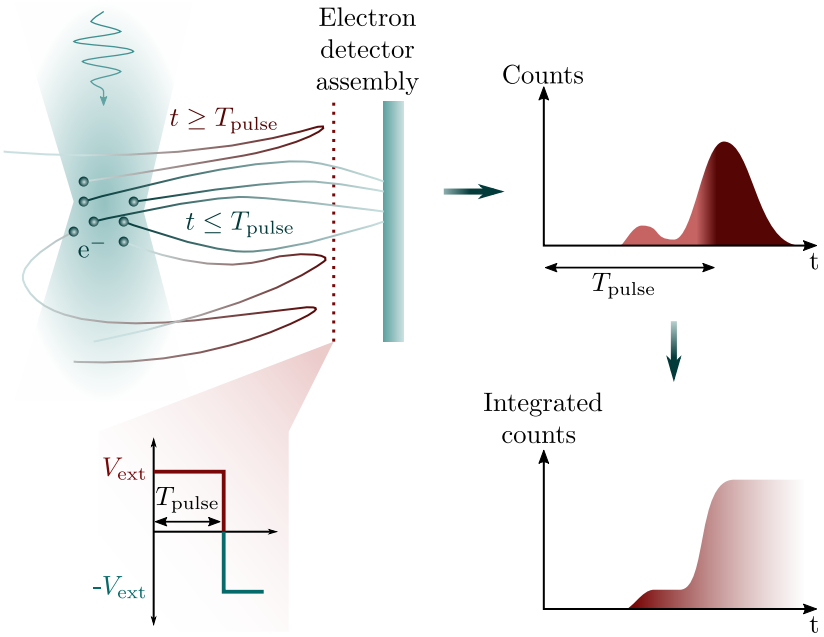


**Fig. 2.20: Time-resolved detection of electrons.**
Photoelectrons get drawn to the electron detector assembly by the electric field between the extraction meshes. Instead of using a constant potential at the extraction mesh, the voltage is pulsed from a positive and attractive voltage $V_{\text{ext}}$ to negative and thus repulsive voltage $-V_{\text{ext}}$ after a time delay of $T_{\text{pulse}}$ in respect to the femtosecond laser pulse. Electrons arriving at times $t > T_{\text{pulse}}$ will be repulsed from the mesh and not hit the detector. Each realization then yields the integrated counts up to $T_{\text{pulse}}$.

# 3 Ultrafast electron cooling in an ultracold microplasma

In the past, there have been extensive studies on ultracold neutral plasma ionized from atoms in a magneto-optical trap [34–36]. In this chapter we report on the emerging plasma dynamics at considerably higher densities and lower temperatures when a fraction of a $^{87}$Rb BEC is ionized with a femtosecond laser pulse.
A unique property of the plasma systems realized in this manner lies in the high initial density of electrons and ions and high initial kinetic energies of the electrons due to the large excess energy of the two-photon ionization process when a femtosecond pulse with a wavelength of 511 nm is used. We observe a micrometer sized highly charged plasma that exhibits a striking ultrafast electron cooling mechanism.
Section 3.1 gives a short introduction on ultracold plasma and the common measures and terminologies. In section 3.2 the experimental conditions are layed out, local ionization of the BEC is motivated and the methods used to recreate the charged particle dynamics with molecular dynamics simulations are explained. Section 3.3 presents an analysis of both experimental and simulated results focusing on the effect of ultrafast electron cooling observed in the microplasma. The last section 3.4 briefly summarizes the results.
Results presented in this chapter have been published in an earlier publication [69]. Data recording and evaluation was performed in close cooperation with Tobias Kroker with contributions by Juliette Simonet and Philipp Wessels-Staarmann.

## 3.1 A brief introduction to ultracold plasma

Although most of our immediate environment is in a solid, liquid or gaseous state, we also encounter matter in plasma states in the form of lightning or flames. The majority of mass in our solar system is concentrated in the sun, where the plasma state is dominant. Thus, it is plausible that indeed most of the visible universe is made of plasma. Plasma systems ranging from ionized nebula to the solar core and corona or the core of Jovian planets [110] might suggest that most plasmas are either of astronomical proportion or exceeding temperatures of $1 \times 10^4$ K. However, with the advent of laser cooling techniques a regime of small, millimeter-sized plasma with ion and electron temperatures on the order of 1 K became accessible [36].
An ensemble of ions and electrons can be considered to be in a plasma state, when the collective behavior of the particles becomes dominant over the individual dynamics. This collective behavior can be associated with the Debye length:

$$\lambda_\mathrm{D} = \sqrt{\frac{\epsilon_0 k_\mathrm{B} T_\mathrm{e}}{\rho_\mathrm{e} e^2}} \tag{3.1}$$

where $\epsilon_0$ is the vacuum permittivity, $k_\mathrm{B}$ is the Boltzmann constant, $T_\mathrm{e}$ and $\rho_\mathrm{e}$ are temperature and number density of the electron component and $e$ is the elementary charge. The Debye length can be understood as the length it takes for the electron component to shield external electric fields from penetrating the ensemble [110]. To allow collective plasma dynamics, this length scale has to be smaller then the total system size $\sigma$ to allow for effective shielding ($\lambda_\mathrm{D} \ll \sigma$), setting restrictions to the minimal system size depending on density and temperature.
In ultracold neutral plasma, the temperature is usually derived from an assumed thermalized Maxwell-Boltzmann distribution:

$$T_\mathrm{e,i} = \frac{2E_\mathrm{k,e,i}}{3k_\mathrm{B}} \tag{3.2}$$

Where $E_\mathrm{k,e,i}$ is the kinetic energy of the electron or plasma component and $k_\mathrm{B}$ is the Boltzmann constant. We can then define the coupling parameter $\Gamma_\mathrm{e,i}$ for electrons and ions:

$$\Gamma_\mathrm{e,i} = \frac{e^2}{4\pi\epsilon_0 a_\mathrm{e,i} k_\mathrm{B} T_\mathrm{e,i}} \tag{3.3}$$

where $\epsilon_0$ is the vacuum permittivity, $k_\mathrm{B}$ is the Boltzmann constant, $e$ is the elementary charge, $T_\mathrm{e,i}$ is the temperature of the electron or ion component and $a_\mathrm{e,i}$ is the Wigner-Seitz-radius:

$$a_\mathrm{e,i} = \left(\frac{3}{4\pi\rho_\mathrm{e,i}}\right)^{1/3} \tag{3.4}$$

derived from the number density $\rho_\mathrm{e,i}$ of the electron or ion component. Usually the ionic coupling parameter $\Gamma_\mathrm{i}$ is used to classify the systems into strongly coupled plasma where $\Gamma_\mathrm{i} \geq 1$ and weakly coupled plasma where $\Gamma_\mathrm{i} < 1$. In strongly coupled plasma the Coulomb interaction between particles in the plasma dominates the thermal/kinetic energy present in the system, while weakly coupled plasmas are dominated by the thermal energy. The initial ion coupling parameter can be very high when for example a BEC is ionized. This, however, does not necessarily lead to a strongly coupled plasma as we will see in the course of this chapter, since the coupling parameter is in a strict sense only well defined when the system is in a thermal equilibrium.
For one-component plasma (OCP) with neutralizing electron background, a high coupling parameter indeed leads to interesting dynamics: At a coupling parameter beyond $\Gamma_\mathrm{i} \approx 170$ a spontaneous formation of spatial correlations is predicted [38]. First experimental realizations of self-organizing one-component plasmas were achieved using ensembles of trapped ions [39–41] and fine particles in dusty plasma [42].
However, this simplified view neglects the electron dynamics and the interspecies coupling. For low electron temperatures and high densities, three-body recombination into Rydberg states becomes relevant and leads to heating of the remaining electron gas [45]. Furthermore, in free expanding ultracold neutral plasma the coupling strength is also limited by disorder induced heating [34, 43]. Here, the randomness of the initial ion distribution leads to heating when the ion distribution restructures to avoid small ion-ion distances. Disorder induced heating can be mitigated by starting with a spatially correlated ion distribution, for example by ionizing ultracold atoms in an optical lattice. While earlier photoionization experiments with $^{87}$Rb were conducted with nanosecond

pulses [111], femtosecond timescales offer the possibility to instantly trigger plasma dynamics at BEC densities. The relevant timescale for the electrons in a plasma is given by the inverse of the plasma frequency:

$$\omega_{\mathrm{p,e}}^{-1} = \sqrt{\frac{m_{\mathrm{e}}\epsilon_0}{\rho_{\mathrm{e}}e^2}} \tag{3.5}$$

where $m_{\mathrm{e}}$ is this electron mass, $\epsilon_0$ the vacuum permittivity, $e$ the elementary charge and $\rho_{\mathrm{e}}$ the density of the electron cloud. For a typical BEC density of $2 \times 10^{20}\,\mathrm{m}^{-3}$, $\omega_{\mathrm{p,e}}^{-1}$ amounts to 1.3 ps, suggesting that a nanosecond ionization pulse would indeed perturb the initial dynamics significantly, while a femtosecond pulse can be regarded as instantaneous.
Using a BEC as target sets the ground for a new regime of ultracold plasma by providing an initial charge density that exceeds that of an ultracold gas in a magneto-optical trap by orders of magnitude. This allows for the creation of micrometer sized *ultracold microplasma* with only a few hundred to a few thousand ions and electrons while at the same time permitting relatively high kinetic energies of the electron component on the order of $10^3$ K. In this chapter we discuss a case of microplasma, where the initial electron temperature exceeds the ion temperature by five orders of magnitude and the unfolding dynamics exhibit a unique and striking ultrafast electron cooling.

## 3.2 Ultracold microplasma

Figure 3.1a illustrates the general idea of the experiment. A $^{87}$Rb BEC in the center of the charged particle detector assemblies introduced in section 2.1 is locally ionized by a 511 nm pulse with a duration of $215^{+20}_{-15}$ fs. The ionization products can then be directed by the extraction meshes to the corresponding detectors. The femtosecond laser pulses are focused down to a waist of $w_0 \approx 1\,\mu\mathrm{m}$ in the center of the BEC, yielding peak intensities of up to $2 \times 10^{13}\,\mathrm{W/cm^2}$. At these high peak intensities, the pulse ionizes all the atoms within a cylindrical volume of 1.35 µm radius and 5 µm length (figure 3.1b). At the given wavelength and intensity the ionization occurs via a non-resonant two-photon process (see figure 3.1c). The electrons will carry almost all of the excess energy of 0.678 eV due to the high mass ratio between ions and electrons. At the highest available intensities, the three-photon-process with 3.1 eV can also be observed. Figure 3.1d shows the simulated electron detector images for the energies corresponding to the two- and three-photon ioniziation, as well as a much smaller kinetic energy of 0.01 eV. The latter low-energy signature can be observed when an ultracold plasma is triggered resulting in an ultrafast electron cooling mechanism and will be discussed in the course of this chapter.

### 3.2.1 Local ionization of a BEC

To estimate the geometry of the ionization volume and to predict the fraction of ionized atoms, the ion distribution $\rho_{\mathrm{i}}$ of a locally ionized BEC:

$$\rho_{\mathrm{i}}(x,y,z) = \rho_{\mathrm{TF}}(x,y,z) \times P_I(I(x,y,z)) \tag{3.6}$$

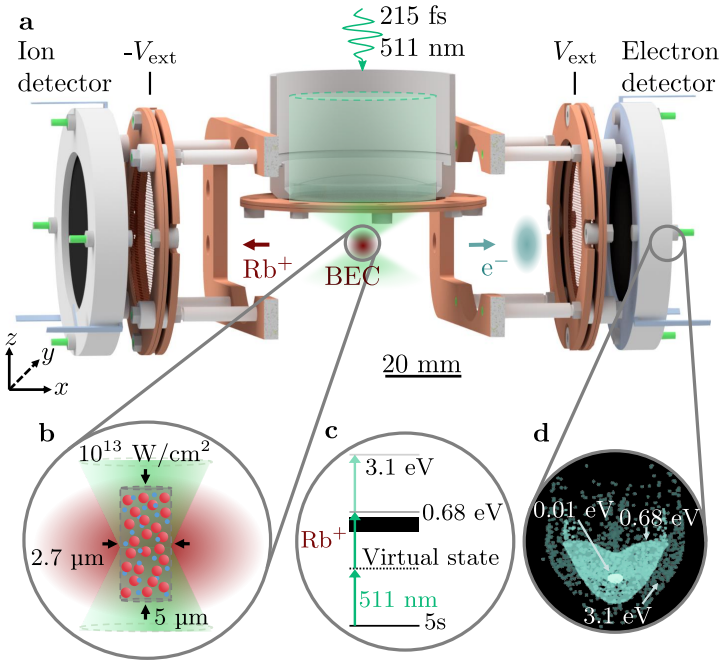


**Fig. 3.1: Creation of an ultracold microplasma**
**a.** A CAD-rendering of the charged particle detector assembly. A single pulse with a pulse duration of 215 fs at 511 nm is used to locally ionize the BEC in the center of the setup. To this end it is focused down to a waist of $\approx 1\,\mu m$. The emerging ions and electrons are separated and drawn to their respective detectors by tunable voltages $\pm V_{ext}$ applied to the extraction meshes. On the way to the detector the electron distribution expands due to its velocity distribution which in turn gets translated into a spatial distribution at the microchannel plate detector. **b.** Due to the high peak intensities of the pulse all atoms along the propagation axis are ionized creating a micrometer sized cylinder filled with ions and electrons within the BEC. **c.** At the given wavelength of 511 nm the ground-state atoms get ionized over a non-resonant two-photon process yielding an excess energy of 0.68 eV. At very high intensities, the three-photon process with an excess energy of 3.1 eV is also detectable. **d.** Electron detector images extracted from charged particle tracing simulations without Coulomb interaction for the initial kinetic energies 0.01 eV, 0.68 eV and 3.1 eV. In contrast to the earlier mentioned simulations in this manner (figure 2.13) the ion MCP was set to ground leading to a slightly different spatial distribution. Figure adapted from [106] and licensed under CC BY 4.0.

can be calculated by taking into account the density profile of the ultracold quantum gas $\rho_{TF}$ as well as the Gaussian beam intensity distribution $I(x, y, z)$ of the inciding femtosecond laser pulse. Here $P_I(I)$ denotes the intensity dependend ionization probability.
The density profile of the BEC $\rho_{TF}$ can be calculated starting from the Gross-Pitaevskii equation (GPE) following the argumentation in [112]:

$$\left(-\frac{\hbar^2\nabla^2}{2m} + V_{ext}(x,y,z,t) + g|\Psi_0(x,y,z,t)|^2\right)\Psi_0(x,y,z,t) = \mu\Psi_0(x,y,z,t) \qquad (3.7)$$

where $\hbar$ is the reduced Planck constant, $m$ is the mass of a $^{87}$Rb atom, $V_{\text{ext}}(x,y,z,t)$ an external potential and $g = 4\pi\hbar^2 a/m$ the interatomic coupling constant with the $s$-wave scattering length $a$. $\Psi_0$ denotes the order parameter of the BEC and can be identified with the square root of the density $\Psi_0 = \sqrt{\rho_{\text{TF}}}$ while $\mu$ is the chemical potential.
As external potential we use the harmonic approximation of the potential of our crossed dipole trap after evaporation:

$$V_{\text{ext}}(x,y,z) = \frac{m}{2}\left(\omega_x^2 x^2 + \omega_y^2 y^2 + \omega_z^2 z^2\right) \tag{3.8}$$

with the measured trap frequencies [69] of $\omega_{x,y} = 2\pi\times 113(3)\,\text{Hz}$ and $\omega_z = 2\pi\times 128(1)\,\text{Hz}$ resulting in an almost spherically symmetric potential.
In the Thomas-Fermi limit, where the kinetic energy is neglected in the GPE, the order parameter and thus the atomic density can be written as:

$$|\Psi_0(x,y,z)|^2 = \rho_{\text{TF}}(x,y,z) = \begin{cases} \frac{1}{g}(\mu_{\text{TF}} - V_{\text{ext}}(x,y,z)) & ,\ \mu_{\text{TF}} \geq V_{\text{ext}}(x,y,z) \\ 0 & ,\ \mu_{\text{TF}} < V_{\text{ext}}(x,y,z) \end{cases} \tag{3.9}$$

where $\mu_{\text{TF}}$ is the chemical potential which, with the correct normalization of the order parameter to the density, amounts to:

$$\mu_{\text{TF}} = \frac{\hbar\omega_{\text{ho}}}{2}\left(\frac{15Na}{\sqrt{\hbar/(m\omega_{\text{ho}})}}\right)^{2/5} \tag{3.10}$$

where $\omega_{\text{ho}} = (\omega_x\omega_y\omega_z)^{1/3}$ and $N$ is the number of particles in the condensate.
With the aforementioned measured trap frequencies of the crossed dipole trap and the particle number extracted from absorption imaging of $N = 4.2(3)\times 10^4$ atoms the calculated density distribution following equation (3.9) results in an almost spherical parabolic density profile with a peak density of $\rho_{\text{BEC}} = 2\times 10^{20}\,\text{m}^{-3}$.
To calculate the ionization probability $P_I$ in equation (3.6) we first calculate the intensity profile of the Gaussian beam of the femtosecond laser focused by the microscope objective:

$$I(x,y,z) = I_0 \cdot \frac{w_{x,0}w_{y,0}}{w_x(z)w_y(z)} \cdot \exp\left(\frac{-2x^2}{w_x(z)^2}\right)\exp\left(\frac{-2y^2}{w_y(z)^2}\right) \tag{3.11}$$

with the beam waists in $x$ and $y$ direction $w_{x,y} = w_{x,y,0}\cdot\sqrt{1+(\frac{z}{z_{\text{R},x,y}})^2}$, where $z$ is the propagation axis of the beam and $w_{x,y,0}$ are the waists of the focus in $x$ and $y$ direction, while $z_{\text{R},x,y}$ denotes the corresponding Rayleigh lengths. $I_0$ is the peak intensity of the ionizing pulses:

$$I_0 = \frac{2P_0}{\pi w_{x,0}w_{y,0}} = \frac{4E_{\text{P}}\sqrt{2\ln 2}}{\pi w_{x,0}w_{y,0}\sqrt{2\pi}\tau_{\text{P}}} \tag{3.12}$$

where $P_0$ is the peak power of the pulse, which can also be written in terms of the pulse energy $E_{\text{P}}$ and the FWHM duration $\tau_{\text{P}}$. The beam waist of the focusing objective was measured to be $w_{x,y,0} = 1.00(4)\,\mu\text{m}$.
For simplicity equation (3.11) only covers the case where the focus is centered on $x = y = z = 0$ and the pulse propagates along the $z$-axis. However, the intensity

profile can be easily generalized for arbitrary focal positions and arbitrary angles.
The ionization probability $P_I(I)$ is nonlinear in the intensity. The corresponding ionization cross sections for the two-photon process at 511 nm were measured and calculated via TDSE-calculations in an earlier publication of our group [33] and used for the calculation. The combination of the density profile of the atomic target, the intensity profile of the ionizing pulse and the intensity dependent ionization probability then leads to the ion density illustrated in figure 3.2a: Shown is a central cut through the $xz$-plane of the cloud (at $y = 0$). The femtosecond laser pulse with a peak intensity of $I_0 = 1.9 \times 10^{13}\,\mathrm{W/cm^2}$ (corresponding to $E_\mathrm{P} = 68\,\mathrm{nJ}$) propagates along the $z$-axis. Darker colors mark regions with higher ion density. In the central region the ion density is identical to the peak density of the BEC.
Figure 3.2b illustrates the locality of the ionization: the red line marks the outline of the Thomas-Fermi density profile of the cloud which is identical for $x$ and $y$ and differs only slightly for the $z$-axis due to almost identical trap frequencies. The turquoise line gives the ionization probability along the $x$-axis which approaches unity only in the central region with sharp edges suggesting that the ionization can be considered local along $x$. This also holds true for the $y$-axis due to the spherical symmetry of the cloud and the radial symmetry of the Gaussian beam. The dotted black line shows the ionization probability along the $z$-axis, which is unity throughout the atomic target - all atoms along the propagation axis of the pulse are ionized. The corresponding volume of ionized atoms can safely be approximated by a cylinder with a radius of 1.35 µm (set by the waist of the focus of the femtosecond laser pulser) and a height of 5 µm (determined by the size of the atomic cloud). Within this volume approximately 4000 atoms get ionized at the discussed intensity.

### 3.2.2 Conditions for plasma formation

When a plasma forms after photoionization of the atoms, some of the free electrons created in the ionization process will get trapped by the total Coulomb potential of the remaining ions. As soon as this Coulomb potential is deeper than the excess energy of the electrons $\Delta E$, the first electron will get trapped. Since the depth of the ionic Coulomb potential depends on the number of ions, this threshold can be characterized by the minimum number of ions for plasma formation $N^*$. An increasing number of ions beyond this threshold will simply increase the number of trapped electrons. For a Gaussian density distribution common to ultracold neutral plasma the critical ion number is [36]:

$$N^* = \frac{\Delta E}{U_0} \text{ with } U_0 = \frac{\sqrt{2/\pi}e^2}{4\pi\epsilon_0\sigma} \tag{3.13}$$

with the elementary charge $e$, the vacuum permittivity $\epsilon_0$, the electrons excess energy $\Delta E$ and the root mean square (RMS) radius of the ionic cloud $\sigma$.
Although we clearly expect a non-Gaussian distribution in our setup, we estimate the critical number of ions by using the arithmetic mean radius $\bar{\sigma} = (2r + h/2)/3 = 1.73\,\mu\mathrm{m}$ of the approximated cylindrical ionization volume discussed in section 3.2.1 , leading to

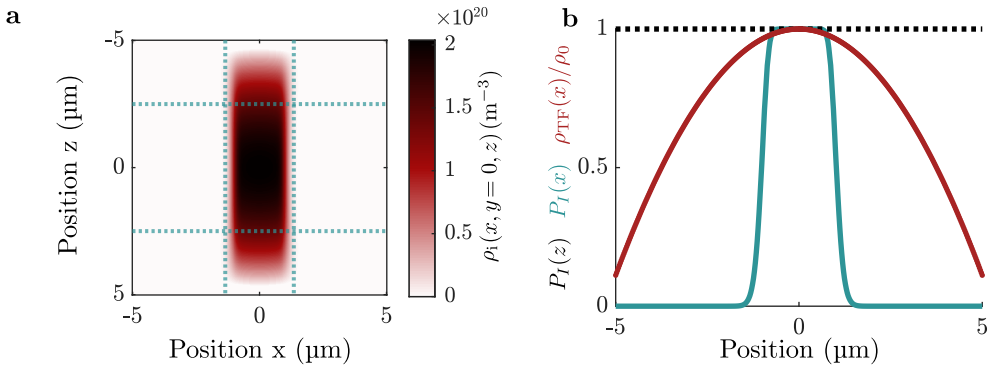


**Fig. 3.2: Calculated ion density in a locally ionized BEC.**
**a.** A BEC with a density of $\rho_{\mathrm{BEC}} = 2 \times 10^{20}\,\mathrm{m}^{-3}$ is locally ionized by a femtosecond pulse with a wavelength of 511 nm and a beam waist of 1 µm at a peak intensity of $I_0 = 1.9 \times 10^{13}\,\mathrm{W/cm}^2$. Plotted is the calculated ion density in the central $xz$-plane at $y = 0$ of the atomic cloud. Darker colors indicate a higher density. The dotted lines mark the edges of a cylinder with a radius of 1.35 µm and a height of 5 µm that we use as approximated ionization volume in the CPT simulations discussed in the following sections. **b.** Ionization probability $P_I$ plotted against the position in the cloud along the $z$-axis (dotted black line) and the $x$-axis (turquoise line). The red line indicates the outline of the (spherically symmetric) Thomas-Fermi density profile $\rho_{\mathrm{TF}}/\rho_0$ of the cloud. While all atoms along the pulse propagation axis ($z$) get ionized, only a small fraction of the cloud is ionized along the $x$- and $y$-axis and the ionization can be considered as local. Figure adapted from [106] and licensed under CC BY 4.0

$N^* = 1023$ ions. This number is significantly lower than the calculated 4000 ions and electrons expected in this volume, indeed suggesting the formation of a plasma.

### 3.2.3 Molecular dynamics simulations of the plasma dynamics

To understand the emerging plasma dynamics, we perform molecular dynamics simulations of the charged ionization products within the COMSOL Multiphysics® model of our detector setup as discussed in section 2.5.1 as well as in an empty field free environment. A notable difference to the previously described setup is, that the front of the ion MCP is set to ground instead of 1 kV and the back of the MCP and phosphor screen are also turned off. For the results presented in the course of this chapter we do not use the ion detector. This yields a different field configuration than shown in figure 2.12 in the high voltage mode of operation, whereas the low voltage mode of operation with $V_{\mathrm{ext}} = 5\,\mathrm{V}$ is used exactly as described in section 2.5.1.
The particle distributions we use for the simulations are generated by using the approximated cylindrical volume described in figure 3.2 filled with a uniform random distribution of $N_{\mathrm{e,i}} = 500$ or $N_{\mathrm{e,i}} = 4000$ ions and electrons.
The electrons are generated with an isotropic and monochromatic velocity distribution, with a kinetic energy of 0.678 eV, corresponding to the excess energy of the two-photon ionization at 511 nm and translating into an initial temperature of $T_{\mathrm{e}} \approx 5250\,\mathrm{K}$ (eq. (3.2)). Here, the isotropy of the distribution neglects the expected anisotropy of the angular distribution of the ionization process discussed in section 2.5.3. The monochro-

maticity is a valid simplification here since the bandwidth of the two-photon ionization process of $\sigma_{\mathrm{E}} \approx 9\,\mathrm{meV}$ is much smaller than the excess energy.
The initial thermal energy of the ions can safely be neglected (they start with the temperature of the BEC in the nK-regime), instead we only take the recoil from the ionization process with a kinetic energy of $4.3\,\mu\mathrm{eV}$ into account yielding a temperature of $T_{\mathrm{i}} = 33\,\mathrm{mK}$. For the simulation we again chose an isotropic monochromatic distribution for simplicity.
The emerging plasma dynamics in the system is a direct effect of the many-body Coulomb interaction between the ions and electrons. In the simulations, the Coulomb interaction is taken into account with a short-range cutoff to omit the divergence of the force for small interparticle distances:

$$F_{\mathrm{C}} = \begin{cases} \frac{1}{4\pi\epsilon_0}\frac{q_1 q_2}{r^2} & , \; r > R_0 \\ \frac{1}{4\pi\epsilon_0}\frac{q_1 q_2}{R_0^2} & , \; r \leq R_0 \end{cases} \tag{3.14}$$

Here $\epsilon_0$ is the vacuum permittivity, $q_1$ and $q_2$ are the charges of the interacting particles, $r$ denotes the distance between these particles and $R_0$ is the cutoff distance, which we set to 20 nm. The solver of the charged particle tracing module of the COMSOL Multiphysics® software uses somewhat intransparent dynamic time steps i.e. for dense systems with fast dynamics it automatically chooses smaller time steps for the calculation. As the system expands, the time steps become larger, effectively reducing the calculation time. In order to calibrate the cutoff distance to fit our simulated system, we check the overall dynamics for energy conservation.
The cutoff distance is chosen to be smaller than the initial particle distance characterized by the Wigner-Seitz radius $a_{\mathrm{i,e}} = 106\,\mathrm{nm}$ (equation (3.4)) for an initial density of $\rho_{\mathrm{BEC}} = 2 \times 10^{20}\,\mathrm{m}^{-3}$. However, it prevents us from making suitable predictions concerning close-range interactions between electrons and ions like for example three-body recombination into bound states. A more comprehensive discussion of molecular dynamics simulations for plasma simulations can be found in chapter 4 using a different tool for simulation.

## 3.3 Ultrafast electron cooling

The unique initial conditions discussed in the previous section yield a striking feature of the plasma dynamics observed in our experiments. The large initial density, the small volume and the high excess energy imposed on the electrons lead to a fascinating ultrafast electron cooling, that will be further illuminated in the course of this section by comparing experimental results with the simulated dynamics down to the picosecond.

### 3.3.1 Measuring the kinetic energy of the electrons

Figure 3.3a-c shows false color images of the averaged electron signal at pulse peak intensities of $1.7 \times 10^{12}\,\mathrm{W/cm^2}$, $3.8 \times 10^{12}\,\mathrm{W/cm^2}$ and $1.9 \times 10^{13}\,\mathrm{W/cm^2}$ in the high voltage mode of operation with $V_{\mathrm{ext}} = \pm 300\,\mathrm{V}$. The images shown are averaged over 18(a), 23(b) and 22(c) experimental realizations. When comparing the recorded detector images to the charged particle tracing simulations without Coulomb interaction in

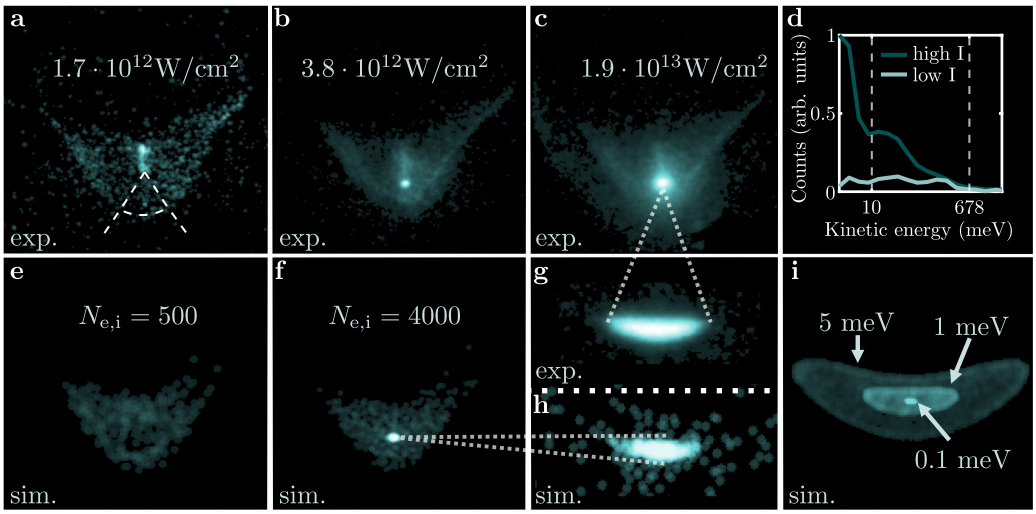


**Fig. 3.3: Direct measurement of electron energies.**
**a-c.** False color image of the electron signal at $V_{ext} = \pm 300\,\mathrm{V}$ with pulse peak intensities of $1.7 \times 10^{12}\,\mathrm{W/cm^2}$, $3.8 \times 10^{12}\,\mathrm{W/cm^2}$ and $1.9 \times 10^{13}\,\mathrm{W/cm^2}$ averaged over 18, 23 and 22 realizations. The structure on the detector at the lowest intensity (a) corresponds to electrons that carry the excess energy of 0.68 eV from the ionization process. As the number of charged particles increases with intensity, the conditions for the formation of a plasma is fulfilled and a bright dot appears on the detector (b-c). These electrons are cooled by the plasma dynamics to energies below 0.01 eV. **c.** At high peak intensities a large structure associated to the three-photon process at 3.1 eV appears (compare with figure 3.1c-d) and the amount of cold electron increases. **d.** The plot shows the counts for $1.7 \times 10^{12}\,\mathrm{W/cm^2}$ and $3.8 \times 10^{12}\,\mathrm{W/cm^2}$ (a,c) integrated over the circular section shown in (a). The vertical dashed lines at 0.01 eV and 0.678 eV mark the outer radii of the corresponding simulated images without Coulomb interaction (figure 3.1d). While at low intensity the distribution is flat up to the two-photon excess energy, we see a strong peak at high intensities at energies below 0.01 eV associated with the plasma electrons and the center of mass of the escaping electrons is shifted towards lower energies. **e.** Depicted is the detector image extracted from a molecular dynamics simulation with 500 electrons and ions. Here, no plasma signature is visible and the structure shows good agreement with the experimental image in (a). **f.** A molecular dynamics simulation with 4000 electrons and ions shows the cold electrons from the plasma dynamics in good agreement with (b). **g.** At $V_{ext} = \pm 5\,\mathrm{V}$ the recorded detector images can be understood as a zoom-in into the central region of cold electrons. **h.** A corresponding molecular dynamics simulation at $V_{ext} = \pm 5\,\mathrm{V}$ again shows excellent agreement with the experimental data in spite of the challenges due to the very small extraction gradient. **i.** Charged particle tracing simulations neglecting Coulomb energy show a good resolution below 5 meV and suggest that the electrons emerging from the plasma have kinetic energies between 5 and 1 meV (both in experiment and simulation (g,h)). Figure adapted from [106] and licensed under CC BY 4.0.

figure 3.1d it becomes evident, that the spatial structure visible on the detector image for the lowest intensity is in excellent agreement with the electrons emerging from the two-photon ionization process with an excess energy of 0.68 eV. As stated before, this kinetic energy can be identified with a temperature of $T_e = 5250\,\mathrm{K}$.

In figure 3.3c, at the highest intensity recorded, electrons from the three-photon process become visible as an underlying larger structure on the detector (compare to the simulated electron distribution with a kinetic energy of 3.1 eV in figure 3.1d).
Besides these two energy classes of electrons that directly originate in the strong-field ionization, a third class of electrons is visible on the experimental images for the higher intensities (3.3b and c): A small bright dot near the center corresponding to very small kinetic energies comparable to the 0.01 eV-feature in figure 3.1d appears. These cold electrons are a result of the plasma dynamics emerging from the local ionization of the ultracold atoms.
The average of the brightness within the circular section marked by the dashed line in figure 3.3a for the lowest intensity is shown in figure 3.3d and compared to the same averaged section from the image corresponding to $3.8 \times 10^{12}\,\mathrm{W/cm^2}$ (figure 3.3b). The white dashed vertical lines marking 10 meV and 678 meV are the outlines of the simulated signal in figure 3.1d. This allows us to get a more quantitative measure of the kinetic energy of the electrons. At the lowest intensity the resulting profile from the experimental images is basically flat up to the energy belonging to the two-photon process. At the higher intensity a sharp peak appears below 10 meV, corresponding to the small bright spot in the detector images and a temperature of 77 K. Furthermore, the distribution for the higher intensity is not flat, but the overall center of mass is shifted towards lower energies.
The cold electrons below 77 K are plasma electrons that are decelerated by the initial charge separation and the expansion of the plasma, as we discuss in the next section. The overall shift to lower energies is also an effect of the initial charge separation: As the atoms are ionized, some of the electrons leaving the ionization volume are decelerated by the positive charge left behind, resulting in an overall shift towards smaller energies. An increase in intensity also yields an increase in charged particles, amplifying the trapping and deceleration of electrons. This can also be seen in the decreasing area of the two-photon signature in the detector images in figure 3.3a-c.
The effect of the plasma dynamics on the electrons visible in these measurements can be reproduced with molecular dynamics simulations of the system as discussed in section 3.2.3. The results for simulations within the virtual model of our detector assembly are shown in figure 3.3e for $N_{\mathrm{e,i}} = 500$ and in figure 3.3f for $N_{\mathrm{e,i}} = 4000$ ions and electrons. The simulations are in excellent agreement with the experimental images in figure 3.3a and b and it is evident, that the cold plasma electrons emerge only for a number of charged particles exceeding the critical number for the formation of a plasma.
As was discussed in figure 2.13 of section 2.5.2, operating the detector assembly with a lower extraction voltage of $V_{\mathrm{ext}} = \pm 5\,\mathrm{V}$ provides a better energy resolution for the very small kinetic energies down to approximately 1 meV. Figure 3.3g shows a false color detector image for $I_0 = 1.9 \times 10^{13}\,\mathrm{W/cm^2}$ averaged over 14 realizations for this configuration. The electron signal displayed can be understood as a magnification of the bright spot in the center of figure 3.3c, as indicated by the dashed white lines.
In figure 3.3i the simulated detector images for electrons with kinetic energies of 5, 1 and 0.1 meV and without Coulomb interaction are depicted. Comparing the simulated and the experimental image, we can conclude that the measured slow electrons have a kinetic energy of $E_{\mathrm{kin}} \approx 1\,\mathrm{meV}$ or a temperature of $T_e \approx 8\,\mathrm{K}$.
Figure 3.3h shows a detector image extracted from the molecular dynamics simulation

of the plasma including the Coulomb interaction between the particles in the same voltage configuration for $N_{e,i} = 4000$. Again, the dashed lines indicate that this can be understood as a magnification of the cold electron signature in the simulated detector image in figure 3.3f due to the lower extraction field. The kinetic energy of the electrons in the simulated case is consistent with the experimentally determined energy in figure 3.3g and can also be estimated to have an upper boundary of $E_{kin} \approx 1\,\text{meV}$. Despite the challenging low field regime, the simulation shows again excellent agreement with the experimental data.

### 3.3.2 Simulated plasma dynamics

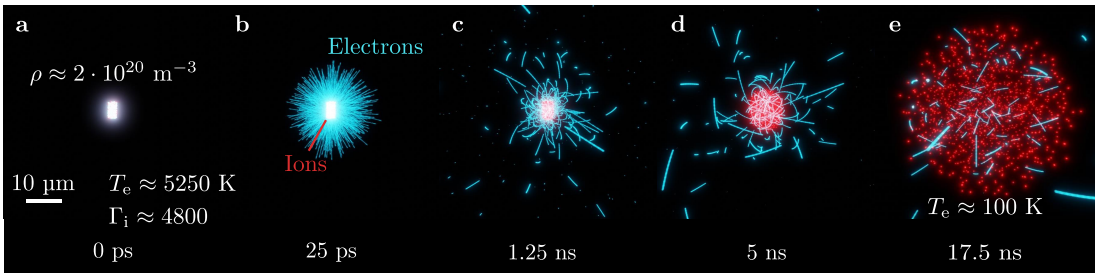


**Fig. 3.4: Snapshots from a molecular dynamics simulation of the plasma dynamics.** **a.** The first snapshot shows the initial particle configuration: ions (red) and electrons (blue) are homogeneously distributed in a cylindrical volume with a density of $\rho \approx 2 \times 10^{20}\,\text{m}^{-3}$. The high excess energy of the photoionization yields an electron temperature of $T_e \approx 5250\,\text{K}$ while the low temperature of the ions leads to a high initial coupling parameter of $\Gamma_i \approx 4800$. **b.** Within the first picoseconds most of the electrons leave the ionization volume due to their high kinetic energy leaving behind a positively charged ionic core. In the process the plasma electrons experience a rapid cooling with a loss of about 50 % of their initial kinetic energy. **c.** The charge separation decelerates the emerging electrons and traps about half of them in an ultracold plasma with trajectories around and through the ion cloud. **d.** On the nanosecond timescale the ion cloud starts to expand due to Coulomb repulsion, leading to a decrease in the depths of the collective Coulomb potential and further electron cooling. **e.** The continuing expansion leads after 17.5 ns to an electron temperature of $\approx 100\,\text{K}$. Figure adapted from [106] and licensed under CC BY 4.0.

The excellent agreement between the molecular dynamics simulations and the measured electron distributions at the detector allows us to draw conclusions on the underlying dynamics. The nature of these simulations allows us to follow the position and momentum of each individual particle on a picosecond timescale.
Regarding the appearance of the cold electrons they reveal two distinct mechanisms that lead to a reduction in kinetic energy of the plasma electrons: An ultrafast cooling process after the instantaneous creation of the plasma within the first picoseconds and a slower process driven by the expansion of the system on a nanosecond timescale.
Figure 3.4a-e illustrates the evolution of the plasma. The images are renderings of simulation data, blue lines mark the trajectories of the electrons, red dots/lines mark the trajectories of the ions. The lengths of the lines are a qualitative measure of the speed of the particles.

In figure 3.4a the initial conditions are shown: $N_{e,i} = 4000$ electrons and ions are generated in the cylindrical ionization volume yielding a peak density of $\rho_{i,e} \approx 2 \times 10^{20}\,\mathrm{m}^{-3}$. The initial kinetic energy of the electrons is set to the excess energy of the two-photon process of 0.68 eV corresponding to a temperature of $T_e = 5250\,\mathrm{K}$. The initial coupling parameter of the ions amounts to $\Gamma_i \approx 4800$ (eq. (3.3)) due to the high density and the low kinetic energy of 33 mK.
Because of their high kinetic energy, most of the electrons leave the ionization volume within the first few picoseconds as illustrated in figure 3.4b. On this timescale the ions can be regarded as static. This charge separation leads to a deceleration of the electrons leaving the volume and an associated loss of kinetic energy. The ions in turn experience a gain in potential energy of the same magnitude due to the reduced electron density and reduced Coulomb shielding.
In figure 3.4c we see that after 1.25 ns some electrons have escaped the system (blue distant dots in the background), while some electrons are forced on orbital trajectories around and through the ion cloud (plasma electrons).
Within the next nanoseconds (figure 3.4d-e) the ion cloud expands, transferring the potential energy of the ions into kinetic energy. During the expansion the depth of the collective ionic Coulomb potential that the electrons are bound to decreases and the electrons experience a further reduction of kinetic energy, reaching temperatures on the order of 100 K after 17.5 ns (figure 3.4e).

### A microscopic view on the electron dynamics

To understand the collective dynamics of the ultrafast electron cooling, we first look at the microscopic electron dynamics:
In figure 3.5 exemplary trajectories of a selection of electrons from a molecular dynamics simulation are plotted. In this case a simulation without extraction field with $N_{e,i} = 4000$ electrons and ions initially distributed in the aforementioned cylindrical ionization volume was chosen for illustrative purposes. Given is the distance of the particles from the center of the ionization volume in dependency on the time. The red line marks the maximum ion radius i.e the ion that is furthest away from the center. The dashed red line gives the RMS radius of all ions. The black lines illustrate the trajectories of 25 escaping electrons that are not bound to the plasma and quickly leave the ionization volume right after ionization. These are electrons that contribute to the charge separation in the system, leaving behind unpaired ions in the plasma. The trajectories of 25 electrons with close orbits are plotted in light turquoise - these are plasma electrons, that are bound to the ionic Coulomb potential and move on trajectories mostly within the ion cloud. The dark turquoise lines are electrons on wider orbits that are most of the time outside of the ionic cloud. The common picture of an ultracold neutral plasma is that of overlapping electron and ion plasma with the same extent. In contrast, for the charged ultracold microplasma the electronic component can be significantly larger than the ionic component.
For the quantitative analysis of the collective dynamics we only differentiate between *escaping electrons* and *plasma electrons*:
In the simulations without extraction field, plasma electrons are all electrons that are still within two times the maximum ion radius at the end of the simulation time

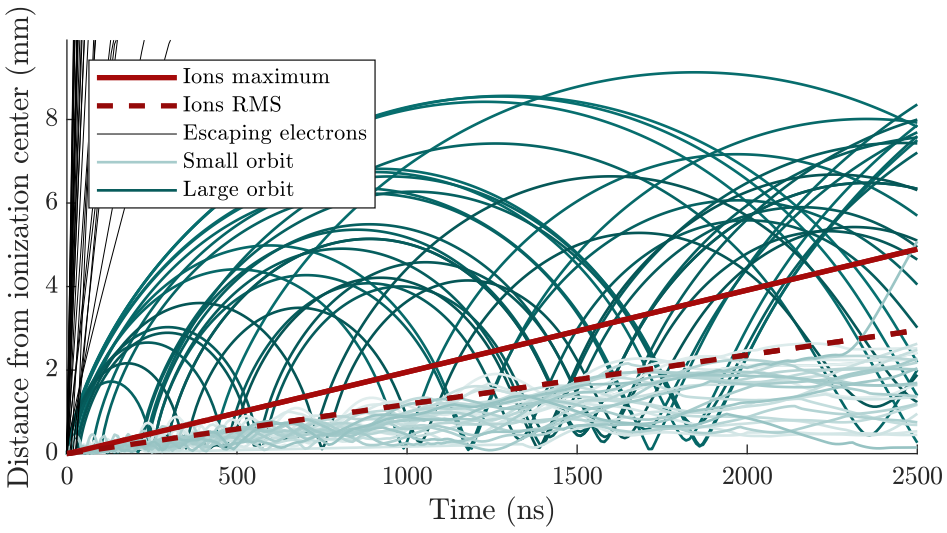


**Fig. 3.5: A microscopic view on the electron trajectories.**
The plot shows the particle distance to the center of the ionization volume in dependence on the time for a selection of electrons from the molecular dynamics simulation without extraction field. The red line is the maximum ion radius, the dashed red line is the RMS radius of all ions which corresponds to the extent of the ion cloud. The thin black lines are 25 escaping electrons, that are not bound to the collective Coulomb potential. The plasma electrons can be distinguished into two different classes: in light turquoise a selection of 25 electrons is plotted. These electrons are most of the time within the ion cloud. In dark turquoise 25 electrons with large orbits around the ion cloud are plotted. These trajectories are only possible due to the finite size of the initial charged particle distribution and high initial excess energy.

$T_{\mathrm{end}} = 2.5\,\mu\mathrm{s}$. All electrons outside this radius are assumed to have escaped the Coulomb potential. For the simulations with extraction field, the situation is more difficult, since the extraction field slowly pulls the electrons from larger orbits out of the plasma and to the detector. Over time approximately 80 % of the plasma electrons get pulled out of the system this way. To this end, we consider electrons as plasma electrons that are not further than 1 mm from the ionization center after either 40 ns for $V_{\mathrm{ext}} = \pm 300\,\mathrm{V}$ or 300 ns for $V_{\mathrm{ext}} = \pm 5\,\mathrm{V}$. For later times the extraction field becomes dominant over the Coulomb potential of the ionic cloud. A much better definition of the different electron classes will be introduced and discussed for the molecular dynamics simulations close to the ionization threshold in chapter 4 but was not part of the publication regarding the ultrafast electron cooling.

### Macroscopic dynamics: Charge separation

The collective dynamics of the ultracold microplasma can be best understood in terms of mean energies per particle. Figure 3.6a shows the initial development of the mean total energy per particle of all electrons and ions (turquoise and red) and the mean kinetic energy per particle of the electrons trapped in the plasma (light turquoise) for the aforementioned simulation in a field-free environment. The total energy is determined

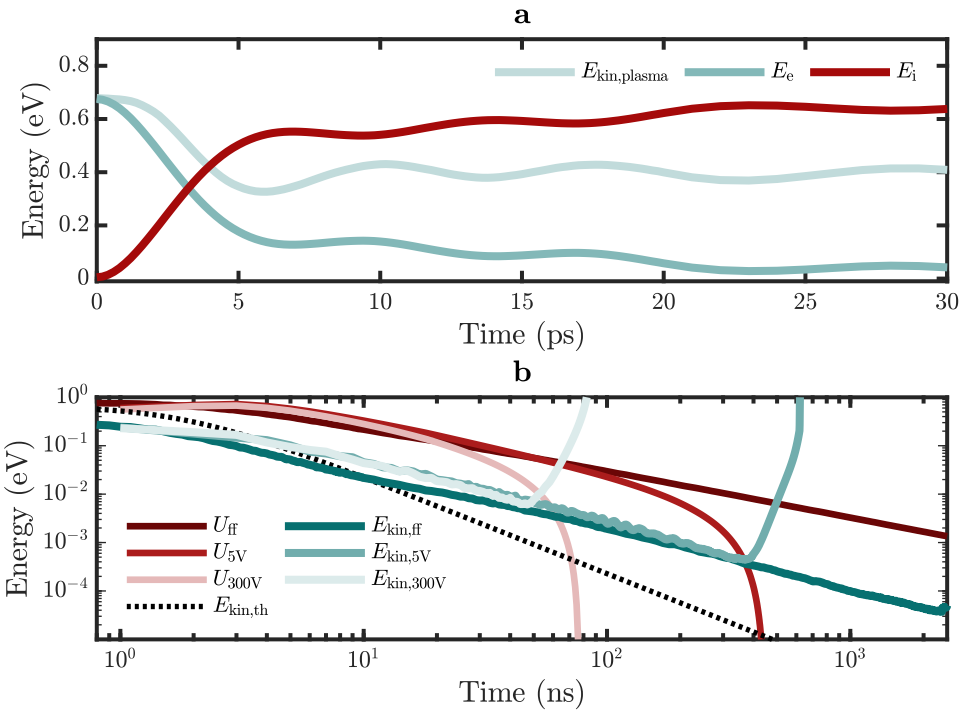


**Fig. 3.6: Plasma dynamics on picosecond to nanosecond timescale.**
**a.** The plot shows the development of the mean kinetic energy per particle of the plasma electrons (light turquoise) and the mean total energy per particle for the electrons (turquoise) and ions (red) in the first 30 ps of the evolution. The data is extracted from a molecular dynamics simulation without extraction field. The kinetic energy of the plasma electrons drops by approximately 50 % within the first 7 ps and is converted into potential energy of the ions due to charge separation when the electrons leave the ion cloud. **b.** Plotted is the mean kinetic energy per particle and the effective depth of the collective potential $U_{\mathrm{eff}}$ (eq. (3.18)) in dependence on the time for molecular simulation simulations with $V_{\mathrm{ext}} = \pm 300\,\mathrm{V}$ (light turquoise, light red), $V_{\mathrm{ext}} = \pm 5\,\mathrm{V}$ (turquoise, red) as well as in a field free environment (dark red, dark turquoise). The black dotted line is the kinetic energy for expansion driven electron cooling predicted by a hydrodynamic model (eq. (3.16)) which quickly deviates from our simulations by orders of magnitude. On the nanosecond timescale the kinetic energy of the electrons decreases due to the expansion of the ionic cloud and the decrease in the depth of the Coulomb potential. The sharp rising edges in the kinetic energies for the simulations with extraction field mark the point in time when the extraction field becomes dominant over the binding Coulomb potential of the ionic cloud and the plasma electrons get accelerated towards the detector. Figure adapted from [106] and licensed under CC BY 4.0.

by the sum of kinetic and potential energy. The dynamics in the first picoseconds of the evolution is driven by the charge separation: Most of the electrons initially leave the ionization volume and approximately half of the electrons escape the plasma completely, leaving behind a large charge imbalance. The trapped plasma electrons loose approximately half of their initial kinetic energy within the first 7 ps which gets transferred into potential energy of the ions. At this point the potential energy of

the ions is dominated by ion-ion-repulsion and has a positive sign, while the potential energy of the plasma electrons is dominated by the ion-electron attraction and has a negative sign. This leads to the mean total energy of all electrons (dark turquoise) being smaller than the kinetic energy of the plasma electrons.
A closer look at the energies reveals a dampened oscillation with a period of the same order than the initial duration of charge separation of 7 ps which is in good agreement to the expected timescale given by the plasma frequency in equation (3.5) of $T = 2\pi/\omega_{\mathrm{p,e}} = 7.9\,\mathrm{ps}$. Dephasing of the electron trajectories (figure 3.5 showed a variety of oscillation frequencies from the MHz to the GHz range) explains the dampening of the oscillation. Depending on its initial position and charge environment, each electron looses a different amount of kinetic energy during the charge separation resulting in a continuum of orbital sizes and oscillation periods.
Eventually, the loss of about half of the kinetic energy of the plasma electrons within the first 7 ps can be understood as an ultrafast cooling from 5250 K to about 2500 K with an unprecedented cooling rate of $\approx 400\,\mathrm{K/ps}$.

### Macroscopic dynamics: Coulomb expansion

The second process of the macroscopic dynamics contributing to the low electron energies measured in the experiment is the Coulomb expansion of the ionic cloud on a nanosecond timescale: Here, potential energy stored in the ions as a result of the initial charge separation gradually translates into kinetic energy of the ions. The expansion of the cloud leads to a further reduction of the kinetic energy of the electrons.
In an ultracold neutral plasma the expansion dynamics can be described by a hydrodynamic model after an equilibration phase [113]. For these systems the expansion is driven by the thermal pressure of the components yielding the hydrodynamic expansion velocity [34]:

$$v_{\mathrm{hyd}} = \sqrt{k_{\mathrm{B}}(T_{\mathrm{e},0} + T_{\mathrm{i},0})/m_{\mathrm{i}}} \tag{3.15}$$

where $k_B$ is the Boltzmann constant, $T_{\mathrm{e,i},0}$ are the initial electron/ion temperatures and $m_{\mathrm{i}}$ is the ion mass. For the initial temperatures in our system this would amount to $v_{\mathrm{hyd}} = 710\,\mathrm{m/s}$. From the evolution of the RMS ion radius shown in figure 3.5 we can extract an asymptotic expansion velocity of $v_{\mathrm{exp}} = 418\,\mathrm{m/s}$ that is smaller than the result for the hydrodynamic model. Since the microplasma we investigate is highly charged and driven by Coulomb forces instead of thermal pressure a discrepancy is to be expected.
The expected evolution of the kinetic energy of the electrons a hydrodynamic expansion in an ultracold neutral plasma is plotted in figure 3.6b (dotted black line), with:

$$E_{\mathrm{kin,th}}(t) = E_{\mathrm{kin,e}}(0)(1 + t^2/\tau_{\mathrm{exp}}^2)\ ,\ \text{with}\ \tau_{\mathrm{exp}} = \sqrt{m_{\mathrm{i}}\sigma^2/[k_{\mathrm{B}}(T_{\mathrm{e},0} + T_{\mathrm{i},0})]} \tag{3.16}$$

where $E_{\mathrm{kin,e}}(0)$ is the initial kinetic energy of the electrons, while $m_{\mathrm{i}}$ is the ion mass, $\sigma$ the initial ion RMS radius and $k_{\mathrm{B}}$ the Boltzmann constant. $T_{\mathrm{e,i},0}$ denote the initial ion and electron temperatures.
Compared to the results of our molecular dynamics simulation for $V_{\mathrm{ext}} = \pm 300\,\mathrm{V}$ (light turquoise), $V_{\mathrm{ext}} = \pm 5\,\mathrm{V}$ (turquoise) and a field-free environment (dark turquoise), we

observe that the hydrodynamic model also covers an expansion-driven electron cooling. Yet it does not capture the initial ultrafast electron cooling by charge separation we observe in our system and the calculated energy quickly diverges from the energies in our simulations by orders of magnitude.
To estimate the depth of the ionic potential in our molecular dynamics simulations we first simplify the Coulomb potential of the cloud by assuming a homogenously charged sphere with the potential:

$$U(r) = \begin{cases} \frac{Q}{8\pi\epsilon_0 R}(3 - \frac{r^2}{R^2}), & r \leq R \\ \frac{Q}{8\pi\epsilon_0 r}, & r > R \end{cases} \tag{3.17}$$

where $\epsilon_0$ is the vacuum permittivity, $R$ the maximum ion radius and the total charge $Q$ given by $e \cdot N_{\text{diff}}$. Here $e$ is the elementary charge and $N_{\text{diff}}$ the difference between the number of ions and electrons within the sphere.
For the simulations with extraction fields we also have to take the effect of the extraction field into account.

$$U_{\text{eff}}(r) = U(r) - E_{\text{ext}} \cdot r \tag{3.18}$$

We simplify the inhomogeneous extraction field to a linear field $E_{\text{ext}}$ with $E_{\text{ext,300V}} = 162\,\text{V/m}$ for $V_{\text{ext}} = \pm 300\,\text{V}$ and $E_{\text{ext,5V}} = 4.6\,\text{V/m}$ for $V_{\text{ext}} = \pm 5\,\text{V}$ (see field configurations in section 2.5.1).
The depth of the potential is the difference of the local maximum $U_{\text{eff}}(r_{\text{max}})$ and the local minimum $U_{\text{eff}}(r_{\text{min}})$ at the radii:

$$r_{\text{max}} = \sqrt{\frac{Q}{4\pi\epsilon_0 E_{\text{ext}}}}\ ,\ r_{\text{min}} = \frac{4\pi\epsilon_0 E_{\text{ext}} R^3}{Q} \tag{3.19}$$

The effective depth of the collective potential $U_{\text{eff}}(r)$ of the ions for molecular dynamics simulation are also shown in figure 3.6b with extraction fields $V_{\text{ext}} = \pm 300\,\text{V}$ (light red) and $V_{\text{ext}} = \pm 5\,\text{V}$ (red) as well as the the simulation in a field-free environment (dark red).
The progressing decrease of the depth of the trapping Coulomb potential in the cases with extraction field (light red and red) influences the duration of the expansion-driven cooling of the electrons: When the depth of the Coulomb potential becomes smaller than the kinetic energy of the electrons, they will escape the plasma and are accelerated by the extraction field towards the detector. This explains the sharp rise in the kinetic energy of the plasma electrons at $\approx 45\,\text{ns}$ (for $V_{\text{ext}} = \pm 300\,\text{V}$) and after $\approx 360\,\text{ns}$ (for $V_{\text{ext}} = \pm 5\,\text{V}$), yielding different final temperatures for the electrons. By tuning the extraction field, the lifetime of the plasma and the final temperature can be controlled. Without extraction field electrons will reach sub-meV energies in less than $1\,\mu\text{s}$.

### 3.3.3 Measurement of the plasma lifetimes

To determine the lifetime of the plasma experimentally, we employ a gated detection scheme as described in section 2.5.6. Here, after the time $T_{\text{pulse}}$ the voltage at the extraction mesh $V_{\text{ext}}$ is pulsed for $2\,\mu\text{s}$ to a repulsive voltage $V_{\text{rep}} = -V_{\text{ext}}$, pushing all

electrons arriving at the mesh after $T_{\text{pulse}}$ away from the MCP detector. The resulting signal shows the integrated counts up to $t = T_{\text{pulse}}$. In contrast to the improved timing reported in section 2.5.6, the measurements presented here are limited by a temporal resolution of $\approx 30\,\text{ns}$ due to the jitter of the old time base and the pulse rise times of the previously used high-voltage pulser.
Figure 3.7a shows the accumulated electron signals for pulse delays $T_{\text{pulse}}$ ranging from 0 ns to 1200 ns in steps of 200 ns at an extraction voltage $V_{\text{ext}} = \pm 5\,\text{V}$ measured at a peak pulse intensity of $I_0 = 1.2 \times 10^{13}\,\text{W/cm}^2$. All images are sum images over more than 10 realizations and are normalized to their individual peak value for better visibility. The image for $T_{\text{pulse}} = 0\,\text{ns}$ only shows a few electron counts from the background. The image at $T_{\text{pulse}} = 200\,\text{ns}$ shows a diffuse signal corresponding to electrons with an energy corresponding to the excess energy of the the two-photon ionization process. At $T_{\text{pulse}} = 400\,\text{ns}$ the first cold electrons escaping the plasma arrive at the detector and form the elongated signal discussed in figure 3.3g. This cold electron signal in the center of the image increases until it is saturated for $T_{\text{pulse}} > 800\,\text{ns}$. For longer pulse delays the overall brightness of the electron signal does not increase - all electrons from the plasma have been detected at this point.
Figure 3.7b shows the electron counts summed over the detector area in dependence on the arrival time for three different extraction voltages $V_{\text{ext}} = 5\,\text{V},\ 25\,\text{V}$ and $100\,\text{V}$. Here, the arrival time is the time when the voltage pulse is applied to the detector, the counts are the integrated counts up to $T_{\text{pulse}}$. For all three voltages the distribution shows two clear plateaus. The first corresponds to the escaping electrons leaving the ionization volume with a large kinetic energy. The second plateau can be associated to the plasma electrons being initially trapped in the plasma and leaving the ionic cloud as soon as the extraction field becomes dominant which takes up to a few hundred nanoseconds, depending on the strength of the extraction field.
The solid lines in the figure show the results of molecular dynamics simulations for the indicated extraction voltages. Each of them is scaled with a single free parameter to the maximum of the corresponding experimental result, showing excellent agreement for the arrival of the free electrons, the arrival of the plasma electrons as well as the ratio between them.
To extract the lifetimes of the plasma we fit a double-sigmoid to the experimental data:

$$f(t) = \frac{a_1}{1 + e^{-b_1 \cdot (t - c_1)}} + \frac{a_2}{1 + e^{-b_2 \cdot (t - c_2)}} \tag{3.20}$$

where $a_{1,2}$, $b_{1,2}$ and $c_{1,2}$ are fit parameters determining the amplitude, rise time and temporal position of the two sigmoids. Figure 3.7c shows the temporal derivative of the fitted sigmoids revealing the arrival time spectra of the electrons i.e. the detected counts per time. The position of the two peaks are given by the position of the edges of the sigmoids $c_1$ and $c_2$ in equation (3.20). The difference between the arrival time of the free and the plasma electrons $c_2 - c_1$ gives us the lifetime of the plasma and is plotted in the inset figure 3.7d. For the lowest extraction field ($V_{\text{ext}} = \pm 5\,\text{V}$), we obtain a maximum lifetime of 498(46) ns, while the highest extraction field that still allows for the gated detection scheme ($V_{\text{ext}} = \pm 100\,\text{V}$) yields a lifetime of 160(6) ns.

## 3.4 Conclusion

In this chapter we discuss the mechanism of ultrafast electron cooling in an ultracold microplasma created by local photoionization of a $^{87}$Rb BEC following the results presented in our publication [106].
We briefly describe the experimental conditions and explore the nature of the local photoionization within our BEC by explaining the methods we use to calculate the exact charge distribution after photoionization. We then define the necessary conditions leading to the formation of a plasma in the given system.
As a central tool for understanding the underlying dynamics of the plasma we introduce our method to perform molecular dynamics simulations with the charged particle tracing module of the COMSOL Multiphysics® [108] software. This method bears the advantage, that we can include a CAD model of our detector assembly with great precision to recreate not only the dynamics of the plasma, but also the measurement process yielding simulated detector signals in excellent agreement to our experimental data.
The experimental data presented shows an ultrafast electron cooling from 5250 K to below 10 K within the plasma lifetime of approximately 500 ns. The molecular dynamics simulations performed grant access to the underlying dynamics of the cooling process down to picosecond timescales.
We investigate the microscopic and macroscopic dynamics of the system and identify two cooling processes: The first rapid cooling takes place on the timescale of the inverse of the initial plasma frequency within the first 7 ps. Here, the plasma electrons loose about 50 % of their initial kinetic energy which is transferred into potential energy of the ions due to the initial charge separation triggered by the escaping electrons. This first ultrafast cooling yields an exceptional cooling rate of ≈400 K/ps. In the following nanoseconds the electrons are further cooled by the expansion of the ion cloud down to temperatures below 10 K. In an idealized model system without extraction field, this cooling driven by the expansion continues below this minimum temperature. At the end of the realized simulation time in the field-free simulation, we achieve an electron temperature of only $T_{\text{field-free}} = 292\,\text{mK}$, having bridged four orders of magnitude in temperature in only 2.5 µs .

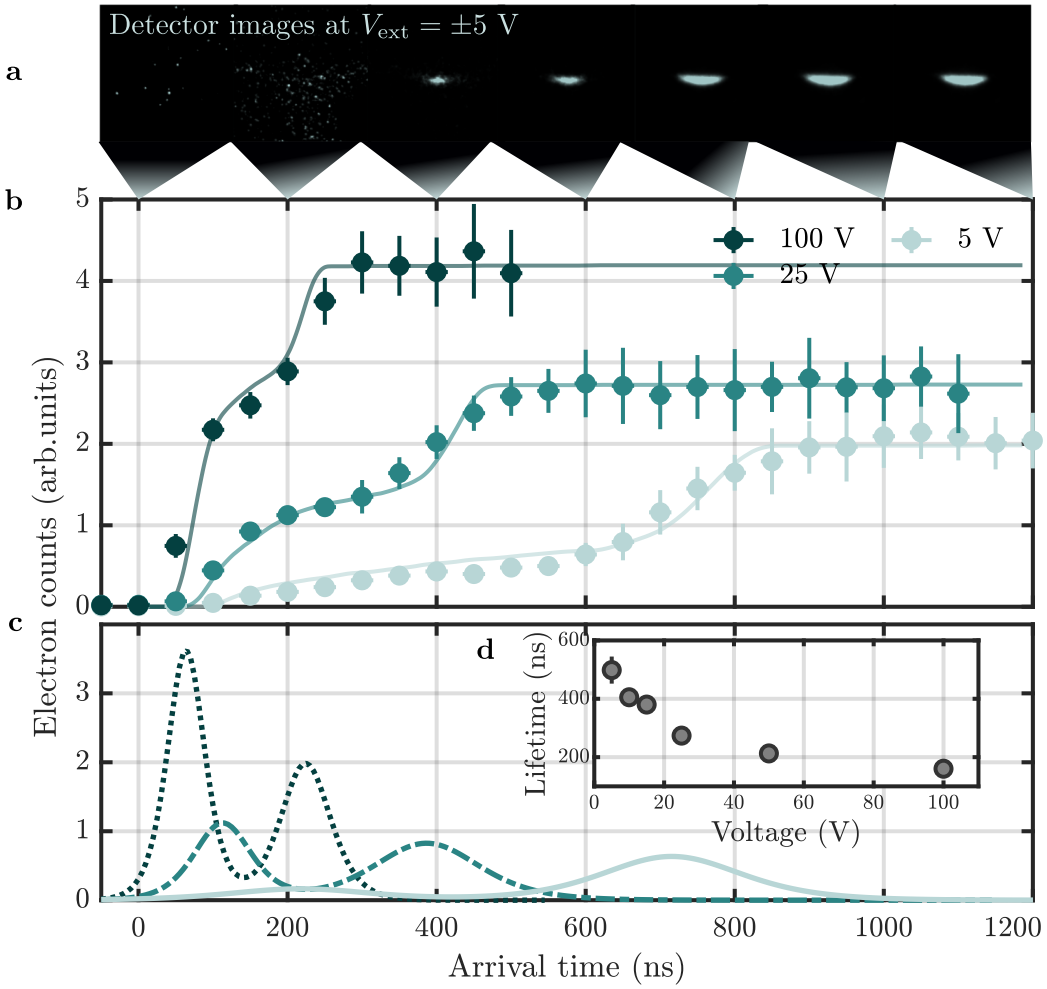


**Fig. 3.7: Measurements of the plasma lifetime.**
**a.** Exemplary detector images for voltage pulse delays $T_{\text{pulse}}$ from 0 ns to 1200 ns in steps of 200 ns for an extraction voltage of $V_{\text{ext}} = \pm 5$ V revealing the spatio-temporal evolution of the electron signal. The images are sum images over more than 10 realizations. The first image shows only background electrons. On the image for $T_{\text{pulse}} = 200$ ns the escaping electrons from the photoionization process are visible as a diffuse structure. For $T_{\text{pulse}} > 400$ ns a central feature associated with the cold electrons emerging from the plasma starts to appear and saturates after $T_{\text{pulse}} > 800$ ns. **b.** The data points and error bars mark the integrated electron counts with standard deviation (image sums over more than 10 realizations) measured at a peak intensity of $I_0 = 1.2 \times 10^{13}$ W/cm$^2$ in dependence on the arrival time (i.e. $T_{\text{pulse}}$) for three different extraction voltages: 5 V, 25 V and 100 V (light turquoise, turquoise, dark turquoise). The two plateaus with their corresponding edges are associated with the arrival of the escaping electrons and with a delay up to a few hundred nanoseconds the plasma electrons. The solid lines show the corresponding results of molecular dynamics simulations for the three voltages scaled with one free parameter to fit the experimental results. **c.** The experimental data in b is fitted with a double sigmoid as defined in equation (3.20) to extract the arrival times of both the free and plasma electrons. The derivative of these fits is plotted here in dashed lines for 5 V, 25 V and 100 V (light turquoise, turquoise, dark turquoise) revealing the arrival time spectrum of the electrons at the detector. **d.** The plasma lifetime ranging from 498(46) ns to 160(6) ns is plotted in dependence on the extraction voltage. It is given by the distance between the edges of the double sigmoid $c_1 - c_2$. Figure adapted from [106] and licensed under CC BY 4.0.

# 4 Across the threshold: Tuning the excess energy in an ultracold microplasma

In this chapter we discuss the experimental realization of plasma systems created by exciting either an ultracold thermal cloud or a BEC of $^{87}$Rb with femtosecond laser pulses close to the two-photon ionization threshold. The experimental results are complemented by molecular dynamics simulations to shed light on the underlying dynamics.
Section 4.1 motivates our interest in the plasma regime close to the two-photon ionization threshold followed by a presentation of the experimental parameters realized in the measurements in section 4.2.
In section 4.3 we thoroughly analyze the electron signals recorded during the measurements and introduce our methods of separating the electrons emerging from plasma dynamics, three-photon ionization and Rydberg excitation, while section 4.4 focuses on the ion signal as a measure for Coulomb energy.
We introduce our methods regarding the molecular dynamics simulations of the dynamics of the experimentally realized systems in section 4.5 that allow us to account for Rydberg states as well as ultracold plasma. Section 4.6 then applies these methods to the experimental conditions presented before, while section 4.7 summarizes the main results of both, the experimental and the simulative study.
The experimental results were recorded in close cooperation with Julian Fiedler with contributions by Jette Heyer. The simulations were performed and evaluated by the author and benefited from fruitful discussions with Julian Fiedler, Jette Heyer, Juliette Simonet, Philipp Wessels-Staarmann and Markus Drescher.

## 4.1 Tuning the excess energy of an ultracold plasma

In chapter 3 we discussed the generation and dynamics of a highly charged ultracold microplasma in detail. In the associated experiments we used femtosecond laser pulses at 511 nm which yield a high electron excess energy of 678 meV after two-photon ionization. By using the optical parametric amplifier available at our experiment, we are able to tune the wavelength of the femtosecond laser pulse. Consequently, this allows us to tune the excess energy of the electrons.
Figure 4.1a illustrates different plasma systems expected for varying excess energy. When using a pulse with a wavelength of 580 nm, the electrons have an excess energies of 98 meV, which exceeds the bandwidth of the laser pulse by a factor of 10. This leads to the dynamics described in the previous chapter with large electron orbits around the ion cloud, small orbits within the ion cloud and a large charge imbalance with rapid Coulomb expansion and electron cooling. Increasing the wavelength towards the ionization threshold at 593.7 nm will yield a more neutral plasma, where most of the electrons are confined to the ionic cloud.

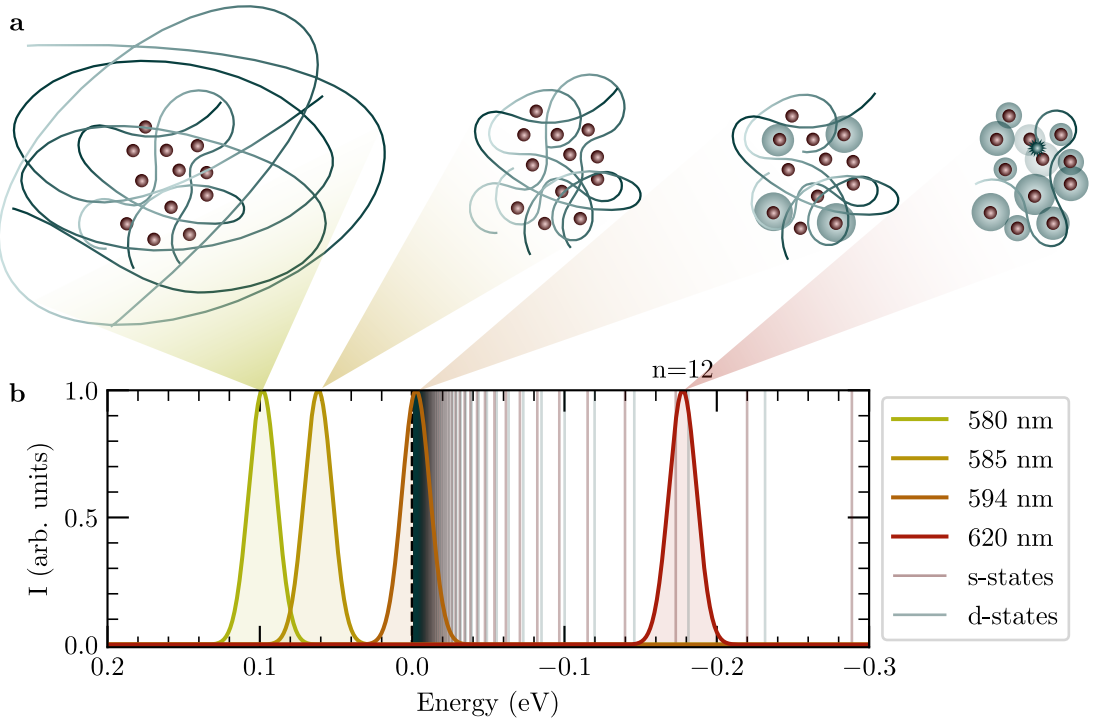


**Fig. 4.1: Tuning the excess energy across the ionization threshold.**
**a.** Illustrations of plasma systems above and below the ionization threshold. Photoelectrons with high excess energies will show a mixture of large orbits around the ion cloud and smaller orbits within the ion cloud and form a plasma with large charge imbalance. Approaching the ionization threshold, smaller electron orbits will dominate the dynamics while the charge imbalance is reduced and the plasma approaches neutrality. Directly at and below the threshold the large bandwidth of the femtosecond pulses will allow excitation of Rydberg states without Rydberg blockade, triggering Rydberg-Rydberg-ionization. **b.** To illustrate the accessible excess energies above the threshold and the addressable states below the threshold, the pulse profiles for the two-photon process at wavelengths ranging from 580 nm to 620 nm is plotted at a pulse duration of 170 fs. The vertical lines mark the ionization threshold (black dotted line), the s-states of $^{87}$Rb(dark red) and the d-states (turquoise) which can be addressed by two-photon-excitation.

On the one hand, crossing the two-photon ionization threshold, Rydberg excitation will play a significant role in the dynamics. The large radii of the Rydberg atoms and the high density of a BEC will lead to collisional Rydberg-Rydberg ionization and transfer of the electrons in bound states into ultracold plasma [74, 76, 114]. On the other hand, three-body Rydberg recombination can play a role for low excess energies above the threshold [75, 115].
Figure 4.1b shows the pulse profiles for two-photon ionization/excitation for wavelengths ranging from 580 nm to 620 nm at a pulse duration of 170 fs. The black dotted vertical line marks the two-photon ionization threshold at 593.7 nm, while the vertical red and turquoise lines mark the *s*- and *d*- states of an unperturbed $^{87}$Rb atom [116] which can be addressed by two-photon excitation. Due to the large bandwidth of the

femtosecond pulse, the Rydberg blockade effect as it is known (and employed) in experiments, where single Rydberg states are addressed with cavity-locked narrow-bandwidth laser systems, does not play a role here.
Directly at the threshold, we can assume that the excess energy is limited to the bandwidth of the two-photon process $2 \times \sigma_{\mathrm{E}} = 9.1\,\mathrm{meV}$ and yields the temperatures

$$T_{\mathrm{e}} = 77\,\mathrm{K}\ ,\ T_{\mathrm{i}} = 0.4\,\mathrm{mK}$$

which subceed the initial temperatures in the previous chapter by orders of magnitude, suggesting distinctively different initial conditions when creating a plasma at this wavelength.
To illustrate that the excess energy of the electrons can indeed be reduced in this manner, figure 4.2a shows false color electron detector images at an extraction voltage of 300 V averaged over 93 measurements per depicted wavelength. The target was a thermal cloud with a peak density of $\rho_{\mathrm{th}} = 2.8 \times 10^{17}\,\mathrm{m}^{-3}$.
To ensure that we detect only electrons created by two-photon ionization and neither plasma electrons nor electrons from three-photon ionization, the focus of the femtosecond laser pulse with a waist of $\mathrm{w}_0 = 1\,\mu\mathrm{m}$ was deliberately misaligned to effectively reduce the peak intensity of the pulse at the atomic cloud. Since, in this regime only a few atoms were ionized per pulse, 15 pulses were used in each experimental cycle to accumulate enough signal.
The depicted images correspond to wavelengths ranging from 513 nm to 593 nm covering excess energies from 657 meV to the bandwidth limit of 9.1 meV. The reduction in size and change in shape of the electron signal towards longer wavelengths is consistent with the reduction in kinetic energy of the electrons as discussed in section 2.5.2.
Tuning the electron excess energy towards the lower limit given by the pulse bandwidth leads to a reduction of the critical number of particles necessary for plasma formation and offers direct means of controlling the charge imbalance. Figure 4.2b shows the critical number $N^*$ (eq. (3.13)) plotted against the wavelength of the ionization pulse for the cylindrical ionization volume discussed in the previous chapter (sec. 3.2.1). The turquoise line marks the critical number for two-photon ionization which vanishes at the two-photon ionization threshold (dotted vertical line) where the excess energy approaches zero suggesting a neutral plasma in this regime. The dashed light turquoise line marks the critical particle number, assuming only three-photon ionization plays a role.

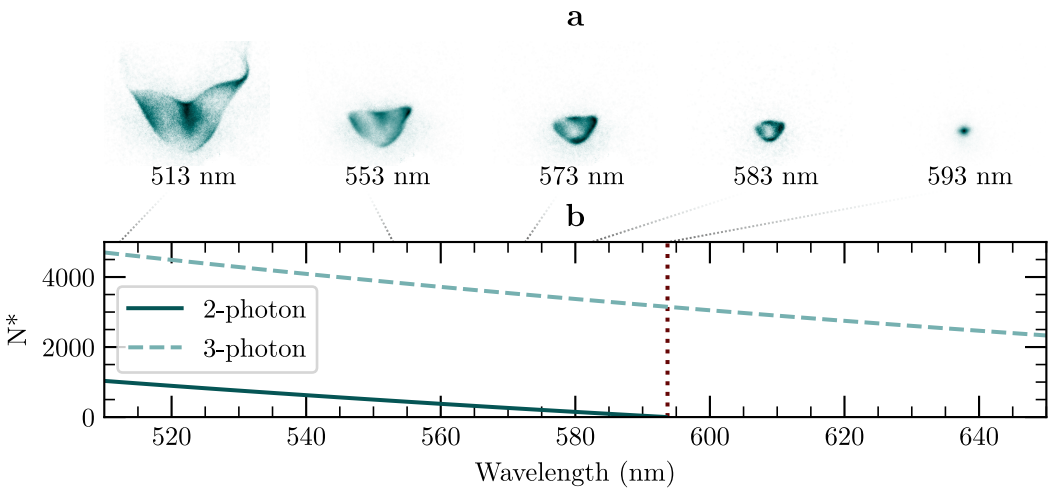


**Fig. 4.2: Excess energy and critical particle number for plasma formation.**
**a.** False color electron detector images averaged over 93 measurements with 15 femtosecond laser pulses per measurement. As target a thermal cloud with a peak density of $\rho_{\mathrm{th}} = 2.8 \times 10^{17}\,\mathrm{m}^{-3}$ was used and the focus of the femtosecond laser was shifted outside the atomic cloud to avoid high intensities at the target and the formation of a plasma. The images clearly show the decrease of the excess energy of the electrons created by two-photon-ionization as a shrinking of the structure on the detector when the wavelength of the pulse is tuned from 513 nm to 593 nm (compare to the simulated detector images in fig. 2.13). **b.** Critical number of ionization events $N^*$ necessary for plasma formation plotted against the wavelength of the ionizing pulse after eq. (3.13) for the approximated cylindrical ionization volume discussed in section 3.2.1. The turquoise line marks the critical number for two-photon-ionization and approaches zero at the two-photon-ionization threshold at 593.7 nm (dotted vertical line) while the dashed light turquoise line marks the critical particle number for three-photon-ionization.

## 4.2 Across the threshold: Experimental conditions

We choose 583 nm, yielding an excess energy of 76 meV as the first wavelength above the two-photon ionization threshold in our measurements. This ensures, that we start far from the case discussed in the previous chapter with an electron excess energy of 678 meV. The longest wavelength we used in our experiments was 643 nm. Here, the two-photon energy is 321 meV *below* the ionization threshold and close to the $n = 10s$ state of $^{87}$Rb at a binding energy of $-289$ meV and the two $n = 8d$ states at a binding energy of $-306$ meV, marking the lowest unperturbed states addressable by two-photon excitation.
The three-photon excess energy ranges from 2.202 eV at 583 nm to 1.608 eV at 643 nm. While the three-photon ionization processes play a significant role in the systems presented here, higher order processes could not be detected.
Especially below the threshold, where Rydberg-Rydberg ionization and electron-Rydberg ionization can be expected, the density of the atomic target will influence the unfolding dynamics. To this end we prepare two different targets by varying the final power of our exponential dipole trap evaporation. For a dilute target, we prepare an ultracold thermal cloud by stopping the evaporation in the crossed dipole trap at a final dipole trap

power of 0.5 W, yielding a Gaussian atomic density profile with $N_{\mathrm{th}} = 1.9(1)\times10^5$ atoms and a peak density of $\rho_{\mathrm{th}} = 2.8\times10^{17}\,\mathrm{m}^{-3}$ with an interparticle distance of $a_{\mathrm{th}} = 950\,\mathrm{nm}$ (eq. (3.4)). We also perform measurements on a BEC with $N_{\mathrm{BEC}} = 2.6(3)\times10^4$ atoms and a peak density of $\rho_{\mathrm{BEC}} = 1.6\times10^{20}\,\mathrm{m}^{-3}$, almost three orders of magnitude higher. Here, the interparticle distance amounts to $a_{\mathrm{BEC}} = 110\,\mathrm{nm}$.
Since the output power of the OPA shows a significant wavelength dependency and large shot-to-shot fluctuations, the pulse energy for each measurement was recorded as described in section 2.3.3. All data then was binned according to the recorded pulse energy, enabling us to post-select data to ensure comparable conditions. If not stated otherwise, all data recorded with a thermal cloud are taken at a pulse energy of 109(5) nJ corresponding to a peak intensity of $I_0 = 3.9(2)\times10^{13}\,\mathrm{W/cm^2}$, while data recorded with a BEC are taken at a lower pulse energy of 70(5) nJ corresponding to a peak intensity of $I_0 = 2.5(2)\times10^{13}\,\mathrm{W/cm^2}$ due to degradation in the output power of the OPA.
Regarding the detection of Rydberg atoms excited by the femtosecond laser pulse, we find that we can effectively ionize them with light from our dipole trap at 1064 nm. To this end, instead of applying the femtosecond excitation pulse after switching off all trapping potentials, we switch the tweezer axis of the dipole trap to its maximum power of $\approx 3\,\mathrm{W}$ for 10 µs. Depending on the binding energy of the Rydberg states addressed by the femtosecond pulse, this ionization yields excess energies close to the photon energy of the dipole trap of 1175 meV and below. The corresponding electron signal can be clearly separated from both, cold plasma electrons and electrons from three-photon ionization on the electron detector. A detailed discussion of the detection of Rydberg states follows in section 4.3.3.

## 4.3 Electron signal

All electron and ion signals are recorded with the field configuration discussed in section 2.5.1 at an extraction voltage of $V_{\mathrm{ext}} = 300\,\mathrm{V}$. We analyze the averaged images for each wavelength by identifying features belonging to three-photon ionization (excess energies from 1.6 eV to 2.2 eV), electrons originating from the optional Rydberg ionization pulse (excess energies from 0.8 eV to 1.2 eV) and plasma electrons (very small excess energies).
Electrons originating from three-photon ionization and plasma electrons can be separated by simply masking the central area of the detector image corresponding to the low excess energies and thus to the cold electrons emerging from the plasma dynamics. For wavelengths below the two-photon ionization threshold, the Rydberg signal can be extracted by subtracting the brightness (i.e. pixel counts) of the images without Rydberg ionization pulse from the brightness of the images with Rydberg ionization pulse. The former only show electrons from three-photon ionization and plasma, while the latter also features the electrons from single-photon ionization of bound states by the dipole trap pulse. The total brightness is given by the sum of the extracted signals for each class of electrons.
The incidence probability of electrons traveling through our detector setup shows an energy dependency (see fig. 2.14). To obtain a brightness signal for the different electron

classes that is indeed proportional to the number of created electrons, this incidence probability has to be taken into account. Therefore, we weight the detected brightness of each electron class with the inverse of the corresponding incidence probability. For the slow plasma electrons we assume an incidence probability of 100 % due to their low kinetic energies. For the Rydberg signal it is set to 75 % corresponding to the simulation results obtained for electrons of $\approx 1\,\mathrm{eV}$. For the electrons originating in three-photon ionization we approximate the incidence probability with 45 %, corresponding to an energy of $\approx 2\,\mathrm{eV}$ or a wavelength of 600 nm.
Figure 4.3 shows the detector brightness extracted in this manner from the detector images for a thermal cloud (a) and a BEC (b) plotted against the wavelength of the femtosecond excitation pulse. While the upper plot shows the absolute brightness, the lower plot shows the ratios of the components. The dotted vertical line marks the two-photon ionization threshold at 593.7 nm (gray) and the dashed lines mark the unperturbed $n = 12s, 11s, 10s$ states (red, left to right) as well as the unperturbed $n = 10d, 9d, 8d$ states (dark turquoise, left to right) for orientation [116].
The total brightness (black, shaded areas show the standard deviation) exhibits three distinct resonance features at around 615 nm, 628 nm and 638 nm for a thermal cloud. These resonances originate in the signal from the Rydberg ionization pulse (red) and fit to the marked positions of the $n = 10d, 9d, 8d$ states (and the $n = 12s$ state). The resonances around 628 nm and 638 nm are also visible in the measurement with a BEC, but are broader and far less pronounced here.

### 4.3.1 Three-photon ionization

In the performed measurements we observe a surprisingly high amount of electrons originating from three-photon ionization processes that we did not encounter in previous experiments at 511 nm. In fact, in the measurement with a BEC, most of the detected electrons originate from three-photon ionization (43 % to 83 %) (fig. 4.3b, dark turquoise). Both, ratio and total brightness are higher than in the measurement with a thermal cloud. This is an effect of the higher density of the BEC leading to significantly more atoms in the high intensity region of the small femtosecond laser focus.
In the measurement with a thermal cloud the amount of three-photon ionization events seems to be higher above and close to the threshold. However, here, the signal of the three-photon ionization is overestimated. This is due to the overlap between the signatures of electrons from two-photon ionization, plasma and three-photon ionization on the detector (see again figure 2.13a) making a clear separation of the energy classes impossible.
Exemplary, figure 4.4 shows averaged and normalized false color images of the electron signal for a BEC (a) and a thermal cloud (b) when a femtosecond laser pulse with a wavelength of 583 nm is used. The upper images show the masked image that we associate with electrons originating in three-photon ionization. The lower images show the masked area containing the slow plasma electrons. With a BEC as target, the shape of the signal corresponding to electrons originating in the three-photon ionization with an excess energy on the order of 2 eV is clearly visible. For a thermal cloud, this signal does not show a distinct shape. Here, it becomes evident that the separation by a simple

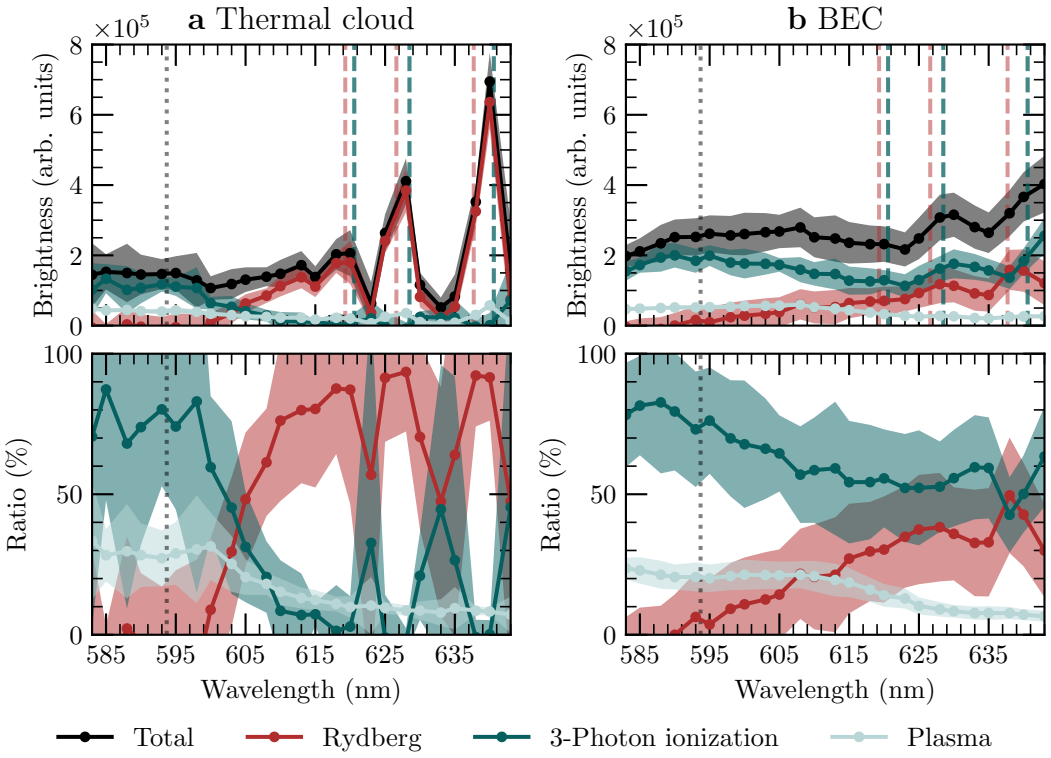


**Fig. 4.3: Brightness and ratio of different electron classes above and below threshold.**
Brightness of different electron classes in dependency on the wavelength after excitation of the target with a femtosecond laser pulse (upper plot) and ratio of the signals (lower plot). For the extraction of the plasma brightness (light turquoise) a small mask is applied to the detector images around the central area where electrons with low kinetic energies are detected and only the counts within this area are summed up (see figure 4.4). For the brightness of the electrons ionized via three-photon ionization (dark turquoise) all counts outside this mask are taken into account. The Rydberg signal (red) is extracted by switching on the dipole trap to a power of $\approx 3\,\mathrm{W}$ during the excitation pulse of the femtosecond laser to ionize the created Rydbergs via a single-photon process and the brightness of the image *without* this additional ionization pulse is subtracted. The total brightness (black) is the sum of all signals. The dotted gray line marks the theoretical position of the two-photon ionization threshold at 593.7 nm. The dashed lines mark the positions of the $n = 12s, 11s, 10s$ states (red, left to right) as well as the $n = 10d, 9d, 8d$ states (dark turquoise, left to right). The shaded areas mark the standard deviation of the corresponding brightness/ratio. **a.** The total brightness (black) of the electron signal when using a thermal cloud as target shows distinct resonance features near the marked states (dashed lines) originating in the signal associated with electrons from Rydberg states (red) (upper plot). Below the threshold most of the signal originates from these electrons (lower plot). **b.** Using a BEC as target, the resonance features are not as visible (upper plot). The ratio of Rydberg electrons is also much lower, while the electrons from three-photon ionization make up most of the signal (lower plot).

mask clearly overestimates the amount of electrons from three-photon ionization, since then faster plasma electrons are included.

In the naive picture of unperturbed states during the pulse, we would expect a significant increase in three-photon ionization below the two-photon ionization threshold because the three-photon ionization process, which is non-resonant *above* the threshold, would become a resonant two-photon process coupled with a non-resonant one photon process into the continuum *below* the threshold. In the measurement we do not observe this behavior. This again shows that strong-field ionization (and excitation) transcends the naive models and requires a full TDSE treatment that exceeds the scope of this thesis.

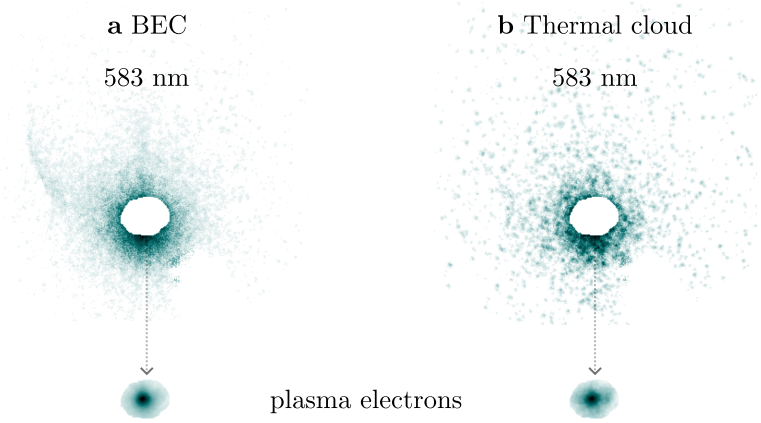


**Fig. 4.4: Separation of the electron signals from three-photon ionization and plasma dynamics.**
Averaged false color detector images at a femtosecond pulse wavelength of 583 nm to illustrate the separation of three-photon signal (top row) from plasma signal (bottom row) by using a simple mask in the center of the image. **a.** For a BEC the structure associated with three-photon ionization (compare to electrons with $E_k = 2\,\mathrm{eV}$ in fig 2.13a) is clearly visible. The masked area in the center contains the small feature corresponding to the cold plasma electrons. **b.** With a thermal cloud, the signal associated with three-photon ionization has no distinct structure. Here it becomes evident that part of the faster plasma electrons are counted as electrons originating in three-photon ionization, leading to an overestimation of this process.

### 4.3.2 Plasma above and below the two-photon ionization threshold

Besides the high three-photon ratio when using a BEC as target, the omnipresence of the plasma electron signature even for wavelengths far below the two-photon ionization threshold is noteworthy. In both cases, with BEC and thermal cloud, we detect slow plasma electrons at all wavelengths with a slightly higher absolute brightness when using the denser BEC as target (see figure 4.3b, light turquoise). The presence of these slow electrons across all wavelengths suggests that the cooling mechanism discussed in the previous chapter is remarkably robust.
Above the two-photon ionization threshold, detection of plasma electrons is expected, yet the underlying dynamics below the threshold have to differ profoundly.
A simple explanation for plasma formation below the threshold would be that the high

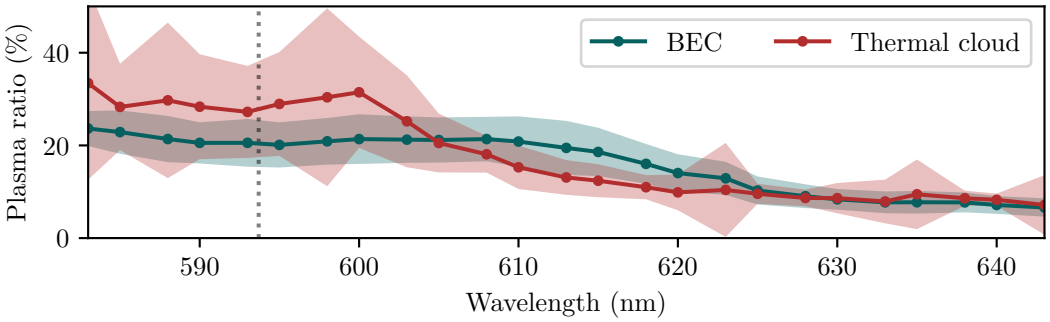


**Fig. 4.5: Plasma brightness ratio for thermal cloud and BEC.**
Plotted is the ratio of the plasma electrons taken from fig. 4.3 for a thermal cloud (red) and a BEC (dark turquoise), the shaded areas mark the standard deviation. With a thermal cloud, the plasma ratio remains almost constant up to a wavelength of 600 nm. Further below the two-photon ionization threshold the ratio of plasma electrons decreases. For the BEC, the plasma ratio remains almost constant, and the decrease occurs at significantly longer wavelengths. The difference below the threshold is either an effect of the higher ratio of electrons ionized via three-photon-ionization or the higher density yielding more Rydberg-Rydberg ionization for a BEC compared to a thermal cloud.

amount of electrons from three-photon ionization triggers plasma dynamics on itself. This would result in a sudden drop of the plasma signal at the threshold: Right above the threshold we would create a mixture of electrons with low kinetic energy from the two-photon process and electrons with high excess energy from the three-photon process. Right below the threshold we would create only electrons with high excess energy originating in three-photon ionization, which are much harder to trap by an ionic Coulomb potential. The critical particle number $N^*$ for plasma formation would jump at this point (see fig. 4.2) and we would expect an equal drop in the plasma brightness in our experiments, which we do not observe. Also, we only detect relatively few electrons from three-photon ionization below the threshold when using a thermal cloud as target, while there are still cold electrons present.
The origin of the plasma electrons below the threshold lies in the excitation of Rydberg states. Indeed, Rydberg states excited by the femtosecond laser pulse are ionized and form an ultracold plasma [74–76]. The ionization of the Rydberg atoms can occur via the overlap of the electron orbitals for atoms in Rydberg states, as well as via Rydberg-electron collisions, where the electron is either already freed by the former process, or originates in three-photon ionization. When Rydberg atoms are embedded into an ultracold plasma, the interaction between the plasma electrons and the Rydberg atoms can ionize even deeply bound states (n<20) [77].
Figure 4.5 again shows the plasma ratio extracted from figure 4.3 for BEC (dark turquoise) and thermal cloud (red) plotted against the wavelengths. In direct comparison, a few things become evident: Both plasma ratios have a plateau above the threshold and for the wavelengths close to the threshold. For the thermal target, the plasma ratio starts to decrease approximately at 600 nm, for the BEC the same decrease starts at a longer wavelength of approximately 615 nm. The decay of the plasma ratio for the thermal target clearly coincides with an increase in the ratio of ionized

Rydberg atoms (see again figure 4.3a). This also holds true for the corresponding absolute brightness. With a BEC the situation is similar, although the increase in the signal associated with the Rydberg states is not as steep. This suggests the transfer of electrons in Rydberg states into plasma electrons, which is amplified at the higher BEC densities leading to a plateau in the plasma ratio that reaches further below the threshold.

### 4.3.3 Ultrafast excitation of Rydberg states

#### Detection of atoms in Rydberg states

As stated above, we are able to detect atoms in Rydberg states by means of an ionization pulse from our dipole trap at 1064 nm wavelength that overlaps with the femtosecond excitation pulse. By subtracting the averaged image without ionization pulse from the image with the Rydberg ionization pulse, we can effectively isolate the electrons from the Rydberg ionization. Figure 4.6a illustrates this process. A femtosecond laser pulse with a wavelength of 625 nm is used to excite and ionize atoms in a thermal cloud and the averaged electron detector image is subtracted from an averaged image with an additional 10 µs ionization pulse from the dipole trap. While the former only contains plasma electrons and electrons originating in three-photon-ionization, the latter also contains electrons from ionization of Rydberg states. The difference image then only contains these electrons from Rydberg ionization and exhibits a clear structure concurring with simulated electron distributions of 0.7 eV to 1 eV. This is in agreement with the $n = 11s$ state or the $n = 9d$ state when ionized via one photon from the dipole trap, as indicated in the brightness spectra shown in figure 4.3a.

To ensure that the Rydberg ionization pulse from the dipole trap saturates the ionization of the atoms excited by the femtosecond laser pulse, the intensity of the dipole trap pulse used for the ionization is scanned. In order to realize short ionization pulses, the intensity control loop of the dipole trap has to be bypassed to allow for fast switching to a higher power in the tweezer axis of the dipole trap for 10 µs coinciding with the femtosecond laser pulse. Without the intensity control, the intensity during the pulse can not be precisely determined. The total available power was on the order of $\approx 3\,\mathrm{W}$ (yielding an intensity of $I_{\mathrm{DT}} \approx 7 \times 10^5\,\mathrm{W/cm^2}$). By changing the amplitude of the radio-frequency inserted into the acousto-optical modulator controlling the tweezer, the intensity can be tuned in a relative manner. In figure 4.6b the brightness of the signal with ionization pulse from the dipole trap (turquoise) and the Rydberg signal after subtraction of the signal without pulse from the dipole trap (red) is plotted against the relative intensity of the dipole trap pulse. The target was a thermal cloud and the femtosecond pulse was set to a wavelength of 628 nm, coinciding with the first resonance shown in figure 4.3. Although the cross section of the one-photon ionization process can not be extracted precisely, it is quite evident that we quickly saturate the transition when the intensity is increased.

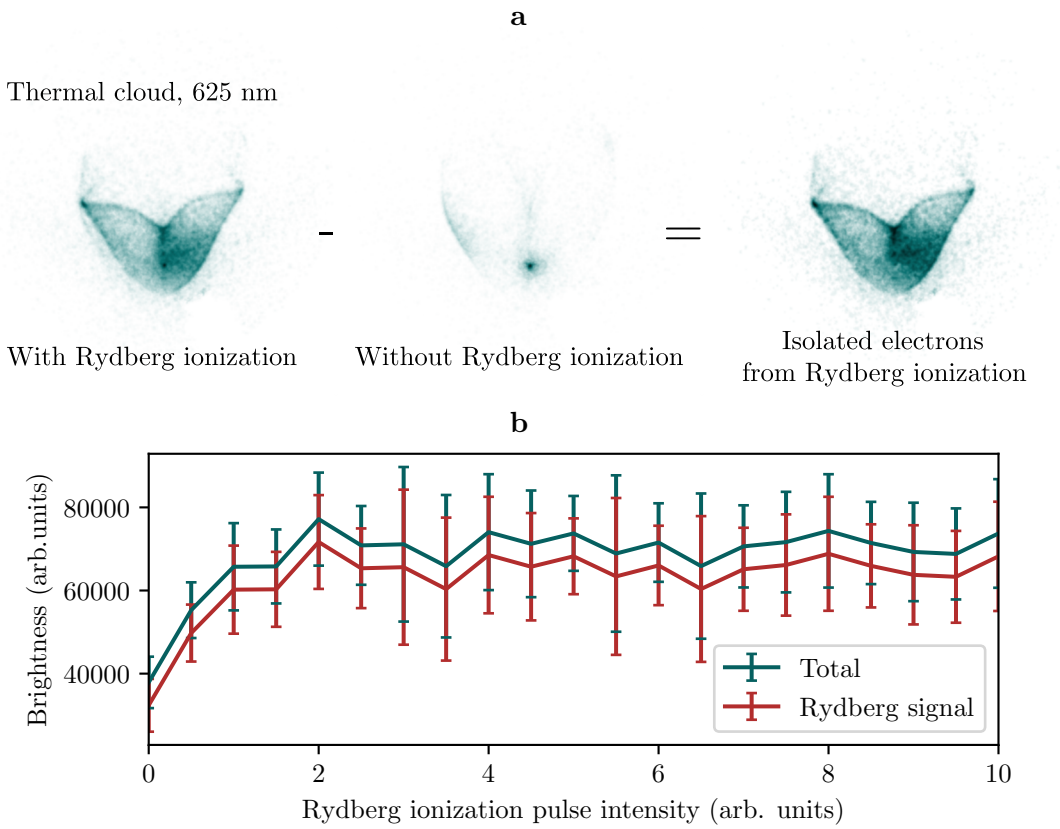


**Fig. 4.6: Extraction of the Rydberg signal.**
**a.** Rydberg atoms excited in a thermal cloud by a femtosecond laser pulse at a wavelength of 625 nm are ionized by applying light from the dipole trap. To isolate the detected electrons originating from this Rydberg ionization, we subtract the averaged images without the ionization pulse from the averaged images with the ionization pulse. Since the image without the ionization pulse contains only plasma electrons and electrons originating in three-photon-ionization, which are also present in the image with the ionization pulse, the resulting difference image contains only the electrons from the ionized Rydberg atoms. For the image without Rydberg ionization pulse 78 images were averaged, for the image with Rydberg ionization pulse 24 images were averaged. The structure in the difference image is in good agreement with the simulated detector images with excess energies between 0.7 eV to 1 eV. This suggests that the excited state could indeed be a $n = 11s$ or $n = 9d$ state (as marked in figure 4.3a). **b.** The total brightness recorded with the electron detector (dark green) and the brightness of the Rydberg signal (red) after extraction via the method illustrated in (a) is plotted against the relative intensity of the ionization pulse from the dipole trap. The error bars mark the standard deviation. The measurement was performed with a thermal cloud and the atoms were excited via a femtosecond pulse with a wavelength of 628 nm close to one of the resonance feature visible in the electron detector brightness spectrum. We use a 10 µs ionization pulse from the dipole trap with a wavelength of 1064 nm and a maximum intensity on the order of $\approx 3$ W. Since the intensity control loop of the setup has to be circumvented to create short pulses of high intensity, only the relative intensity can be estimated. However, we observe that the Rydberg ionization quickly saturates when the intensity is increased, suggesting that the applied intensity is sufficient to ionize all excited atoms.

### Excitation of different Rydberg states

The shape and size of the electrons from the ionization of the Rydberg states via the dipole trap pulse on the electron detector can give insight into the binding energy of the state(s) excited by the femtosecond laser pulse. Here, the excess energy $E_{\mathrm{e,Ryd}}$ of the detected electrons is given by:

$$E_{\mathrm{e,Ryd}} = E_{\gamma,\mathrm{DT}} + E_{\mathrm{b}} \tag{4.1}$$

where $E_{\gamma,\mathrm{DT}}$ is the photon energy of the dipole trap amounting to 1.17 eV and $E_{\mathrm{b}} < 0$ is the binding energy of the addressed bound state. A reduction in size of the detector signal can be associated with a decrease in excess energy or an increase in the magnitude of the binding energy and thus an addressing of lower lying bound states with the femtosecond laser pulse.
Although we can not measure the excess energy of the electrons in an absolute manner due to limited overlap between our simulated electron images with the experimental realizations and the small differences and finite resolution at the excess energies common to our Rydberg detection scheme, we can easily find a relative measure for the binding energy. To illustrate our approach, figure 4.7a shows the Rydberg electron detector signals after applying a femtosecond laser pulse with a wavelength of 603 nm (turquoise) and 628 nm (red) to a thermal cloud. To quantify the change of shape in the detector signal in a simple manner, we define a rectangular portion of the image as region-of-interest (dotted red rectangle). In this region, different excess energies lead to a vertical shift in the upper edge (dashed horizontal lines) of the wing-like structure.
We define this edge as the $y$-position where the summed up $y$-profiles shown in figure 4.7b (turquoise - 603 nm, red - 628 nm) in the rectuangular region-of-interest reaches 50 % of its maximum value (red and turquoise dotted vertical lines). To determine the robustness of this measure, we also determine the 30 % and 70 % mark and use them as lower and upper boundaries (shaded areas) for the position of the edge.
The position of the edge shows an almost monotonically falling dependency on the wavelength of the femtosecond laser pulse when a thermal cloud is used in the experiment (fig. 4.7c, red). This simply means, that the excess energy of the detected electrons decreases when the femtosecond laser pulse is tuned further below the threshold and indicates that we indeed address lower states with higher magnitude of the binding energy here.
At the aforementioned resonance feature around 628 nm, the extent of the electron structure shows a local minimum - at the wavelengths from 630.5 nm to 635.5 nm the signal again shows a larger extent and thus a larger electron excess energy. A larger binding energy at 628 nm in comparison to longer wavelengths would be implausible, we interpret this as an effect of the Coulomb interaction with the remaining ions. The peak in the total brightness on the detector at this wavelength (see again fig. 4.3a) indicates that at this point a lot of atoms in Rydberg states are ionized, leaving behind an equally large amount of positively charged ions. The large attractive Coulomb potential of this ensemble decelerates the escaping electrons and thus effectively reduces the measured excess energy (the same effect was observed on the two-photon signature for different intensities in the previous chapter in section 3.3.1).

When evaluating the Rydberg signals from the measurement with a BEC, very similar results are obtained for wavelengths >618 nm (fig. 4.7c, turquoise) than for a thermal cloud. For shorter wavelengths closer to the threshold, the size of the signal is significantly smaller. In addition, the uncertainty given by the 30 % to 70 % thresholds is much larger which implies a less pronounced edge of the signal. This can be clearly seen on the false color images of the isolated electrons originating in Rydberg ionization for 603 nm, 615.5 nm and 628 nm shown in figure 4.7d-f. While the signal at 628 nm (f) shows the same distinct features and shape as the signal extracted from the measurement with a thermal cloud in figure 4.7a (red), it appears heavily deformed and less distinct for 603 nm (d) and 615.5 nm (e). Looking back at the plasma ratio for wavelengths close to the threshold in figure 4.5, we observe that the deformations in the detected Rydberg signal for wavelength up to 618 nm coincide with the plateau in the plasma ratio. This again suggests that here the system shows a stronger transfer from electrons bound in Rydberg states into ultracold plasma due to the higher density of the BEC in contrast to the measurements with a thermal cloud.

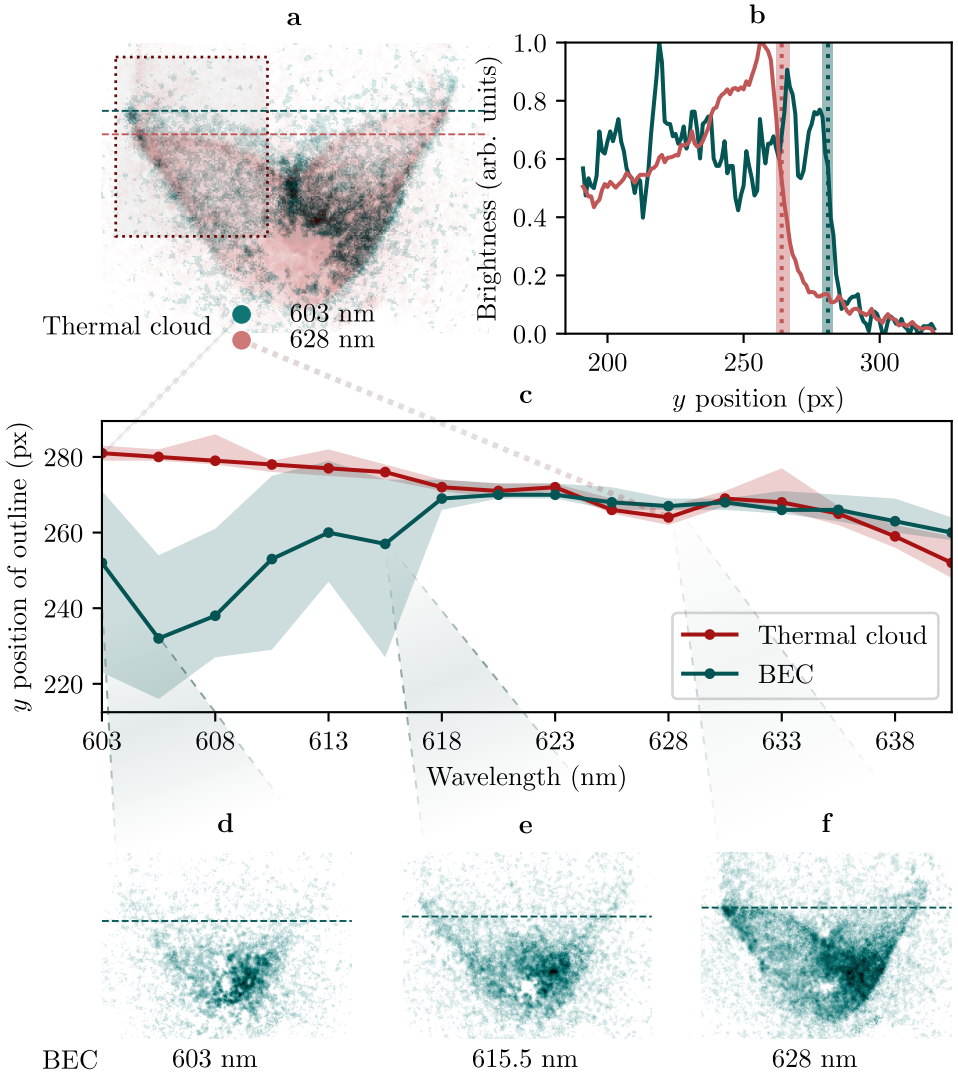


**Fig. 4.7: Qualitative analysis of the Rydberg electron signal.**
**a.** Isolated electrons from Rydberg ionization for 603 nm (turquoise) and 628 nm (red) for a thermal cloud. The dashed lines give the edges of the left wing of the visible structure extracted as described in (b) while the rectangle marks the region-of-interest for the extraction. **b.** To get a more quantitative measure associated with the excess energy and the binding energy of the Rydberg state, the size of the signal is quantified by the position of the edge in the left wing of the structure in (a). This was done only on the left side to circumvent the asymmetry in our detector signal and because the upper edge of the wings is most sensitive to the excess energy (see again figure 2.13). To extract the position the cutout marked as dotted rectangle in (a) was summed over the $x$-axis and the resulting $y$-profile (turquoise line for 603 nm and red line for 628 nm) is plotted against the $y$-axis of the image. As edge we define the position, where this signal reaches 50 % of its maximum value (dashed lines). The shaded areas mark the region between 30 % and 70 % of the maximum value to estimate the robustness. **c.** Position of the edge discussed in (a) and (b) plotted against the wavelengths of the femtosecond pulse for a thermal cloud (red) and a BEC (turquoise). The shaded area gives the aforementioned 30 % to 70 % position as a measure of robustness. **d-f.** Isolated electrons from Rydberg ionization for a BEC at a pulse wavelength of 603 nm, 615.5 nm and 628 nm. While the signal looks similar to the signal with a thermal cloud as target for 628 nm, it is heavily deformed for shorter wavelengths due to Rydberg ionization triggered by plasma dynamics.

## 4.4 Ion signal

While we clearly can separate different classes of electrons in the triggered dynamics by characterizing them by kinetic energies as shown above, we are also able to detect the created ions. In section 2.5.4 we discuss the abilities and limitations of our ion detector on the basis of simulative studies. One of the core features is the ability to give a relative measure for the Coulomb energy present in the system as discussed in figure 2.17, since the energy of the ions is not dominated by the excess energy of the ionization process but rather by Coulomb interactions.
Since the ion signal discussed here is taken at the same time as the electron signal, the field configuration of the detector as well as the properties of the atomic clouds and femtosecond laser pulses remain the same. For the time-resolved measurement, only the pulse energies change as indicated.

### 4.4.1 Coulomb expansion

A valid measure for the Coulomb energy is the size of the ion signal at the detector since it is a direct result of the Coulomb expansion of the cloud. Figure 4.8a-c illustrates our method of extraction from the recorded detector images. In (a) a false color image of a single experimental run with a BEC as target and a femtosecond laser pulse with a wavelength of 593 nm is shown. The low detection efficiency of the ion detector prevents resolution of the complete structure after a single experimental run and the image shows gaps and asymmetry. To obtain the complete structure we average over half of the available data set (in this case 55 images) and apply a median filter with a window size of $10 \times 10$ pixel to remove noise and graininess (b). To evaluate the robustness of the signal obtained in this manner, we repeat this step with random permutations of different sets of single images from the data set. The area of the signal is finally obtained by counting the pixels that have nonzero brightness in the filtered and averaged image (c).
In figure 4.8d the area of the ion signal is plotted against the wavelength of the femtosecond excitation pulse for both targets: thermal cloud (red) and BEC (turquoise) both, with Rydberg ionization pulse from the dipole trap (*DT on*, dark colors) and without (*DT off*, light colors). The shaded areas indicate the standard deviation when different random selections in the averaging of the images are used as discussed above. It is obvious that the Coulomb energy, and thus the area of the signal on the detector, is higher for a BEC due to the higher atomic density of the atomic cloud. In this case, there is also a clear correlation to the total electron brightness plotted in figure 4.3b, simply revealing that the Coulomb energy increases with an increasing number of charged particles. For a BEC, there are only minor differences between the measurements with ionization of Rydberg atoms (*DT on* ) and without (*DT off*), suggesting that the ions from Rydberg ionization do not significantly influence the total Coulomb expansion. For a thermal cloud, the difference between the measurements with and without Rydberg ionization shows a distinct increase for wavelengths larger than 605 nm, duplicating the resonance features visible in the electron brightness (fig. 4.3a). This suggests that here the ionization of the Rydberg atoms via the dipole trap leads to an amplification of the initial Coulomb expansion.

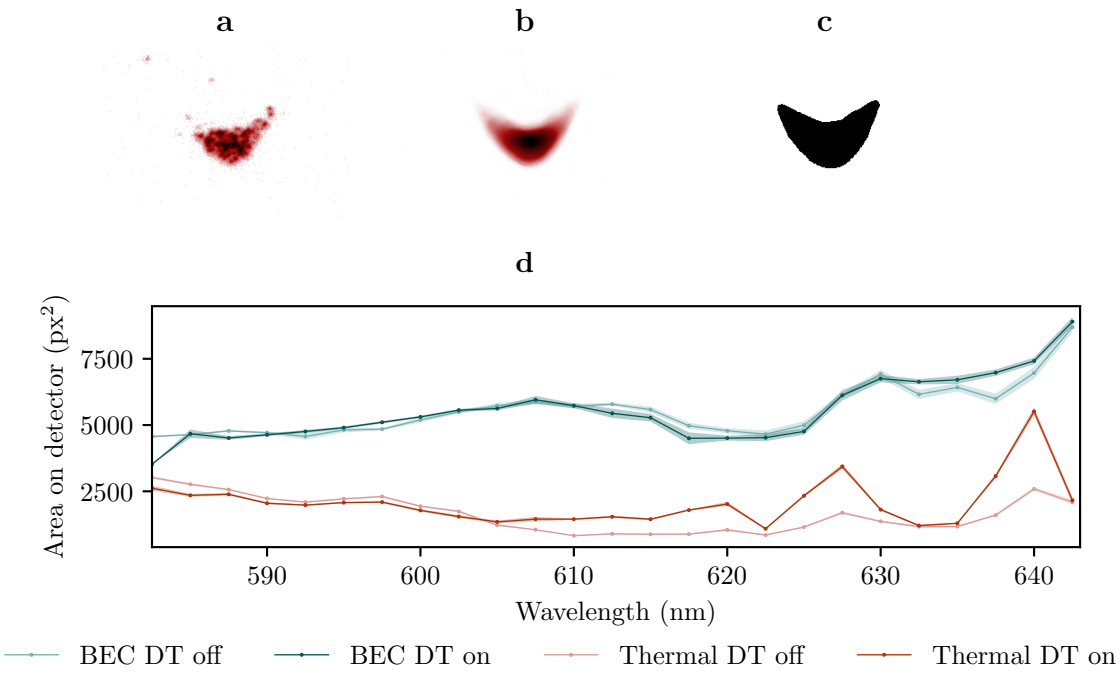


**Fig. 4.8: Evaluation of the area of the ion signal as a measure for Coulomb energy.** **a.** False color image from the ion detector at an excitation pulse wavelength of 593 nm applied to a BEC at an extraction voltage of $V_{\text{ext}} = \pm 300\,\text{V}$. **b.** Averaged image over half (here: 55) of all available images in the corresponding data set with an applied median filter with a window size of 10 px. Different permutations of averaged images give a measure of the robustness/deviation of the signal. **c.** The area of the signal is given by all pixels in (b) that have nonzero brightness. **d.** Plotted is the area of the ion signal on the detector against the wavelength of the applied femtosecond laser pulse for a BEC (turquoise) and a thermal cloud (red) with and without Rydberg ionization pulse (corresponding light and dark colors). The shaded areas mark the standard deviation of the area obtained using different permutations for the generation of the averaged image in (b). Following the previous discussion of our ion detector (see figure 2.17), we can read this area as a measure for the Coulomb energy in the system. For a BEC the Coulomb energy after excitation is much higher than with the thermal cloud due to the higher density. Here the signal, also shows a correlation with the total electron brightness in figure 4.3b. For the thermal cloud there is a clear indication that the Coulomb energy in the system is increased when the Rydberg states are ionized by the dipole trap pulse.

### 4.4.2 Signature of Rydberg atoms in the ion signal

A closer look on the ion detector images can give better insight into the influence of Rydberg atoms on the Coulomb expansion. Figure 4.9a shows an averaged and normalized false color image after excitation of a thermal cloud with a femtosecond pulse at a wavelength of 628 nm (chosen to be at the resonance feature in the electron brightness spectrum close to the unperturbed $n = 11s$ state or $n = 9d$ state). While the outline of the structure agrees with the simulated ion detector images in figure 2.17 for densities

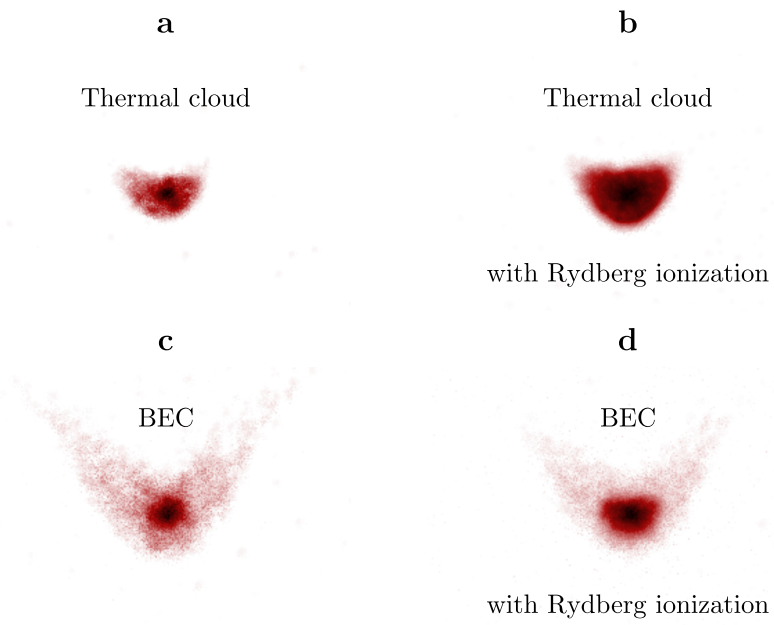


**Fig. 4.9: Signature of Rydberg atoms in the ion signal.**
**a.** Shown is the averaged and normalized false color ion signal after excitation of a thermal cloud with a femtosecond pulse at 628 nm. The overall shape agrees well to the simulated detector images for similar densities shown in figure 2.17. Yet, in the center of the structure a small spot is apparent. Not unlike the small central plasma feature in the images from our electron detector, this dot corresponds to slow ions that do not partake in the Coulomb expansion of the ion cloud. **b.** Using the same target and excitation parameters but adding the Rydberg ionization pulse from the dipole trap, the feature in the center of the structure vanishes and the area of the ion signal increases. The small spot can be attributed to Rydberg atoms that are ionized and do not take part in the initial Coulomb expansion. When ionizing the Rydberg atoms via the ionization pulse, they also take part in the Coulomb expansion and increase the Coulomb energy in the system. **c.** Using the same excitation wavelength and a BEC, the structure of the ion signal is much larger with more pronounced wings (in good agreement to our simulations for higher densities shown in figure 2.17). The small spot in the center associated with the Rydberg atoms that do not take part in the initial Coulomb expansion also has a better visibility. **d.** In contrast to the measurement with the thermal cloud, we observe the signature of a second Coulomb expansion when the Rydberg atoms are ionized by the dipole trap and the double structure is conserved.

in the order of $\rho \approx 5 \times 10^{-18}\,\mathrm{m}^{-3}$, there appears to be a small dark spot in the center of the structure. This narrow central feature can only be seen for wavelengths below the two-photon ionization threshold.
Not unlike the feature associated with the slow plasma electrons on the electron detector, this feature implies the detection of slow ions. In (b) a false color detector image with the same target and excitation parameters is shown, however, this time with Rydberg ionization pulse. The small central spot disappears under these circumstances and the total size of the signal increases. We assume that the small spot of slow ions in (a) is a signature of Rydberg atoms that are successively ionized in the course of the

plasma dynamics but do not take part in the Coulomb explosion of the free ions at the beginning of the dynamics. When a Rydberg ionization pulse is applied, these Rydberg atoms are ionized right after the femtosecond laser pulse and thus can take part in the initial Coulomb expansion increasing the Coulomb energy in the system and the area of the ion signal on the detector.
With a BEC, a similar yet slightly different behavior can be observed: Figure 4.9c shows the averaged and normalized false color image for the same wavelength of 628 nm of the excitation pulse. The outline of the main structure is much larger than in the case with a thermal cloud as atomic target, agreeing with our expectation that a higher density yields a higher Coulomb energy. Again, we see a small central spot in the center of the structure (only visible for pulse wavelengths below the two-photon ionization threshold).
When we apply the Rydberg ionization pulse from the dipole trap, instead of amplifying the initial Coulomb expansion like in the case where a thermal cloud was used, the ions from the Rydberg ionization form a separate Coulomb expansion visible as a second feature in the center of the main structure (d). Again, we attribute this behavior to the higher density of the BEC: The initial Coulomb expansion after the femtosecond laser pulse happens on much shorter timescales than in the case with a thermal cloud due to larger Coulomb energy in the system. The Rydberg ionization pulse needs a finite amount of time to ionize the remaining Rydberg atoms, which then are located as a dense cluster in the center of an already expanded dilute ion cloud, seeing the Coulomb repulsion of each other but barely that of the initial ion distribution. Thus they take part in a separate Coulomb expansion. In the thermal case, the timescale of the Rydberg ionization and the Coulomb expansion of the much more dilute sample overlap and the ionized Rydbergs can directly take part in the initial expansion dynamics. With a BEC as target, a double structure in the ion signal is preserved.

### 4.4.3 Time-resolved ion signal

To further strengthen that the small feature in the center of the ion signal at wavelengths below the two-photon ionization threshold can be associated with initially almost static Rydberg atoms, we perform a time-resolved measurement of the ion signal as explained in figure 2.19. We use an exposure time of 1 µs and shift the exposure time in steps of 1 µs to obtain a time-resolved tomography of the ion signal.
In figure 4.10a the normalized and averaged detector images are plotted against the start the camera exposure time $t$ in respect to the incidence of the femtosecond laser pulse for a thermal cloud and a wavelength of 628 nm. The wavelength was again chosen to be at the resonance feature observed in the electron brightness close to the unperturbed $n = 11s$ state or $n = 9d$ state. Since this was a different measurement than the extensive study concerning the scan of the pulse wavelength discussed above, the pulse energy here was different with $E_\mathrm{P} = 79(4)\,\mathrm{nJ}$ yielding a peak intensity of $I_0 = 2.8(1) \times 10^{13}\,\mathrm{W/cm^2}$.
The first counts of the ion signal appear at the detector approximately 13 µs after the femtosecond pulse and the total signal stretches to 33 µs. The first ions arriving at the detector are ions that get accelerated towards the detector by the Coulomb expansion, while ions that arrive at the end of the time span are ions that are initially driven into

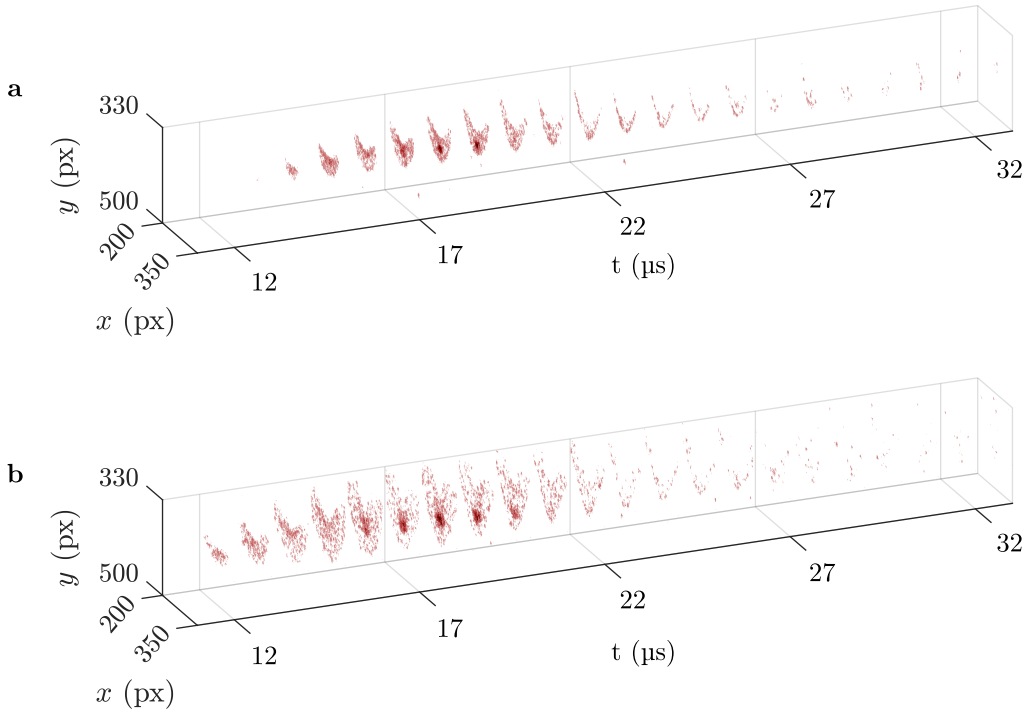


**Fig. 4.10: Time-resolved ion signal and Rydberg signature.**
**a.** The figure shows the time-resolved ion signal captured with the frame delay method discussed in section 2.5.5. Here, an excitation pulse with a wavelength of 628 nm with a mean pulse energy of 79(4) nJ was applied to a thermal cloud. The exposure time of the high speed camera was set to 1 µs and sets the time resolution of the measurement. The first ions arrive at the detector 13 µs after the femtosecond pulse, while the last arrive at approximately 33 µs. The first ions that arrive at the detector are ions that are accelerated by the Coulomb expansion towards the detector, while late ions are ions that get accelerated away from the detector and thus have significantly longer trajectories through the setup. Around 18 µs to 19 µs, ions forced radially to the detector axis arrive at the MCP. The arrival times measured here are in good agreement to the simulated arrival times for low densities in figure 2.18. The dot of slow ions apparent in the structure of the integrated ion signal shown in figure 4.9 arrives with the radially expanding ions at 17 µs to 19 µs, leading to the conclusion, that these ions are indeed ionized Rydberg atoms that do not partake in the initial Coulomb expansion and thus have vanishing axial velocity. **b.** A similar measurement was performed with a BEC as target and a pulse energy of 102(4) nJ at 628 nm. Due to the higher target density, the Coulomb energy in the system is increased and the ions experience more acceleration during the expansion. Therefore, the first ions arrive earlier at the detector, starting at 12 µs. The small feature associated with the Rydberg atoms still arrives between 17 µs to 19 µs, since their arrival time on the detector is not influenced by the Coulomb energy but is determined only by the extraction field.

the opposite direction by the Coulomb expansion.
Around 17 µs to 19 µs ions that move almost perpendicular to the detector axis can be detected, making up for most of the wing-like structure on the detector. The ions arriving at this time had low initial axial velocity. Ions that appear at the outlines of the visible structure have a high radial velocity.

The spot in the center of the structure then has neither high axial, nor high radial velocity and thus belongs to ions that are initially almost static. Since the spot only appears for wavelengths below the two-photon ionization threshold, we associated it to Rydberg atoms that are ionized in the course of the plasma dynamics but do not take part in the initial Coulomb expansion. The same holds true for the measurement with a BEC as is illustrated in figure 4.10b. Here, an excitation pulse with the same wavelength of 628 nm was used with a pulse energy of 102(4) nJ yielding a peak intensity of $I_0 = 3.7(2) \times 10^{13}\,\mathrm{W/cm^2}$.
The timescales differ slightly from the measurement with a thermal cloud: Here, the first ions already arrive 12 µs after the femtosecond pulse due to higher initial Coulomb energy and a faster Coulomb expansion. Again, the last ions arrive after 33 µs resulting in a signal that is more stretched out in time.
Still, the central spot we associate with the Rydberg atoms is located around 17 µs to 19 µs, supporting that the detected ions are initially static and do not take part in the Coulomb expansion. Hence, their time of arrival is solely defined by the extraction field and not their initial Coulomb energy.

## 4.5 Understanding the underlying dynamics - Molecular dynamics simulations for plasma near the ionization threshold

To get a glimpse of the underlying dynamics of the many-body systems created in our experiment, we again employ molecular dynamics simulations. For the results presented in chapter 3 we relied on the COMSOL Multiphysics® [108] software for both, molecular dynamics simulations and propagation through the electric field configuration of our detector. For the microplasma with large charge imbalance and high initial electron excess energies, this proved successful. However, closer to the two-photon ionization threshold the intransparent dynamic time stepping of the COMSOL becomes a problem for our endeavours. To get consistent, reliable and controlled results we switched to the "SARKAS - Python MD code for plasma physics" [117] for our simulations. This Python package provides a molecular dynamics toolbox that is both, fast and easy to manipulate, and offers a selection of different model potentials, boundary conditions as well as integrators.

### 4.5.1 Velocity Verlet integration

All the simulations we present in this chapter use the velocity Verlet integrator. This common integrator is often used in molecular dynamics simulations and has been developed in the 1980s [118]. Here, the iteration of the particle position $\mathbf{x}$ and velocity $\mathbf{v}$ from time $t$ to $t + \Delta t$ takes the simple form:

$$\mathbf{x}(t + \Delta t) = \mathbf{x}(t) + \mathbf{v}(t)\Delta t + \frac{1}{2}\mathbf{a}(t)\Delta t^2 \text{ and} \tag{4.2}$$

$$\mathbf{v}(t + \Delta t) = \mathbf{v}(t) + \frac{1}{2} \cdot (\mathbf{a}(t) + \mathbf{a}(t + \Delta t))\Delta t \tag{4.3}$$

Where $\mathbf{a}$ is the acceleration that in molecular dynamics simulations is usually derived from the interactions between the particles. In the SARKAS code the velocity Verlet integrator is implemented via the following steps:

- Calculate $\mathbf{v}(t + \frac{1}{2}\Delta t) = \mathbf{v}(t) + \frac{1}{2}\mathbf{a}(t)\Delta t$
- Calculate $\mathbf{x}(t + \Delta t) = \mathbf{x}(t) + \mathbf{v}(t + \frac{1}{2}\Delta t) \cdot \Delta t = \mathbf{x}(t) + \mathbf{v}(t)\Delta t + \frac{1}{2}\mathbf{a}(t)\Delta t^2$
- Apply boundary conditions and calculate accelerations $\mathbf{a}(t + \Delta t)$ from particle interactions using the new particle positions at $\mathbf{x}(t + \Delta t)$, assuming these are not dependent on $\mathbf{v}(t + \Delta t)$.
- Calculate the second half of the velocity iteration: $\mathbf{v}(t+\Delta t) = \mathbf{v}(t+\frac{1}{2}\Delta t)+\frac{1}{2}\mathbf{a}(t+\Delta t)\Delta t$ and return to the first step.

The local truncation error after a single iteration of the velocity Verlet algorithm is $\mathcal{O}(\Delta t^4)$ while the global truncation error can be estimated to $\mathcal{O}(\Delta t^2)$. Since our simulations only include Coulomb interactions and form a conservative system, a good consistency check is total energy conservation. Errors on position then translate into errors in potential energy, while errors in velocity translate into errors in kinetic energy.

### 4.5.2 Simulation parameters and particle distributions

Since we neglect interactions between charged particles and neutral atoms, we can restrict the model to Coulomb interaction between the charged particles and use the same expression for the Coulomb force with a short range cutoff $R_0$ as shown in equation (3.14) of the previous chapter.
A common simulative approach to investigate the internal dynamics of plasma systems is to restrict the simulation volume to a small box with periodic boundary conditions [119]. However, from our experiment and the experiences we obtained simulating the highly charged plasma in the previous chapter, we expect significant effects from the expansion dynamics and the finite size of our system. The small particle number of a few thousand electrons and ions makes it possible and necessary to simulate the whole distribution in an empty space with open boundary conditions.
The initial particle distribution in our simulations was generated based on the ionization model described in section 3.2.1 either applied to the Thomas-Fermi density distribution of a BEC or the Gaussian density distribution of an ultracold thermal cloud. The cross sections for the multi-photon ionization processes for all wavelengths covered in the measurement above are not known. Results from our previous publication covering experimental confirmation as well as TDSE-calculations are restricted to the ionization cross sections at wavelengths of 511 nm and 1022 nm [33]. We use the two-photon cross sections for wavelengths between 423 nm to 594.4 nm measured on ultracold Rubidium in a MOT setup reported in [31], neglecting three-photon ionization in the cross sections used in our approximations for the density of charged particles.
For the simulations presented in this chapter, we use two ion distributions:
The first distribution corresponds to a BEC, with $2.5 \times 10^4$ atoms in a crossed dipole trap with the trap frequencies $\omega_{x,y} = 2\pi \times 113\,\mathrm{Hz}$ and $\omega_z = 2\pi \times 128\,\mathrm{Hz}$ yielding a peak density of $\rho_{\mathrm{BEC}} = 1.6 \times 10^{20}\,\mathrm{m}^{-3}$. The laser pulse is set to a pulse duration of 166 fs

at 590 nm with a focus size of $w_0 = 1\,\mu\text{m}$ and a pulse energy of 60 nJ corresponding to a peak intensity of $I_0 = 2.2 \times 10^{13}\,\text{W/cm}^2$. These parameters are close to the experimental parameters discussed in section 4.2 and with them we predict the ionization of 4193 atoms in a cylindrical section of the BEC. The distribution is very similar to the cylindrical volume we used in the simulations for the highly charged plasma in the previous chapter (see figure 3.2). This time, we do not approximate the distribution with a homogeneously filled cylinder but take the atomic density profile into full account.
The second distribution is based on the spherically symmetric Gaussian density profile of a thermal cloud with a width of $\sigma_r = 35.2\,\mu\text{m}$, $1.9 \cdot 10^5$ atoms and a peak density of $\rho_{\text{th}} = 2.7 \times 10^{17}\,\text{m}^{-3}$. The same pulse duration of 166 fs characteristic to our optical parametric amplifier setup is used and the wavelengths is set to 590 nm. The pulse energy is chosen to by higher at 350 nJ, yielding a peak intensity of $I_0 = 1.2 \times 10^{14}\,\text{W/cm}^2$ at identical focus size as above. The pulse energy was chosen to be significantly higher than with a BEC to get an ion number of a similar magnitude. The distribution of the 1112 ions predicted by this configuration has an hour-glass shape of approximately 120 µm length and a diameter of approximately 12 µm at the widest point (see B.1).

### 4.5.3 A classical model for bound atomic states

It quickly becomes evident that low electron energies and high densities require to take bound states in the simulations into account. Let us consider the two particle distributions mentioned above:
If we generate both, electrons and ions, randomly and separately from the charge distribution given by equation (3.6), we find that the mean Coulomb energy between each electron and its nearest ion amounts to

$$E_{\text{C,th}} = -1.4(10)\,\text{meV}\ ,\ E_{\text{C,BEC}} = -15(9)\,\text{meV} \tag{4.4}$$

For high electron excess energies this energy can be neglected, for lower excess energies it becomes relevant. At a femtosecond laser wavelength of 593.7 nm - the two-photon ionization threshold - the excess energy of the electrons is limited by the bandwidth of the laser pulse to $2 \times \sigma_E = 9.1\,\text{meV}$. Here, the mean nearest-neighbor Coulomb energy in the distribution associated with the BEC $E_{\text{C,BEC}}$ superceeds the excess energy of the electrons. Employing both, random electron and ion distributions we would create electrons that are bound to the nearest ion here, instead of electrons with the correct excess energy.
This problem can be circumvented by creating ions and electrons pairwise and taking into account the simple orbital model for bound states emerging from the Coulomb interaction illustrated in figure 4.11a-c. When we place a slow electron close to an ion, the potential energy becomes dominant. To counteract this, we place the electrons on closed circular orbits around the ions (figure 4.11a). For this, we simply set the centrifugal force $F_{\text{cf}}$ equal to the Coulomb force $F_{\text{C}}$ and calculate the initial velocity

$v_{e,0}$ for an electron on a circular orbit with distance $r$ to the ion:

$$F_{\mathrm{C}} = F_{\mathrm{cf}} \Leftrightarrow \frac{e^2}{4\pi\epsilon_0 r^2} = \frac{m_e v_{e,0}^2}{r} \Rightarrow v_{e,0} = \sqrt{\frac{e^2}{4\pi\epsilon_0 m_e r}} \tag{4.5}$$

where $e$ is the elementary charge, $m_e$ the electron mass and $\epsilon_0$ the vacuum permittivity. To avoid a total angular momentum in the system, we choose a random direction of the orbit for each electron-ion pair. For the simulations at BEC density, we set the initial radius to $r_{8s} = 3.8\,\mathrm{nm}$ the maximum of the radial part of the wave function of an $n = 8s$ state atom (calculated with the Alkali-Rydberg-Calculator library [116]). In the classical model this bound state has a binding energy of $-0.38\,\mathrm{eV}$, which is well below the reach of the lowest simulated femtosecond laser pulse wavelength of 638 nm. Here, the two-photon energy lies 0.29 eV below the ionization threshold.
Starting from these initial bound states, we implement the excitation or ionization process triggered by the femtosecond laser pulse by increasing the velocity of the electron by $\Delta v$ and thus adding to the kinetic energy of the bound electron. If the kinetic energy remains smaller than the potential energy in the electron-ion-system, the electron remains in a bound state (figure 4.11b) and moves to an elliptical orbit. If the kinetic energy of the electron is larger than the potential energy, the bound state gets ionized and the electron becomes a free electron (see figure 4.11c).
Using this approach we can effectively set an ionization threshold and a correct zero point for the kinetic and potential energies in dense Coulomb systems. It also allows us to incorporate free electrons from ionization as well as bound electrons with variable binding energies for wavelengths below the two-photon ionization threshold.
As a proof of principle, figure 4.11d shows the orbital radius $d$ normalized to the initial radius $d_0$ in dependency on the time of a single electron-ion system simulated in this manner. The initial radius was set to $r_{11s} = 10.5\,\mathrm{nm}$ which corresponds to the maximum of the radial part of the $s$-state wave function with principal quantum number $n = 11$. Although there is a minor ellipticity of the orbit leading to a deviation from the initial radius of up to $\pm 0.75\,\%$ due to numerical errors of the integrator, the total energy is conserved and the state can be considered as stable (even for times $\gg 5\,\mathrm{ps}$).
Although we model the bound states classically, we use discrete energy levels for the wavelengths below the two-photon ionization threshold, while we use continuous energies for the ionization events above the threshold. We also take the three-photon process into account. Since the ionization cross sections for the three-photon processes at all simulated wavelengths are not known, we use the ratios we observed in our measurement (figure 4.3b). Figure 4.12 shows the probability spectrum of the generated electron energies at a wavelength of 594 nm. The probability here is normalized to its maximum value for visual purposes. The peak around zero energy is the two-photon process with a bandwidth of 9.1 meV. The peak above 2 eV is the three-photon process with a bandwidth of 13.7 meV. We use significant simplifications here: above the threshold the spectrum is continuous and proportional to the Gaussian intensity profile of the pulse. Below the threshold the spectrum is discrete, using the energies of the unperturbed $s$- and $d$-states (both accessible via two-photon excitation) of a $^{87}$Rb atom [116]. The inset figure shows a zoom into the two-photon peak. The probability here is also proportional to the Gaussian intensity profile - we do not take the exact

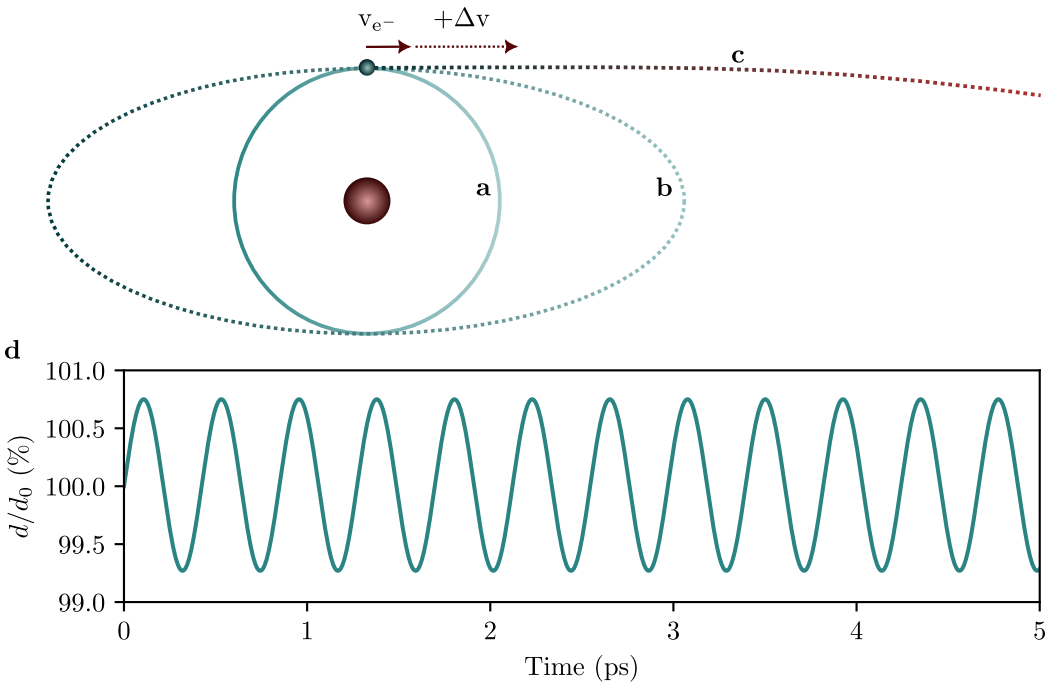


**Fig. 4.11: Classical model for bound states emerging from the Coulomb interaction.** **a.** Circular orbit of a bound state we use as initial condition for each electron-ion pair to avoid miscalculation of the initial potential energy when the charged particle distributions are generated randomly at high densities. The radius is set to the maximum of the radial s-wave function for principal quantum number $n = 8$. **b.** By increasing the velocity of the electron and thus the kinetic energy the electrons follow elliptical orbits with binding energy of lower magnitude. In our simple representation this would be the case when the wavelength of the femtosecond excitation pulse is below the two-photon ionization threshold. **c.** When the energy of the electron exceeds the magnitude of the binding energy between electron and ion, the bound state gets ionized and the electron moves to a free trajectory leaving the system. **d.** As a proof of principle we simulate a single bound state consisting of an ion and an electron where the electrons initial distance was set to the maximum of the radial s-wave-function for $n = 11$, yielding a distance of $r = 10.5\,\mathrm{nm}$. The simulation shows only a minor ellipticity with a deviation from the initial orbit of only $\pm 0.75\,\%$ due to the integrator, while the energy is conserved and the bound state remains stable.

excitation probabilities into account, since their calculation is not trivial for strong-field excitation.

In the earlier publication regarding the strong-field ionization cross sections [33], a complete treatment of the time-dependent Schrödinger equation with the atom in the time-dependent electric field of the femtosecond laser pulse was necessary. This treatment is not in the scope of this thesis but would yield valuable insight into the ionization and excitation mechanics in the strong-field regime.

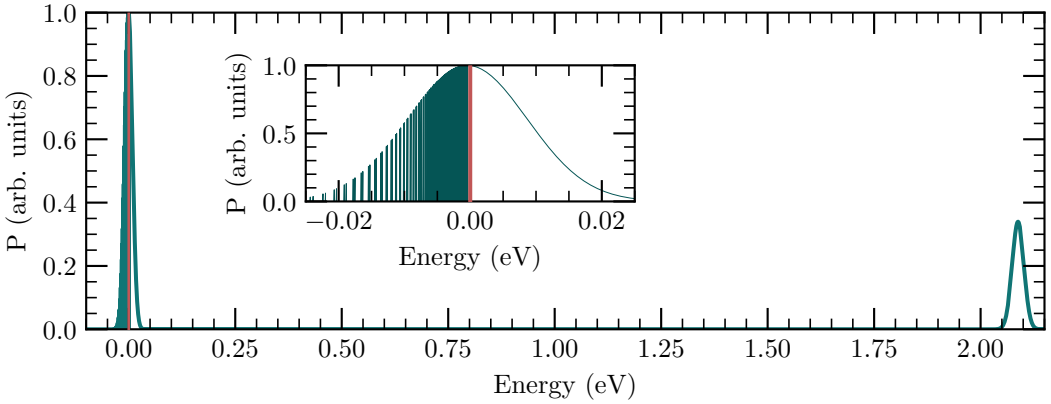


**Fig. 4.12: Exemplary probability spectrum of the generated electron energies.** Plotted is the probability to generate an electron at a given energy in our simulations normalized to its maximum value. The first peak marks the two-photon process with a bandwidth of 9.1 meV at wavelength of 594 nm. Half of the peak is above the threshold and has a continuous probability spectrum, while the other half is below the threshold. Here we choose the energies according to the energies of the unperturbed $s$- and $d$-states of $^{87}$Rb. The inset shows a zoom into the spectrum at the threshold. The probability in our simplified model is always proportional to the intensity since the exact excitation probabilities for different states are unknown in the strong-field regime. The peak above 2 eV marks the three-photon process with a bandwidth of 13.7 meV. The ratio between two-photon and three-photon process for each wavelength is taken from the measurement of the electron signal in figure 4.3.

### 4.5.4 Model case: Thermal Rydberg clouds

Before we present the calculations at BEC densities revealing the underlying dynamics of the experimental results, we consider a model case with pure samples of single Rydberg states at the density of a thermal cloud. As ion distribution we use the hour-glass shaped density distribution for a thermal cloud with a peak density of $\rho_{\mathrm{th}} = 2.7 \times 10^{17}\,\mathrm{m}^{-3}$ as discussed in section 4.5.2 and illustrated in appendix B.1. The mean nearest ion-ion distance in this distribution is 1.4(9) µm. The short range Coulomb cutoff was set to 5 nm and the time step was set to 1 fs to catch the dynamics with reasonable conservation of energy yielding a total deviation of $\Delta E_{\mathrm{tot}} < 0.1\,\%$ at the end of the simulated time.

#### Electron trajectories

We created the electrons paired with the ions as discussed above and choose circular orbits with different radii for each simulation. Figure 4.13 shows the results for simulations for initial electron-ion radii corresponding to the maximum of the radial $s$-state wavefunction for $n = 13$, 27 and 50 (a-c). All measures in the figures are plotted in dependency on the time over a span of 2 ns. The figures in the first row show the distance from each electron to the nearest ion $d_{\mathrm{Rb,e}}$. Initially, all electrons have the same distance to the nearest ion - the initial electron-ion radius depends on the principal quantum number, which amounts to 17 nm for $n = 13$ (a), 105 nm for $n = 27$ (b) and

418 nm for $n = 50$ (c). For the lowest principal quantum number, the bound states remain stable and there is only a slight deviation over time. In this case the orbits are not large enough to significantly influence each other at the given density. For $n = 27$ (b), the trajectories of the electrons are rapidly disturbed and for $n = 50$ (c) there is a significant amount of electrons following orbits that exceed the ion-ion distance, suggesting that these electrons are outside of the ion cloud.

### Electron classification

We can classify the electrons according to their kinetic energy into bound states, plasma electrons and free electrons:

$$\begin{aligned} E_{\mathrm{k,e}} &\leq E_{\mathrm{C,NN}} &&\Rightarrow \text{bound state} \\ E_{\mathrm{C,NN}} < E_{\mathrm{k,e}} &\leq E_{\mathrm{C,tot}} &&\Rightarrow \text{plasma electron} \\ E_{\mathrm{k,e}} &> E_{\mathrm{C,tot}} &&\Rightarrow \text{free electron} \end{aligned} \tag{4.6}$$

Where $E_{\mathrm{k,e}}$ is the kinetic energy of the electron, $E_{\mathrm{C,NN}}$ the potential energy the electron experiences from its nearest ion neighbor and $E_{\mathrm{C,tot}}$ is the potential each electron experiences from the whole particle distribution (i.e. the attractive potential of *all ions* and the repulsive potential of *all electrons*). The bound electrons, are electrons that are bound to their nearest ion as described above, the plasma electrons are bound to the collective Coulomb potential of all ions (with included electron repulsion) and the free electrons are electrons that are neither bound to their nearest ion neighbor, nor to the collective potential. This differentiation by energy between different classes of electrons is much more precise than the spatial separation used in chapter 3.
The second row of plots in figure 4.13 shows the ratio of these electron classes: For $n = 13$ (a), all electrons remain in bound states (light turquoise) within the simulated time span. For the ensemble with $n = 27$ (b), approximately 1 % of the bound states ionize each other by perturbing their respective Coulomb potentials and the electrons escape as free electrons. At the highest shown quantum number $n = 50$ (c), again, part of the bound states ionize up to a total ratio of approximately 5 %. After that a plasma forms and up to approximately 17 % of the initially bound electrons take part in the plasma dynamics.

### Evolution of the binding energy

The last row of plots shows the deviation of the mean binding energy $\Delta\bar{E}_{\mathrm{b}}$ of all bound states from its initial value $\bar{E}_{\mathrm{b,0}}$ in dependency on the time. While it remains constant for the case where we have low principal quantum number and no ionization events (a), there is a slight decrease over time for $n = 27$ (b) and an even stronger decrease for $n = 50$ (c). This is a direct result of the Rydberg-Rydberg ionization occurring in these systems: When a bound state is ionized by another bound state, energy conservation requires the remaining bound state to decay into a lower, more deeply bound state.
The underlying classical model does of course not reproduce the discrete atomic spectrum and realistic quantum mechanical electron orbitals. Yet this model case suggests that our methods allow us to simulate stable Rydberg ensembles as well as the expected

transfer into plasma dynamics via Rydberg-Rydberg interaction for higher principal quantum numbers or higher densities.

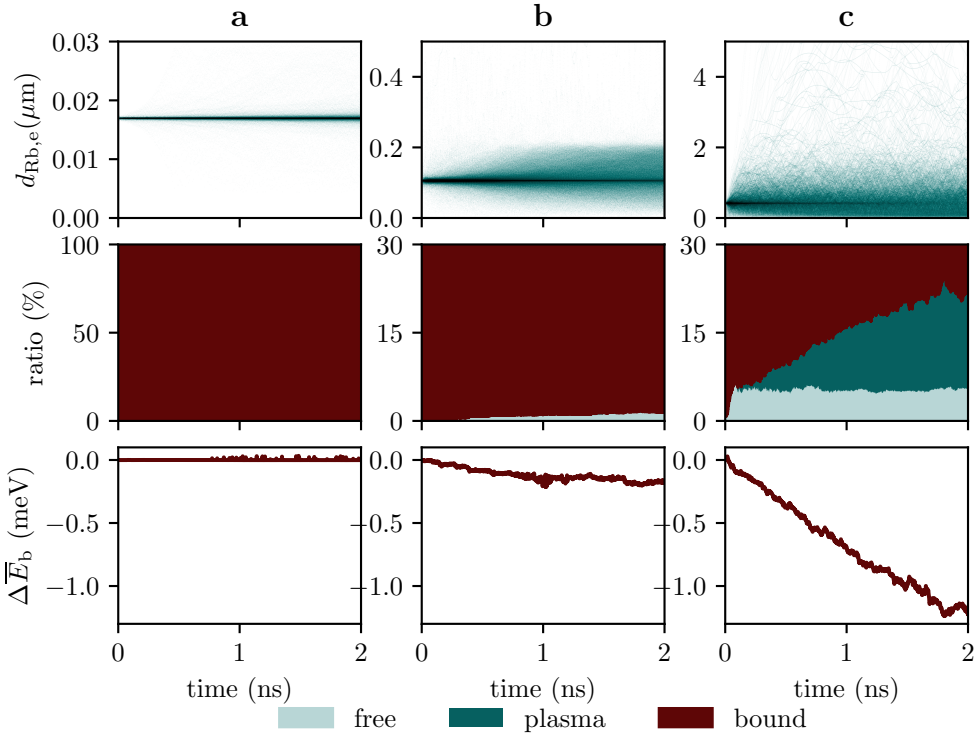


**Fig. 4.13: Simulated electron dynamics in samples of pure Rydberg atoms.**
As initial ion distribution the configuration with a thermal cloud as target discussed in section 4.5.2 is used. The first row of figures shows the distance from each electron to the nearest ion neighbor $d_{\mathrm{Rb,e}}$. The second row shows the ratio of bound (red), plasma (dark turquoise) and free electrons (light turquoise) separated by energies (eq. (4.6)). The third row shows the deviation of the mean binding energy $\Delta\bar{E}_{\mathrm{b}}$ of the bound states from its initial value (red). All measures are plotted in dependency on the time. **a.** The electrons were initially set on circular orbits corresponding to the maximum of the radial s-wave-function for $n = 13$. Almost all electrons retain their initial radius with $d_{\mathrm{Rb,e},0} = 17\,\mathrm{nm}$ and only minor deviations can be observed. All electrons remain in bound states and the mean binding energy of the bound states remains constant. **b.** The radius was set in the same manner for principal quantum number $n = 27$, yielding $d_{\mathrm{Rb,e},0} = 105\,\mathrm{nm}$. Over the course of the simulated 2 ns the orbits of the electrons are significantly perturbed by Coulomb interaction between the electrons and ions. A small amount of bound states ionizes due to these interactions and free electrons escape the system. The energy necessary to free these electrons can be seen as a reduction in binding energy of the remaining bound states. Ionization events are thus compensated by electrons in bound states moving to more deeply bound trajectories. **c.** When starting with bound states corresponding to a principal quantum number of $n = 50$, most of the bound electron trajectories almost instantly transfer into plasma electrons with trajectories within and around the ion cloud. Here $d_{\mathrm{Rb,e},0} = 418\,\mathrm{nm}$ is on the order of half the ion-ion-distance. The ratio of free electrons quickly increases within the first 100 ps and saturates at 5 %. After that more ionization events lead an increase in plasma electrons up to a ratio of $\approx 17\,\%$ by the end of the simulation. The remaining bound states again move to more deeply bound trajectories balancing the energy necessary for the ionization .

## 4.6 A simulative study at BEC densities

To understand the underlying dynamics of the measurements, we perform simulations with the density distribution corresponding to a BEC discussed in section 4.5.2 and femtosecond laser pulse wavelengths of 588 nm, 593 nm, 598 nm, 603 nm, 613 nm, 623 nm, 628 nm, 633 nm and 638 nm under consideration of the two-photon process as well as the three-photon process, where the ratio of the three-photon process is extracted from the measurements (see figure 4.12). The ion distribution is held constant for each simulation, thereby no absolute change in particle number is taken into account and only the electron energies were varied. The Coulomb cutoff is set to 2.5 nm and the time step is set to 1 fs, yielding a simulation speed of approximately 1.1 iterations per second. For the 2 ns of simulated time presented here, each simulation ran approximately 21 days on an up-to-date desktop computer with a 3.3 GHz processor with four cores.

### 4.6.1 Microscopic electron dynamics

The electron dynamics when scanning the wavelength of the femtosecond pulse across the two-photon ionization threshold can be qualitatively understood by further examining the simulation results for three wavelenghts: 588 nm, 603 nm and 623 nm. The first two are close to threshold - one above, the other below. The third wavelength is well below the ionization threshold. For these particular cases the three-photon ratios were set to 70 %, 65 % and 50 % (similar to the results presented in 4.3, yet extracted at an earlier stage in the experiment).

#### Electron trajectories outside the ionic cloud

Figure 4.14a-c summarizes the microscopic electron dynamics for the three cases. In the first row the distance from each electron to the nearest ion $d_{\mathrm{Rb,e}}$ is plotted in dependency on the time within a time span of 2 ns and a range of 0 µm to 100 µm (dark turquoise).
The almost vertical lines present at all wavelengths (a-c, first row) correspond to electrons that escape the ionic cloud at the beginning of the dynamics. Since all wavelengths are close to or below the two-photon ionization threshold, these are electrons from three-photon ionization with excess energies on the order of 2 eV. Despite their high excess energies, some of these electrons are trapped in the course of the plasma dynamics on very large orbital trajectories ranging from 10 µm to >100 µm in radius. At all three wavelengths we observe these large orbital trajectories around the ionic cloud, yet for the wavelength far below the two-photon ionization threshold (c, first row) only a small number on the order of ten electrons is trapped this way. These large trajectories of plasma electrons can also be found in the highly charged microplasma (see previous chapter, figure 3.5) as well as the plasma evolving from ensembles of Rydberg atoms in a thermal cloud (see fig. 4.13). The presence of this feature in all cases indicates that these trajectories are a direct result of the small size of the system and not necessarily triggered by high electron excess energy in the beginning of the dynamics.

### Plasma electrons inside the ionic cloud

In the second row of figure 4.14a-c, the smaller ion-electron distances between $d_{\mathrm{Rb,e}} = 0\,\mu\mathrm{m}$ to $0.5\,\mu\mathrm{m}$ are depicted that are not resolved in the long-distance plots in the first row. The dashed red line corresponds to the mean nearest ion-ion distance $\bar{d}_{\mathrm{Rb,Rb}}$ with standard deviation given by the dotted red lines.
For the simulations with pulse wavelengths of 588 nm (a, second row) and 603 nm (b, second row), electrons are concentrated at a distance of approximately half the ion-ion distance $\bar{d}_{\mathrm{Rb,Rb}}$ and are thus plasma electrons that move within the ionic cloud. While the plasma within the ionic cloud is almost instantly triggered at these shorter wavelengths, it takes some time to accumulate electrons on trajectories that are bound within the ion cloud further below the threshold (c, second row). The exact trajectories of these electrons can not be followed in this representation anymore because the nearest ion constantly changes on the electron's way through the ionic cloud, explaining the diffuse nature of the signal.

### Electrons bound in Rydberg states

While the case for 588 nm only shows the plasma electrons within the ionic cloud (fig. 4.14a, second row), we see an additional concentration of electrons at $d_{\mathrm{Rb,e}} < 0.05\,\mu\mathrm{m}$ for 603 nm (b, second row) and 623 nm (c, second row). This feature correspond to the Rydberg states we create when we tune the wavelength below the two-photon ionization threshold and is obviously not present or expected above the threshold.
At a wavelength of 603 nm (b, second row) the electrons in Rydberg states slowly vanish over the course of the 2 ns of simulated time. For a wavelength of 623 nm (c) the electrons in bound states persist throughout the simulation.

### Evolution of electron classes

A more quantitative approach to the evolution of the different electron classes can be seen in the last row of figure 4.14a-c. To this end, we distinguish the electrons into three classes as stated in equation (4.6), separating electrons bound to single ions (red), electrons taking part in the plasma dynamics (dark turquoise, this includes electrons on large orbital trajectories as well as electrons in the plasma within the ionic cloud) and free electrons (light turquoise) that escape the system.
In the first plot (a, last row) we can see that there are no persisting bound states in the case of a pulse wavelength of 588 nm. The numbers of plasma electrons and free electrons remain almost constant after an initial exchange from free electrons to plasma electrons within the first picoseconds due to the initial charge separation triggered by the escaping electrons from three-photon ionization. This case strongly resembles the highly charged plasma discussed in the previous chapter.
At 603 nm (b, last row) the plasma dynamics is different: There is still a transition from free electrons to plasma electrons within the first picoseconds, however the majority of plasma electrons emerges from previously bound Rydberg states. Within the first 0.5 ns almost all bound states transfer into plasma electrons.
Further below the two-photon ionization threshold at a pulse wavelength of 623 nm (c, last row), there still is a transfer of bound states into plasma electrons, but it is on a

much longer time scale, yielding a much smaller plasma component while most of the bound states remain intact at the end of the simulation time.

The difference in the timescales of the transfer of the bound states into plasma electrons can serve as an explanation why we only see a clear electron Rydberg signal further below the threshold (see figure 4.7c-f) in our measurements. Close to the threshold, at 603 nm our simulation shows a fast transfer of the electrons that are initially in Rydberg states into plasma electrons, which agrees with the measurement not showing a clear Rydberg signal. At 623 nm the transfer is much slower and at the end of the simulation time most of the bound states are still intact. Indeed, here, the measurement did show a clear Rydberg signal.
The difference to the thermal target can be explained by considering the distinctively different densities: Bound states at 603 nm might ionize each other at the density of a BEC, but not influence each other at the density of a thermal cloud (where we did record a distinct Rydberg electron signal). The three-photon ratio in the measurement with the thermal cloud is also much lower further reducing the density of positive charge and removing mobile electrons from the system that can ionize bound states. We will investigate on the role of the three-photon electrons in the next subsection.

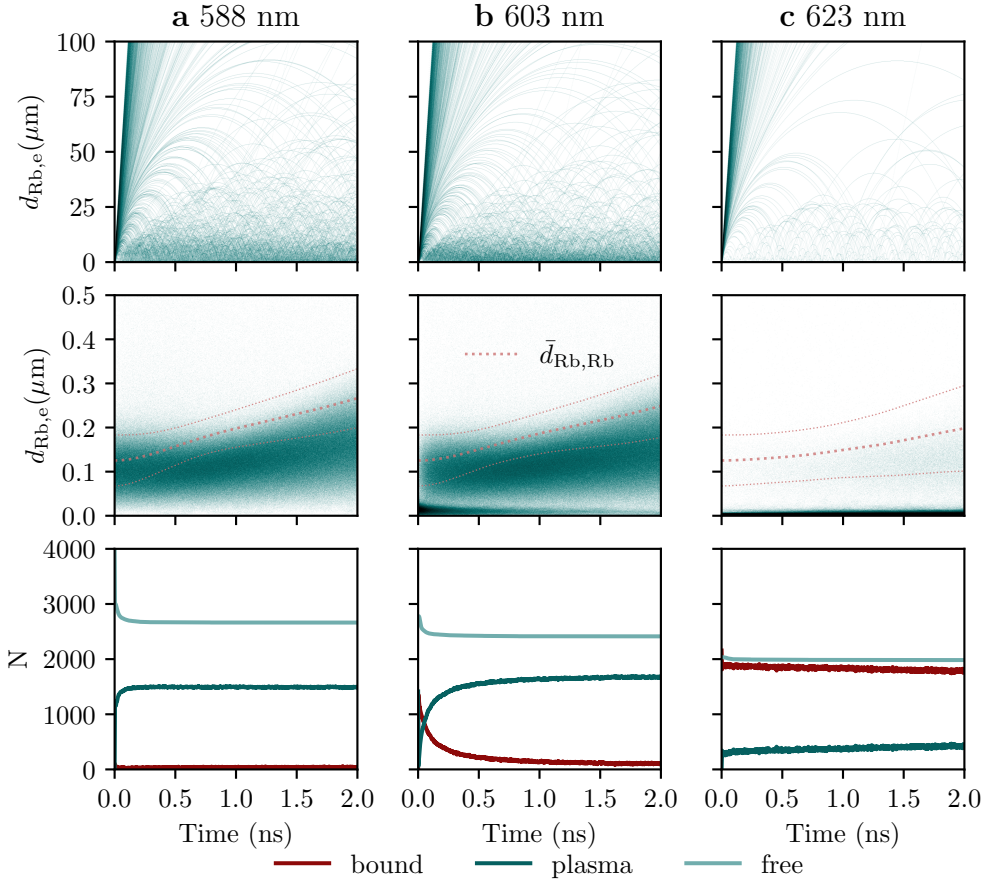


**Fig. 4.14: Electron dynamics above and below the two-photon ionization threshold.** The figures show the distance from each electron to the nearest ion neighbor $d_{\mathrm{Rb,e}}$ on a long range (top row) and short range length scale (center row) close to the mean ion-ion-distance $\bar{d}_{\mathrm{Rb,Rb}}$ (dashed red line, dotted red lines mark the standard deviation). The bottom row shows the number of bound (red), plasma (dark turquoise) and free electrons (light turquoise) separated by energies (eq. (4.6)). All measures are plotted with respect to the time up to 2 ns. **a.** Simulation at a femtosecond pulse wavelength of 588 nm. The almost vertical lines in the upper trajectory plot mark the electrons from three-photon ionization. Most of them escape the system, yet some of them are trapped in plasma dynamics on large orbital trajectories with radii from <1 µm to >100 µm (top). At $d_{\mathrm{Rb,e}} < d_{\mathrm{Rb,Rb}}$ plasma electrons within the ion cloud can be observed (center). Within the first picoseconds approximately 1500 of the initially free electrons get trapped during charge separation (bottom graph). **b.** At a pulse wavelength of 603 nm the long range electron dynamics (top) are very similar to the case in (a). Besides the bulk plasma electrons in the short range regime (center) we see a concentration of electrons at $d_{\mathrm{Rb,e}} < 50$ nm corresponding to electrons bound in Rydberg states. Over the course of 2 ns, these electrons almost disappear. We observe a transfer from free to plasma electrons within the first picoseconds (bottom). Yet, there is also a slower transfer from bound states into plasma electrons on a time scale of $\approx 0.5$ ns. **c.** At a pulse wavelength of 623 nm, there are far fewer long range plasma trajectories (top). In this case the electrons forming the bulk plasma (center) slowly become visible over the course of the simulation. The feature corresponding to the electron orbits of the bound state persists throughout the 2 ns. The transition from free electrons to plasma electrons is almost completely suppressed in this regime (bottom) and after a rapid initial transfer of bound states (picosecond timescale), there is only a gradual transfer within the simulated time span.

### 4.6.2 Three-photon ionization as a catalyst for plasma formation

We repeat the simulations for a few wavelengths without three-photon ionization to isolate the effects of the associated electrons with high excess energy. Above the threshold, we only take two-photon ionization into account while we only create bound Rydberg states below the threshold (no direct ionization by the femtosecond pulse). Due to the higher density of bound states, this regime is far more challenging to simulate. To achieve reasonable energy conservation, the time step of the integrator had to be reduced to 0.1 fs. The simulation speed is only dependent on the number of particles in the system and remains constant at 1.1 it/s, thus the simulations presented here took approximately 11 days per simulation and yielded a simulated time of 100 ps.
To capture the difference between the simulations with and without three-photon ionization, it is sufficient to compare cases close to the two-photon ionization threshold. Figure 4.15 shows the first 100 ps of the evolution of the numbers of bound electrons (red), the plasma electrons (dark turquoise) and free electrons (light turquoise) for 588 nm (a), 594 nm (b) and 603 nm (c).

#### Simulations including three-photon ionization

The top row in figure 4.15a-c show the results of the simulations with three-photon ionization. Depending on the wavelength, a ratio of 70 % (a,b, top row) or 65 % (c, top row) of three-photon electrons is used (corresponding to the results of the measurement discussed in figure 4.3 at an earlier stage in the measurement).
Right above the threshold at a pulse wavelength of 588 nm (a, top row) we observe the dynamics of a highly charged microplasma: within the first picoseconds there is a transfer from free electrons to plasma electrons triggered by the charge separation due to the escaping electrons.
At the two-photon ionization threshold and a wavelength of 594 nm, the dynamics is very similar but complemented by a number of initially bound states that almost instantly transfer into plasma electrons (b, top row).
Below the threshold at a pulse wavelength of 603 nm, we observe that the transfer of the bound states takes place on a longer timescale (transfer on a nanosecond timescale, compare figure 4.14b), yet it is still pronounced and about half of the initially bound states have transferred into plasma dynamics after only 100 ps.

#### Simulations omitting three-photon ionization

The results of the simulation without the electrons originating in three-photon ionization look distinctively different:
In the case right above the threshold at a pulse wavelength of 588 nm (fig.4.15a, bottom row), almost all free electrons are trapped by the ionic cloud within the simulated time span. Accordingly, most of the electrons are plasma electrons. Although initially we do not create any electrons in bound Rydberg states in this scenario, the amount of bound states makes up about 21 % of the electrons by the end of the simulation. This is a clear representation for Rydberg recombination in our simulations expected for ultracold neutral plasma with low excess energies and electron temperatures [115]. Since

this recombination is neither visible in the simulation with three-photon ionization nor in our experiment, we conclude that the suppression of recombination is an effect of the large charge imbalance and the high energy electrons from three-photon ionization.
The case directly at the threshold at a pulse wavelength of 594 nm (b, bottom row), also shows a different behavior when no electrons from three-photon ionization are included in the simulation: again almost all initially free electrons get captured by the ionic Coulomb potential into plasma dynamics due to their low initial excess energy, here limited by the bandwidth of the femtosecond laser pulse. There is also Rydberg recombination and the number of bound states almost doubles within the first few picoseconds. After this increase, there is a slow transfer of bound states into plasma electrons.
The last simulation at a pulse wavelength of 603 nm (c, bottom row), suggests that the transfer of bound states that are initially more deeply bound is also fueled by the charge imbalance and electrons with high excess energies from three-photon-ionization. Within the 100 ps of simulated time, there is almost no transfer of bound states into plasma electrons. Only a small number is ionized and leaves the system not yielding enough residual positive charge to form a plasma and trigger further ionization events.

In conclusion, it can be noted that the inclusion of the high ratio of electrons with high excess energy from three-photon ionization in the simulations yields a suppression of Rydberg recombination close to the two-photon ionization threshold and accelerates the transfer of electrons that are initially bound in Rydberg states into plasma at wavelengths below the threshold.

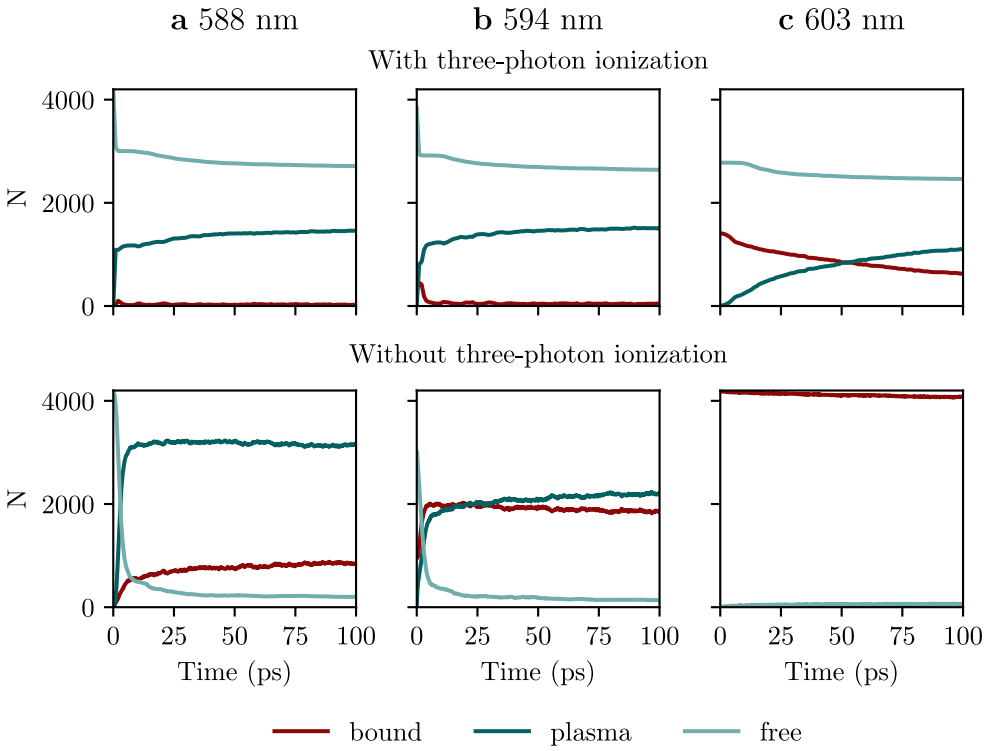


**Fig. 4.15: Comparison of electron dynamics with and without three-photon ionization.**
The numbers of electrons bound in Rydberg states (red), plasma electrons (dark turquoise) and free electrons (light turquoise) is plotted with respect to time over 100 ps. The upper figures show the results of simulations with a number of three-photon ionization events depending on the wavelength (70 %, 70 % and 65 %), the lower figures show the results of simulations only taking the two-photon processes into account. **a.** At a wavelength of 588 nm only free and plasma electrons take part in the dynamics. Within the first picoseconds there is a transfer from free electrons to plasma electrons due to the charge separation and the recapture of escaping electrons (top). Without three-photon ionization (bottom), almost all electrons are captured in the plasma due to the significantly lower excess energy. Furthermore, at the end of the simulation about 21 % of the electrons are in bound states, suggesting Rydberg recombination. **b.** At a pulse wavelength of 594 nm at the two-photon ionization threshold, both free electrons as well as electrons initially created in Rydberg states transfer into plasma electrons within the first picoseconds (top). Without three-photon ionization, a significantly higher number of electrons is trapped in the plasma and the number of bound states increases within the first few picoseconds and then shows a slow transfer into plasma electrons (bottom) **c.** At 603 nm we observe a quick transfer of the initially created bound states into plasma electrons of $\approx 50\,\%$ after 100 ps with three-photon ionization (top). Without three-photon ionization, almost all bound states remain intact during the simulated time span. A few of them ionize and escape the system - there is no formation of a plasma (bottom).

### 4.6.3 Macroscopic electron dynamics : Breathing mode

Close to the ionization threshold the rapid charge separation triggered by the escaping electrons from three-photon ionization leads to a macroscopic breathing mode of the remaining plasma electrons. In figure 4.16a the column density of the electrons is shown

in the $x, z$-plane after 6 ps, 10 ps, 14 ps, 18 ps and 22 ps for the simulation with a pulse wavelength of 588 nm and full electron spectrum including three-photon ionization.
At 6 ps, most of the electrons are within the approximately cylindrical ionic cloud (where the $z$-axis is the longitudinal axis of the cylinder) while few electrons are outside of the ionic cloud either on large orbital or escaping trajectories. Within the next 8 ps to 9 ps the ensemble of plasma electrons contracts along the $z$-axis until it starts to expand again completing a whole cycle of a breathing mode within approximately 16 ps to 18 ps. By extracting the FWHM $w$ of the linear electron density after integration over two axes and fitting a dampened oscillation given by

$$w(t) = A \cdot \exp(-t/\tau) \cdot \sin(\omega t + \phi) + w_0 \tag{4.7}$$

we can extract the amplitude $A$, the angular frequency $\omega$ and initial phase $\phi$ of the oscillation, the time constant of the exponential decay $\tau$ and the mean FWHM $w_0$.
In figure 4.16b the FWHM of the electron linear density $\rho_\mathrm{e}(z)$ along the $z$-axis is plotted (turquoise dots) with the result of the corresponding fit (red line). The light turquoise dashed vertical lines mark the points in time of the column density profiles shown in (a). For the $x$ and $y$ axis we find that the oscillation period $T = \frac{2\pi}{\omega}$ is equal for both axes (within the margin of errors) and amounts to $T_x = 9.1(2)$ ps ($T_y = 9.2(6)$ ps), while it is almost twice as high for the $z$-axis with $T_z = 17.8(1)$ ps. $x$ and $y$ are the radial axes of the initially cylindrical density distribution, while the $z$-axis is the longitudinal axis suggesting that the difference in timescales is due to the geometry of the charged particle density.
A similar, yet more subtle phenomenon can be seen as an oscillation in the kinetic energy of the plasma electrons within the first picoseconds in the highly charged microplasma discussed in the previous chapter (see figure 3.6a, light turquoise). Previously we associated the period of this oscillation with the inverse of the plasma frequency $\omega_\mathrm{p,e}^{-1}$ (equation (3.5)). The *radial* breathing mode we observe in our simulations for a pulse wavelength of 588 nm does indeed fit the timescale $T_\mathrm{p} = 2\pi/\omega_\mathrm{p,e} = 8.8$ ps for an initial electron density of $\rho_\mathrm{e,0} = 1.6 \times 10^{20}\,\mathrm{m}^{-3}$. However, the deviation along the $z$-axis by approximately a factor of two suggest that this oversimplifies the situation and that the broken symmetry in our initial particle distribution leads to two timescales depending on the axis. In fact, due to the small system size the plasma electrons can not be viewed as a displaced electron gas that oscillates *within* an ion gas. A better image would be that of an ensemble of electrons oscillating in the collective potential well of an ion cloud, not necessarily restricting the electrons to be *inside* the cloud. The initial charge separation due to the escaping electrons originating in three-photon ionization can then be seen as quench of this potential from a neutral particle distribution at $t = 0$ without a potential well to a positively charged distribution with a deep Coulomb well that retains the cylindrical symmetry of the ion distribution and thus features two different frequencies of oscillation.

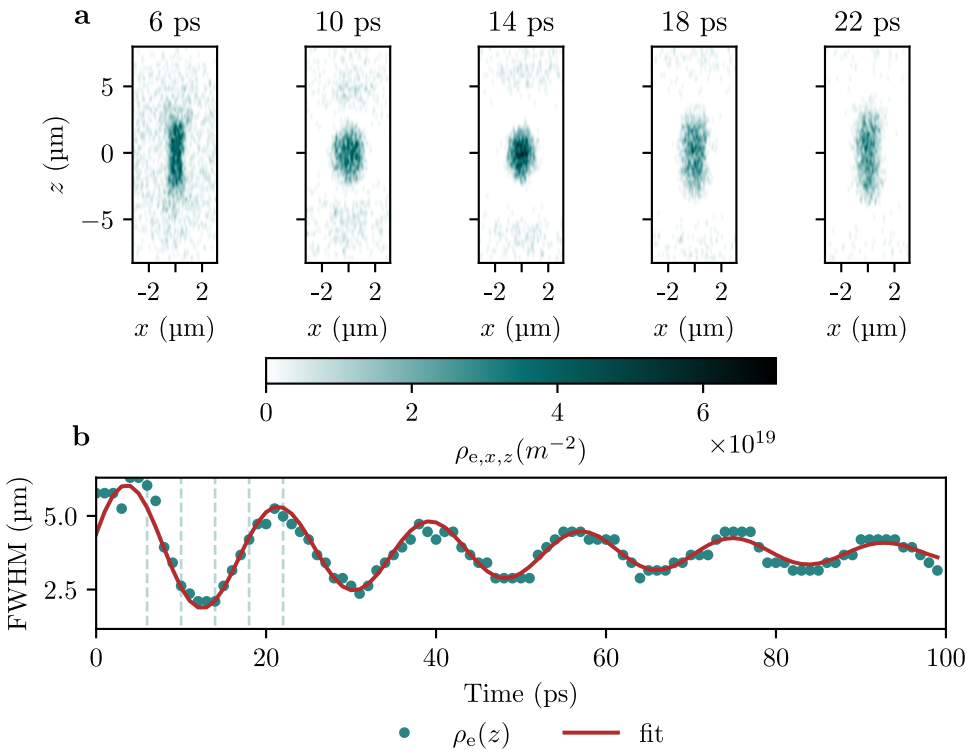


**Fig. 4.16: Collective breathing mode of the electrons.**
**a.** Electron column density in the $x, z$-plane after 6 ps, 10 ps, 14 ps, 18 ps and 22 ps for the simulated plasma dynamics at 588 nm with apparent breathing mode. **b.** FWHM of the electron linear density in $z$-direction $\rho_e(z)$ (turquoise dots) and fit (dark red line) with a dampened oscillation (eq. (4.7)). The dashed lines (light turquoise) mark the position in time of the shown density profiles in (a). For the $z$-axis we find an oscillation period of $T_z = 17.8(1)$ ps, for the radial axes $x$ and $y$ we find $T_x = 9.1(2)$ ps and $T_y = 9.2(6)$ ps. The difference between the axial and radial oscillation periods originates in the cylindrical geometry of the initial ion configuration.

### 4.6.4 Ion dynamics: Coulomb expansion

The charge imbalance originating in the large amount of escaping electrons from the three-photon ionization yields an ensemble that is in total positively charged. Due to this charge the ions will expand by transferring potential energy into kinetic energy. We do not expect to capture the whole ion dynamics in the 2 ns of simulated time because of the high mass of the ions. However, we do find evidence for the double structure visible in the measurements (see figure 4.9).
To get a qualitative viewpoint, figure 4.17a-c shows the column densities of the ion cloud normalized to its maximum value for different times and pulse wavelengths. The first column (a) shows the approximately cylindrical ion distribution at $t = 0$ taken from the simulation with a pulse wavelength of 588 nm. Since we use the same ion distribution for each simulation, this is representative for all wavelengths at $t = 0$. The upper plot shows the column density in dependency on the $z$ and $x$-axis (side view), while the

lower plot shows the column density in dependency on the $y$ and $x$ axis (top view). At the end of the simulation time at $t = 2\,\mathrm{ns}$ the ion cloud has significantly expanded along the $x$ and $y$ direction, while the expansion along $z$ appears to be slower (b).
When the pulse wavelength is set to 623 nm, where we still have a large number of bound states at the end of the simulation at $t = 2\,\mathrm{ns}$ (see figure 4.14c), we see a distinct double structure in the ion cloud after expansion (c). While ions that are not paired with bound electrons expand freely (though not as fast as above the threshold due to their reduced number), ions that are paired with electrons in Rydberg states do not expand since they can be considered as neutral atoms. This double structure closely resembles the double structure seen on our detector - bound states do not take part in the initial Coulomb explosion if they are ionized at later times.
In figure 4.18a the velocity of each ion is plotted in dependency of its traveled distance for the simulation with a pulse wavelength of 588 nm at $t = 2\,\mathrm{ns}$ above the two-photon ionization threshold. The expansion of the ions closely resembles that of a homogeneous distribution of charges, which would show a proportionality between traveled distance (or distance to the center of the cloud) and velocity in the far field (i.e. after sufficient time of expansion). The fastest ions are those that are located on the surface of the ion cloud - these ions also travel the furthest within the simulated time. The almost linear dependency between traveled distance and velocity without any bunching or clusters suggests that there is no formation of shock waves or spatial correlations between the ions in the simulation.
Still, a closer look reveals the influence of the initial cylindrical symmetry and shows that after 2 ns we are not yet in the far field of the expansion: The color shading corresponds to the initial $z$-position of the ions, darker red means that $|z_0|$ is larger (ions started closer to the top or bottom base of the cylinder) while lighter red marks ions closer to the center of the cylinder. The ions starting from the top and bottom base of the cylinder appear slightly faster than ions that have traveled an equal distance but started closer to the center.
In figure 4.18b the same representation for a pulse wavelength of 623 nm (below the two-photon ionization threshold) is plotted. Here, we clearly see the double structure discussed above: While most of the ions still expand in the homogeneous manner as shown in figure 4.18a , the ions belonging to bound states remain at their initial positions (grey circle). Also the maximum velocity and traveled distance is smaller than in the simulation above the threshold since less ions take part in the Coulomb expansion and there is less positive charge.
In the results of the measurements we observed a correlation between the area of the ion signal on the detector as a measure of the Coulomb expansion and the absolute number of charged particles (i.e. the total brightness on the electron detector). In the simulations, we keep the number of charged particles constant for all wavelengths. Here, we find a clear correlation between the Coulomb expansion and the number of electrons from three-photon ionization. In figure 4.18c, the final RMS radius of the ion distribution $r_{\mathrm{i,RMS}}$ is plotted against the initial ratio of electrons from three-photon ionization suggesting a linear dependency.
The pulse wavelengths used in the simulations span a range from 588 nm to 638 nm trigggering vastly different dynamics from highly charged plasma to self-ionizing Rydberg ensembles, yet the dominating parameter for the speed of the Coulomb expansion

is the neutrality of the remaining cloud. It seems to depend solely on the charge density of the ionic cloud which in our case scales with the three-photon ionization ratio and the number of (persisting) bound states. The plasma electrons play an ambiguous role in these dynamics: while the electrons of the bulk plasma within the cloud effectively shield the ions from each other and thus dampen the Coulomb expansion, the electrons on large orbital trajectories around the ion cloud would lead to an acceleration, pulling the ions outwards.

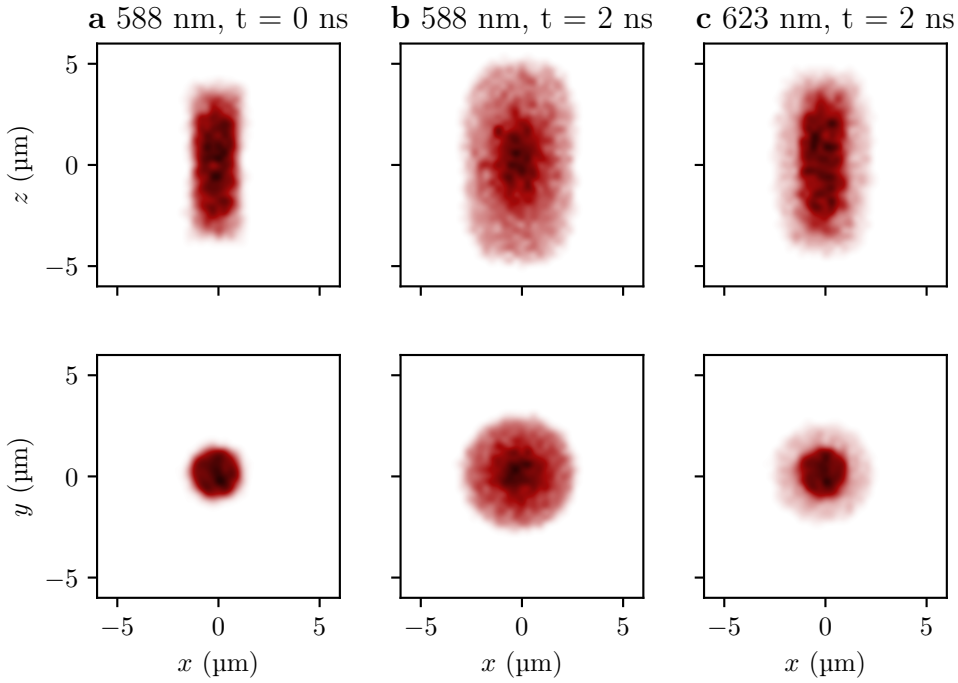


**Fig. 4.17: Normalized ion column density.**
**a.** Initial ion column density along $x$ and $z$ (top) and $x$ and $y$ (bottom) normalized to their respective maximum values and extracted from the simulation at a femtosecond pulse wavelength of 588 nm. This configuration at $t = 0$ is equal for all simulations (only the energies of the electrons were varied). **b.** The same simulation at $t = 2$ ns. The cloud has expanded to about twice the initial radius due to repulsive Coulomb interaction between the ions. The still elongated shape suggests, that we are still at the beginning of the expansion. **c.** Ion column density from the simulation with a pulse wavelength of 623 nm, where a significant amount of bound states are still present in the system at the end of the simulation ($t = 2$ ns). Here, only the free ions take part in the Coulomb expansion and within the expanded cloud a cylinder of ions in bound states with electrons with approximately the size of the initial ion distribution remains.

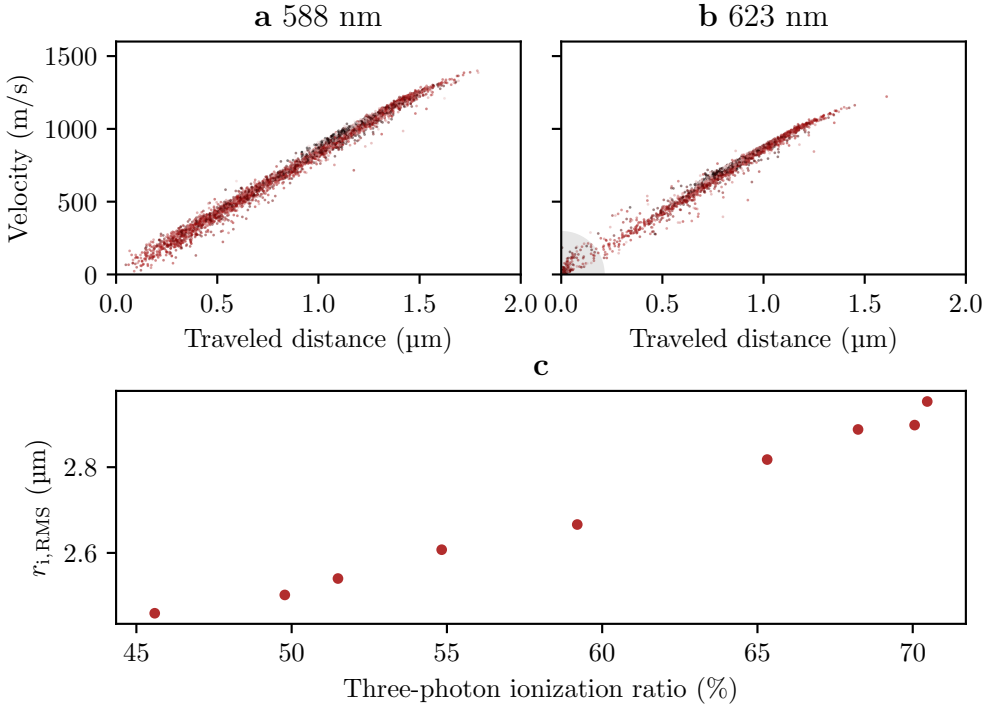


**Fig. 4.18: Ion expansion above and below the two-photon ionization threshold.** **a.** Velocity of each ion in dependency on the traveled distance at $t = 2\,\mathrm{ns}$ in the simulation with a pulse wavelength of 588 nm. The distribution of ions in this representation closely resembles that of a homogeneously expanding cloud, which would show a linear dependency between velocity and traveled distance in the far field of the expansion. The color shading marks the initial absolute $z$ position $|z_0|$ showing the influence of the initial cylindrical geometry where darker colors mark ions at the base and top of the initial distribution. There is no formation of shock waves or spatial correlation. **b.** The same representation of the ion expansion taken at $t = 2\,\mathrm{ns}$ of the simulation with a pulse wavelength of 623 nm. Here, we obtain a bipartite distribution: While most of the ions still expand in the manner described in (a), there is also an ensemble of ions that remains at its initial positions (grey circle). These are the ions in bound states which form the double structure shown in both, experimental data (figure 4.9) as well as ion column density (figure 4.17). **c.** The RMS radius of the ion cloud $r_{\mathrm{i,RMS}}$ at the end of the simulation ($t = 2\,\mathrm{ns}$) is plotted in dependency on the ratio of three-photon ionization. There is a clear correlation between the final size of the ion cloud and three-photon events since the expansion is driven by the positive charge left in the cloud.

### 4.6.5 Conventional plasma parameters: Temperature and coupling parameter

So far we omitted making claims about the common *macroscopic* parameters used to describe ultracold plasma like the electron and ion temperature or the coupling parameters $\Gamma_{\mathrm{e,i}}$. This is done in the knowledge that the small size of our system and the transition between bound states and plasma electrons as well as the orbital trajectories of the electrons spanning orders of magnitudes in radius require a *microscopic* description of the system. Also, the definition of temperature common to plasma systems,

where it is simply set equal to the kinetic energy (see equation (3.2)) fails at the transition to bound states. Here, a bound electron can have a high kinetic energy on its orbit around the ion, while the *excess* kinetic energy is zero. For the plasma electrons close to the transition to bound states the situation is similar: High kinetic energies are not necessarily associated with high temperatures.
To this end we propose to regard each plasma electron in the frame of reference of its nearest ion. The zero point of the *excess* kinetic energy is then given by the equality between kinetic energy of the electron and the binding energy between electron and ion. To calculate the temperature of the plasma electrons we simply add the (negative) binding energy to the nearest ion $E_\mathrm{b}$ to the total kinetic energ $E_\mathrm{e,k}$ electron:

$$E_\mathrm{k,e,exc} = E_\mathrm{e,k} + E_\mathrm{b} \tag{4.8}$$

and then use the conventional equality with temperature (eq. (3.2)). The electron-electron and ion-ion-coupling parameter can then be calculated using equation (3.3). We approximate the Wigner-Seitz-radii $a_\mathrm{e}$ and $a_\mathrm{i}$ with half of the mean nearest neighbor distance of either the plasma electrons or all ions.
In figure 4.19a the coupling parameters are plotted for 588 nm, 594 nm and 623 nm (colors from light to dark), for both components: ions (red) and plasma electrons (turquoise) in dependency on the time for the scenarios close to the experimental conditions with a BEC as target including three-photon ionization. The ions start strongly coupled (in fact the initial coupling parameter is infinite, since we start with stationary ions in the simulations) but quickly decreases into the weakly coupled regime. While the simulations above and at the threshold show an almost equal development, the simulation further below the threshold at 623 nm shows a slower decrease in the coupling parameter over time. This is probably due to the many ions and electrons in bound states at this wavelengths, dampening the Coulomb expansion of the system. The coupling parameter of the plasma electrons decreases within the first $\approx 250$ ps and then remains almost constant, never transcending the weekly coupled regime.
In figure 4.19b the corresponding temperatures are plotted against the simulated time. The ions temperature/kinetic energy (red) is clearly dominated by the Coulomb expansion and increases over time according to the charge density in the system. While 588 nm and 594 nm were simulated with the same amount of electrons from three-photon ionization and the difference in their ion expansion originates in the difference in excess energy, the simulation at 623 nm was started with a lower amount of electrons from three-photon ionization. This lower charge imbalance and the presence and persistence of bound states below the threshold result in a lower final temperature.
The temperature of the plasma electrons (figure 4.19b, blue) decreases over time with the expanding ion cloud, similar to the dynamics observed in the highly charged microplasma (see figure 3.6b). Here, the initial temperature seems to follow the initial energy of the electrons, yielding the highest temperature above the threshold and the lowest temperature below the threshold. For the two wavelengths close to the threshold (588 nm and 594 nm) an oscillation in temperature and thus kinetic energy can be observed in the first few picoseconds. This can be identified with the breathing mode described in the previous section 4.6.3 triggered by the initial charge separation.

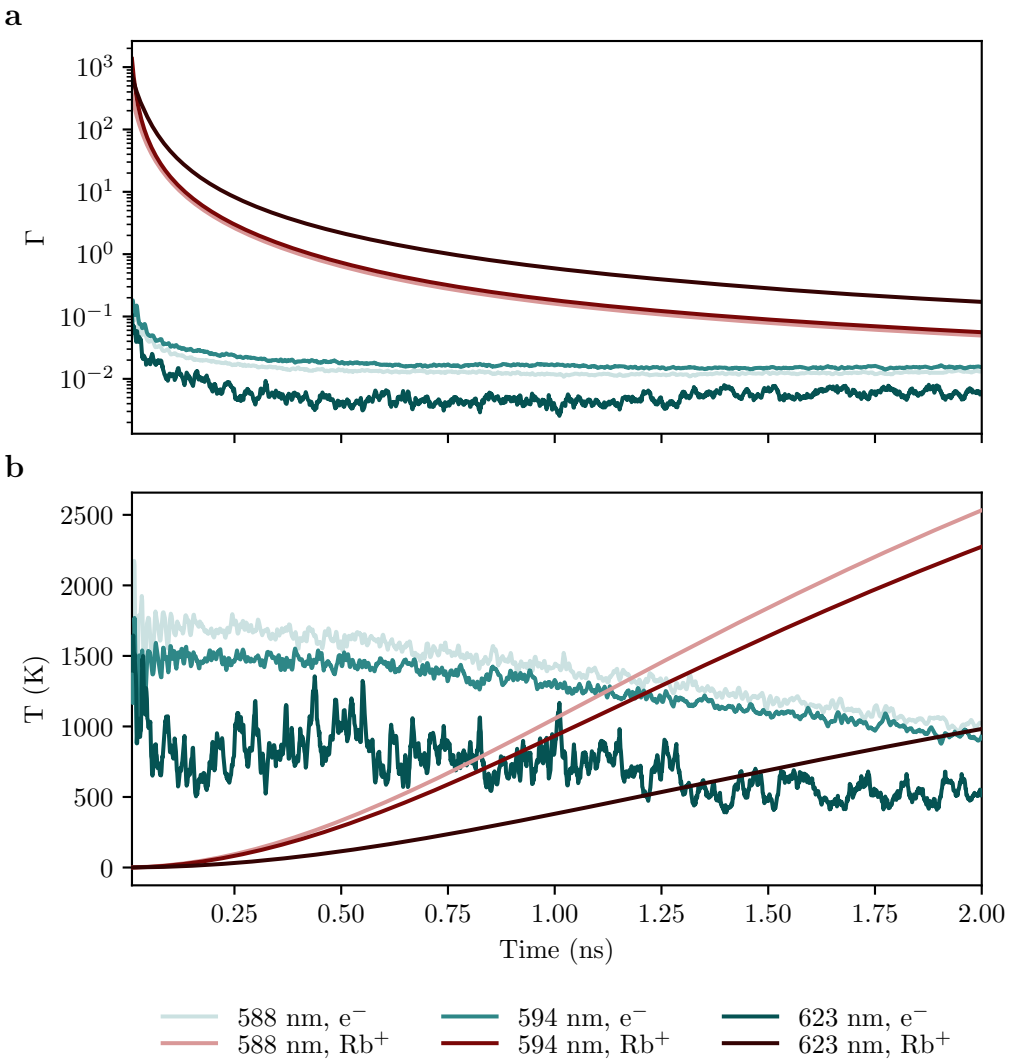


**Fig. 4.19: Macroscopic plasma parameters.**
**a.** Coupling parameter for plasma electrons (turquoise) and ions (red) in dependency on the time extracted from the simulations with pulse wavelengths of 588 nm (light colors), 594 nm, (medium light colors) and 623 nm (dark colors). The ions show initially a strong coupling ($\Gamma_i \gg 1$) that is reduced to weak coupling within less than 1 ns. The simulations with longer wavelengths show a stronger coupling at the end of the simulation due to the presence of bound states. The plasma electrons are always weakly coupled. **b.** Temperature defined by the kinetic energy (eq. (3.2)) for ions and plasma electrons at the same wavelengths as in (a) (with the same color code). The ion temperature increases over time due to the Coulomb expansion and decreases towards longer wavelengths, due to the presence of bound states that do not take part in the Coulomb expansion. The plasma electrons show an initial oscillation in temperature (and kinetic energy) on the picosecond timescale due to the initial charge separation and the breathing mode discussed in section 4.6.3. On the nanosecond time scale there is a continuing decrease in temperature driven by the Coulomb expansion as observed in the dynamics of the highly charged microplasma.

## 4.7 Conclusion

In this chapter we investigate plasma systems emerging from the excitation of an ultracold cloud of $^{87}$Rb with femtosecond laser pulses above and below the two-photon ionization threshold. We briefly explain the motivation to vary the wavelength of the femtosecond excitation pulse to reduce the excess energy of the photoelectrons and tune the initial parameters of the emerging plasma dynamics towards stronger coupling and more neutral systems.
We then present measurements on an ultracold thermal cloud and a BEC locally excited with femtosecond laser pulses at wavelengths above, at and below the two-photon ionization threshold. We thoroughly analyze the recorded electron signals and are able to separate electrons taking part in the plasma dynamics from electrons ionized by three-photon processes and electrons from Rydberg excitation and ionization.
Above the threshold we find evidence for similar dynamics as discussed in the previous chapter with rapid electron cooling in an ultracold microplasma. Below the threshold we still observe cold electrons from plasma dynamics and verify Rydberg excitation by ionizing the Rydberg atoms with a second ionization pulse from the dipole trap. Here, the thermal cloud shows significantly more electrons from this process than the BEC. Also, the Rydberg signal is suppressed close to the threshold for a BEC in favor of increased plasma ratio suggesting a transfer of Rydberg atoms into plasma electrons that is amplified by the high density of the BEC.
We also find that three-photon ionization plays a significant role when a BEC is used preventing the creation of neutral plasma systems due to the large number of escaping electrons.
The ion signal from these measurements gives insight into the Coulomb expansion of the cloud and shows further evidence of the Rydberg excitation below the threshold in form of a double structure of slow ions present in the distribution that do not take part in the initial expansion.
To gain access to the underlying dynamics down to the picosecond timescale we employ molecular dynamics simulations using the "SARKAS - Python MD code for plasma physics" [117]. To include bound states in our simulations, we elaborate on the classical atom model emerging from the Coulomb interaction between ion and electron. We show that within the bounds of our model pure samples of Rydberg atoms at the density of a thermal cloud can already show a transfer into ultracold plasma depending on the radius of the initial electron orbit.
The simulations performed at parameters resembling those of our measurements with a BEC further reveal the microscopic electron dynamics with a strong transfer of bound states into plasma electrons near the threshold, while the bound states further below the threshold remain more stable. By comparing simulations with and without three-photon ionization, we are able to show that the positive charge left behind by these events and the electrons with high excess energy serve as a catalyst for the transfer of the bound Rydberg states into plasma electrons below the threshold. Above the threshold we find evidence that the high amount of three-photon ionization in our measurements prevents the Rydberg recombination we observe in the simulations without three-photon processes.
Furthermore, we discuss the macroscopic breathing mode of the simulated electron gas

close to the two-photon ionization threshold and analyze the Coulomb expansion of the ion cloud, revealing the double structure observed in the measurements. Although the focus of this work relies on a microscopic description of the small plasma systems, we also discuss the common macroscopic coupling parameters and temperatures in the simulated systems, offering a description that is suitable for plasma electrons in dense systems near the transition to bound states.

# 5 Outlook

## 5.1 Beyond ultracold neutral plasma

We transcend the regime of ultracold neutral plasma by using femtosecond laser pulses and ultracold quantum gases. The tunable excess energy of the electrons and the non-Gaussian particle distribution with high density allows for a variety of different systems to be explored. In the work presented here, we focused on the electron cooling in a highly charged microplasma and bridged the gap between Rydberg gases and ultracold microplasma by tuning the wavelength of the femtosecond laser pulse across the two-photon ionization threshold.
The use of longer pulses with a more narrow bandwidth could give a more detailed access to this transition when a balance between the circumvention of Rydberg blockade and a decent spectral resolution to selectively address higher Rydberg states is kept. Above the threshold, pulses of more than a few picoseconds disturb the ultrafast initial electron dynamics when microplasmas are created. To this end we installed a grating-monochromator at the experiment [96] providing pulses with durations of 1.00(4) ps and a bandwidth of of 0.50(17) nm close to the two-photon ionization threshold.
The non-Gaussian density distribution of the microplasma we observed is a direct effect of the Thomas-Fermi density profile of the BEC and the nonlinear ionization probability for strong-field ionization. Usually, ultracold neutral plasma work with Gaussian density distributions at much lower densities and the expansion dynamics of non-Gaussian distributions has been the subject of recent studies [120].
Using a BEC as target offers the advantage that almost arbitrary geometries can be generated by using optical potentials. A plasma emerging from a BEC loaded into a deep 3D optical lattice in the MOT insulator regime avoids disorder-induced heating and provides an initial state with pronounced spatial correlations. [12]. In past efforts, atoms prepared in such a manner were excited into high lying Rydberg states with overlapping electron orbitals yielding an ionization avalanche forming an ultracold plasma [121]. It still remains to be seen if in such a correlated plasma a transition to a transient metal-like system with electronic band structures emerges and if the initial spatial correlations remain after expansion, yielding lower ion temperatures due to reduced disorder-induced-heating which allows prolonged strong coupling in the system.
Beyond spatial correlations between single ions in a 3D optical lattice, a 1D optical accordion lattice can prepare a BEC in spatially separated slices, providing a platform to study electronic systems of reduced dimensions apart from experiments with solid state materials [122, 123].

## 5.2 From many to few: Engineering hybrid quantum systems

So far we have studied plasma systems consisting of a few hundred to thousand ions and electrons at the transition to a Rydberg gas. Scaling down the number of involved particles will provide new insight into the underlying processes and grant access to new few-body systems.
To create systems of only a few charged particles in an ensemble of ultracold atoms via strong-field ionization, the ionization cross sections for two and three-photon ionization of $^{87}$Rb in strong light fields have to be precisely known. Here, we encountered blank spaces in the literature during the experiments performed at the transition between Rydberg gas and ultracold microplasma. Furthermore, ultrafast Rydberg excitation can provide a valuable tool for quantum computation on ultrashort timescales. Recent experiments have shown that laser pulses in the picosecond regime combined with atoms in optical tweezers allow for the realization of ultrafast two-qubit gates [124]. A combination of theoretical TDSE studies and experimental determination of the cross sections for both ionization and excitation with femtosecond pulses on the single-atom level will therefore be mandatory for future experiments and are well covered by the capabilities of our experimental setup.
Our experiment already allows for local ionization of a small fraction of atoms within a BEC by using a small focus waist of 1 µm, which can be further reduced to the order of 500 nm by using a glass slide of the correct thickness to compensate for the correct cover glass thickness of the objective [125]. Using double foci, two separate charge distributions within the same cloud can be generated and the interaction between either two separate plasma systems or cold ions immersed in a BEC can be studied.
Using the monochromator at our experiment we can generate picosecond pulses at the two-photon ionization threshold at 593.7 nm and ionize (single) atoms in the ultracold target with an ion temperature of 0.18(3) mK [96]. Ultrashort laser pulses thus can provide a new approach to create hybrid quantum systems consisting of ultracold ions and atoms. The possibility of sympathetically cooling and trapping the cold ions by utilizing the polarization-induced interaction between neutral atoms and ions can be explored experimentally. By admixing a few percent of Rydberg state population, the strength of this particular interaction can be significantly increased [67, 105] providing the means to enhance same-species buffer gas cooling.
We have all the tools for an experimental realization of these systems at hand including a cavity-locked narrow bandwidth laser system for Rydberg dressing and excitation [126]. So far, we were limited by the low detection efficiency of our charged particle detectors and the lack of a possibility for state selective Rydberg detection. To overcome these restrictions, a new detection unit is currently being set up and a short overview of its capabilities will be given in the next section.

## 5.3 A new charged particle coincidence detector unit for the *Ultracold and Ultrafast* experiment

To quantitatively explore the charged particles and gain access to the Rydberg states involved in the dynamics of the studied systems, a new detector unit was planned and

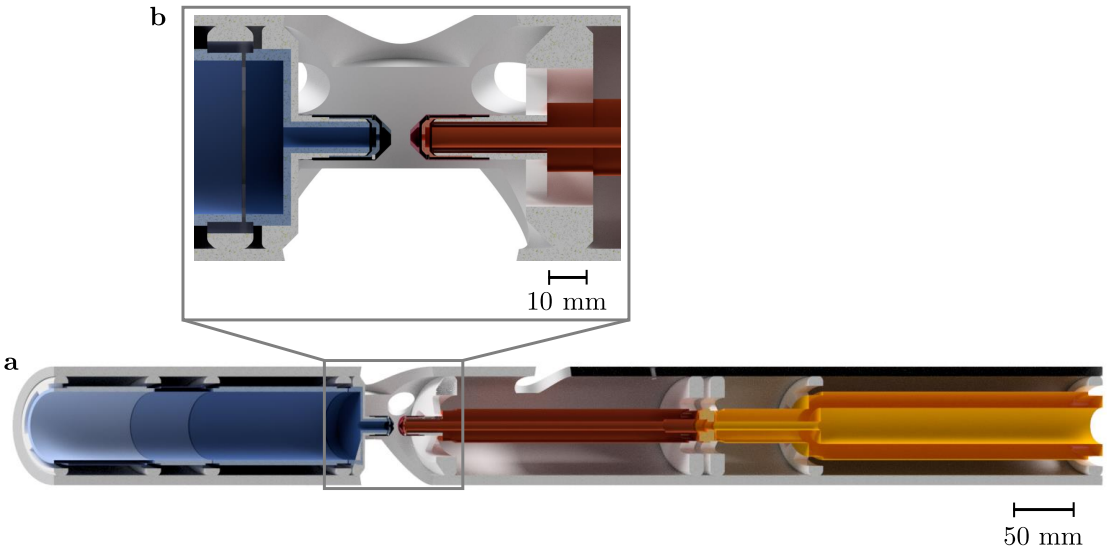


**Fig. 5.1: CAD rendering of the electrodes of the new detector setup.**
**a** The left side of the device (blue) provides electrodes for a velocity map imaging spectrometer for electrons maximizing the chromaticity of the charged particle imaging and allowing for resolution of the electron momentum in magnitude (i.e. kinetic energy) and angular distribution. The right side of the device (red) provides charged particle optics for an ion microscope that allows for magnification and imaging of the initial ion distribution. **b** Central electrodes surrounding the interaction region between ultracold atoms and femtosecond laser pulse. Due to the small distance between the first electrodes of VMI spectrometer and ion microscope, a high field gradient allows for field-ionization of Rydberg states. Figure adapted from [78]

is currently being implemented [78]. This new detector unit consists of a velocity map imaging spectrometer (VMI spectrometer) [127] for the electrons and an ion microscope [18, 19]. The detector can be operated to detect both species in coincidence.
Figure 5.1a shows a CAD rendering of the electrode design that provides the charged particle optics of the device. The VMI spectrometer (blue) can resolve the electron's momentum, both, in magnitude (i.e. kinetic energy) and angular distribution with an energy resolution of $\Delta E/E < 10\,\%$ for energies ranging from 0.05 meV to 1 meV and 0.01 eV to 8 eV. On the other hand, the ion microscope (red) offers access to the spatial distribution of the ion configuration with a magnification of 620 at a resolution of 100 nm over the entire volume of the BEC.
In figure 5.1b the first electrodes around the interaction region between BEC and femtosecond laser pulse are shown. A symmetric potential of $\pm 147$ V is applied to the first electrodes yielding a field gradient of approximately 55 kV/m which can field-ionize Rydberg atoms with $n \geq 28$ allowing for the detection of Rydberg states.
A sophisticated combination of P47-phosphor screen, fiber stack, photocathode and MCP-phosphor-screen-combination (P46) allows to detect the electrons in the VMI with a detection efficiency close to unity [128]. For the ions we expect a detection efficiency of >50 % with a CsI coated MCP and phosphor (P46) screen [129]. The electron detector will be imaged with the same highspeed camera we currently use at the

experiment (see section 2.5.2), for the ion detector a TPX3CAM[1] will be used which offers a time resolution of 1.56 ns for each pixel separately. This camera will enable us to detect ions and Rydberg atoms in a time-resolved manner - possibly allowing for reconstruction of the three-dimensional ion distribution by separating ions by arrival time.
To illustrate the capabilities of this camera, figure 5.2 shows an example image taken at the current experimental setup. Here, a single femtosecond laser pulse at a wavelength of 580 nm was applied to a BEC. The voltage at the extraction meshes was set to $U_{\text{ext}} = \pm 100\,\text{V}$. The TPX3CAM recorded the hits (turquoise) on the electron detector (black circle). Since the single pixels have a dead time of $\geq$465 ns only the first count for each pixel can be resolved in the given time frame of 200 ns.
The central feature in the image corresponds to the electrons ionized via two-photon ionization. The TPX3CAM is able to resolve the different arrival times for the electrons initially moving towards the detector (first counts) and those moving away from it (wing-like structure) on a nanosecond timescale. Since no gated or pulsed detection scheme was used (compare section 2.5.6 and section 2.5.5), a time-resolved spectrum of the arrival times can be reconstructed from a *single* image recorded in a *single* experimental run which immensely simplifies and accelerates the data acquisition.
The high spatial resolution of the ion microscope combined with the high energy resolution of the VMI spectrometer and the possibility to use the detectors in coincidence in combination with the spatiotemporal resolution of the TPX3CAM will enable us to perform time-resolved precision measurements on systems of ions, electrons, Rydberg atoms and ultracold ground state atoms. The VMI spectrometer will give detailed access to the strong-field ionization and excitation cross sections of $^{87}$Rb in femtosecond laser pulses. With the ion microscope, resolution of the interactions between single ions and Rydberg atoms as well as the dynamics of ionized atoms in optical lattices is possible. Using the device in a pulsed manner should enable us to perform precise time-resolved measurements of the expansion dynamics of an ultracold plasma or the ionization dynamics of Rydberg states in these systems, significantly expanding the capabilities of our current experimental setup.

[1] Amsterdam Scientific Instruments TPX3CAM

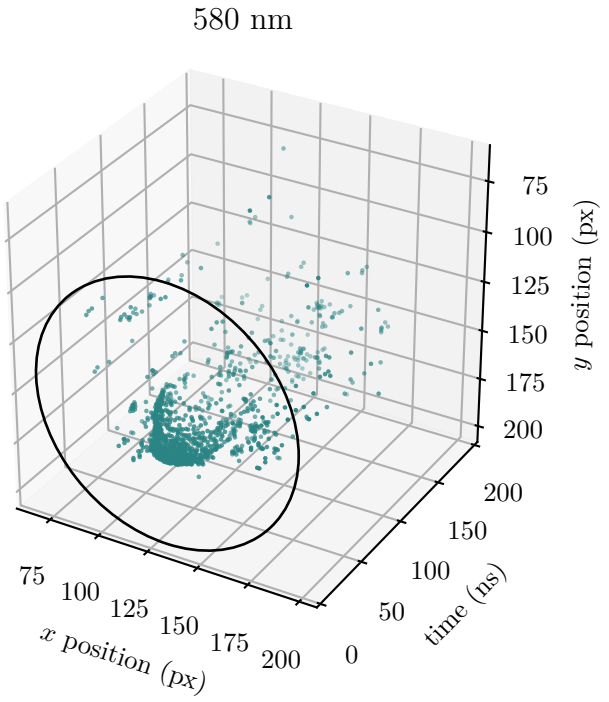


**Fig. 5.2: Example image of the new TPX3 camera.**
A single femtosecond laser pulse at a wavelength of 580 nm is applied to a BEC and the electron signal of the current setup at an extraction voltage of $U_{\text{ext}} = \pm 100\,\text{V}$ is recorded by the TPX3CAM. The black circle marks the extent of the phosphor screen of the electron detector. The central feature shows the electrons ionized by two-photon ionization and shows that the camera is able to resolve their different arrival times without using any gated or pulsed detection scheme in a single run of the experiment.

# A First Appendix

## A.1 Experimental approach to an energy scaling on the electron detector

Extracting electron energies in our experimental setup has proven to be difficult due to the finite overlap between the simulated distributions shown in figure 2.13 and the recorded electron images. Although simulated and recorded images show excellent *qualitative* agreement, discrepancies like a small asymmetry visible in the recorded images (see i.e. figure 4.7a) make quantitative statements on the exact energy challenging.
Therefore, we tried to establish an experimental calibration of the electron energies by recording the cumulated electron signals for electron energies between 0.01 eV to 0.66 eV. To this end we ionized only a few atoms per pulse from a thermal cloud with a peak density of $\rho_{\mathrm{th}} = 2.8 \times 10^{17}\,\mathrm{m}^{-3}$ by misaligning the focus of the femtosecond laser beam to avoid high peak intensities (as discussed in figure 4.2a) at wavelengths between 513 nm to 593 nm in steps of 2.5 nm (corresponding to the bandwidth of the laser pulse). Averaging over 93 experimental cycles with 40 pulses per cycle, a clean detector image of electrons with kinetic energies corresponding to the excess energy of the corresponding two-photon ionization process could be generated this way. The low peak intensity and the ionization of only a few atoms per pulse prevented many-body dynamics like plasma evolution or a reduction of the effective excess energy due to the Coulomb potential of the remaining ion cloud.
Since the area the electron signal occupies on the detector increases monotonically with the kinetic energy of the electrons, we can use the recorded images from this data set to construct an orthonormalized basis set starting from the smallest kinetic energy.
In figure A.1 examples from this generated basis set are shown for electron energies of 0.01 eV, 0.04 eV, 0.15 eV and 0.66 eV. Turquoise areas mark positive contributions while red areas mark negative contributions of the basis vector. Starting from the very slow electrons in the center of the distribution, higher energies are characterized by adding to the outer extent of the structure covered by basis vectors belonging to lower energies. We are then able to use this basis set to create a spectral decomposition of the measured electron distributions $\mathbf{E}_{\mathrm{exp}}$:

$$\mathbf{E}_{\mathrm{exp}} \approx \sum_{i}^{N} \lambda_i \cdot \mathbf{E_i} \tag{A.1}$$

Where $\mathbf{E_i}$ are the orthonormalized basis vectors corresponding to the unique features of a given energy $E_i$ and $\lambda_i$ are the coefficients $\lambda_i = \langle \mathbf{E}_{\mathrm{exp}}, \mathbf{E_i} \rangle$. Figure A.2 shows two examples for spectral decompositions and reconstructions from the basis set in this manner: In figure A.2a a single pulse with a wavelength of 580 nm was applied to a

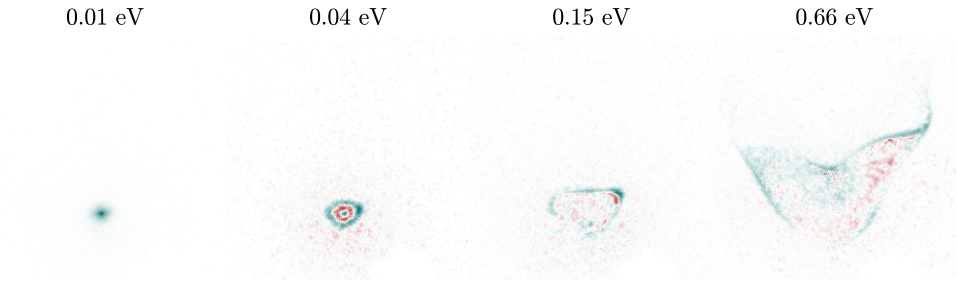


**Fig. A.1: Examples from the generated basis set.**
Basis vectors created from mean detector images for electron energies of 0.01 eV, 0.04 eV, 0.15 eV and 0.66 eV after orthonormalization starting from the lowest energy (turquoise are positive contributions, red are negative contributions). Generated in this way, each basis vector reveals the difference of the visible structure on the detector to the next-lowest energy (e.g. the increase of the area when the kinetic energy increases).

BEC and the recorded electron distribution exhibits slow electrons from plasma dynamics as well as electrons from two-photon ionization (left plot, appearing as a halo around the central dot). In this case the reconstruction (central plot) reproduces all features and looking at the spectral decomposition (right plot), the energies apparent in this distribution are well resolved. Most of the image overlaps with the basis vector corresponding to very low kinetic energies (plasma signature, 0.01 eV), while the free electrons from two-photon ionization appear as a small bump below 0.1 eV.
However, figure A.2b clearly shows the limitations we encountered. In most cases relevant to the experimental work in this thesis, the electron energies span a range from 0.01 eV to 2.2 eV. The basis set we recorded simply did not cover the space spanned by these energies. To this end a larger set could be recorded spanning wavelength from 388 nm to 593.7 nm, covering all kinetic energies from 0.01 eV to 2.2 eV with a two-photon process.
Due to the nature of the basis set which has been generated via orthonormalization starting from the lowest recorded kinetic energy, a signature corresponding to a higher kinetic energy will also feature lower kinetic energies in the spectrum after reconstruction. Not unlike the comparison with the charged particle tracing simulations discussed in figure 2.13, this method can only give an estimate on the upper limit of the kinetic energies resolved.

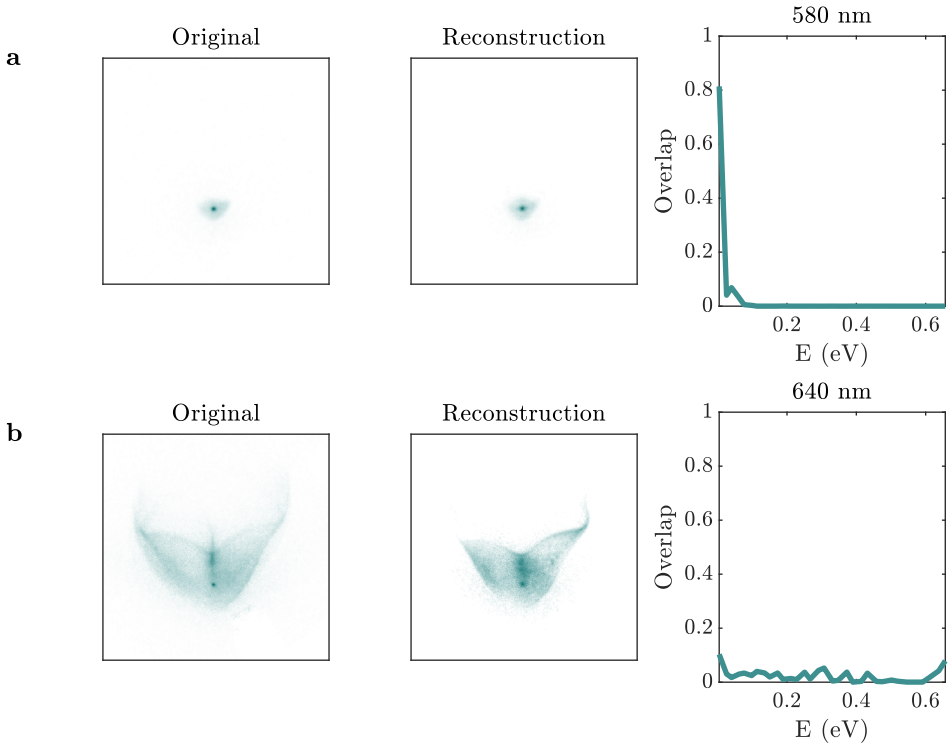


**Fig. A.2: Reconstruction of detector images from the basis set.**
**a.** The original image (left) is an averaged detector image recorded at a pulse wavelength of 580 nm applied to a BEC. Reconstruction (center) is the result of the spectral decomposition and shows excellent agreement, reproducing the electrons from the plasma dynamics (central dot) as well as the free electrons from two-photon ionization. The energy spectrum (right plot) shows the overlap $|\lambda_i|^2$ against the kinetic energy associated with the corresponding basis vector $\mathbf{E_i}$ showing maximum overlap with the lowest kinetic energy (plasma fraction) and a small admixture below 0.1 eV (free electrons from two-photon ionization). **b** For a pulse wavelength of 640 nm with an applied Rydberg ionization pulse from the dipole trap (see section 4.3.3) the averaged image extracted from the experiment exhibits more features: Slow electrons from the plasma dynamics (<0.05 eV), as well as a electrons originating in three-photon ionization (>2 eV), and electrons from Rydberg states ionized via the dipole trap (0.8 eV to 1.2 eV) are visible. Here the reconstruction only covers the slow electrons from the plasma, and part of the feature associated to the electrons from Rydberg excitation, since the basis set only includes energies up to 0.66 eV and does not span the complete space covered by the measurement. For better reconstruction a larger basis set covering higher energies is necessary.

# B Second Appendix

## B.1 Charged particle distribution in a locally ionized ultracold thermal cloud

To estimate the ion distribution when an ultracold thermal cloud is locally ionized, we closely follow the approach in section 3.2.1 replacing the Thomas-Fermi density profile of a BEC $\rho_{\mathrm{TF}}$ with a Gaussian density profile of a thermal ensemble of atoms:

$$\rho_{\mathrm{th}}(x,y,z) = \frac{N}{(2\pi)^{\frac{3}{2}}\sigma_{\mathrm{r}}^3} \cdot \exp\left(\frac{-x^2-y^2-z^2}{2\sigma_{\mathrm{r}}^2}\right) \tag{B.1}$$

where $N$ is the number of atoms and $\sigma_r$ the width of a spherically symmetric cloud. Figure B.1a shows the ion density distribution when a pulse of 590 nm with a waist of 1 µm and a peak intensity of $I_0 = 1.2 \times 10^{14}\,\mathrm{W/cm^2}$ is applied. The thermal cloud was characterized by $N = 2 \cdot 10^5$ and $\sigma_r = 35.2\,\mu\mathrm{m}$ extracted from a representative measurement for a thermal cloud after evaporation in the crossed dipole trap to a final power of the trap to 0.5 W in both axes. In contrast to the cylindrical distribution when a BEC is used as target, here we get an hourglass shape that has a length of approximately 120 µm and a width of 12 µm at its widest position.
Naively, the number of ionized atoms should decrease when the focus of the ionization pulse is shifted along the vertical axis (e.g. along the axis of the femtosecond laser beam) and the overlap between the high intensity volume of the Gaussian beam and the center of the atomic cloud decreases.
This holds true only for low peak intensities as can be seen in figure B.1b. Here the number of ionized atoms is plotted against the vertical position of the femtosecond laser focus $z_0$ in units of the width of the cloud $\sigma_{\mathrm{r}}$ for four different peak intensities. For the highest peak intensities $I_0 = 2.5 \times 10^{14}\,\mathrm{W/cm^2}$, a shift of the focus to $z_0 \approx \sigma_{\mathrm{r}}$ yields the most ions. This has to be considered when the focus height of the femtosecond laser is aligned onto the atomic target - for high peak intensities the optimal overlap between the center of the density profile and the focus of the femtosecond laser beam ($z_0 = 0$) does not coincide with the highest ion count and using the number of detected ions or electrons as an indicator for optimal alignment is thus misleading here.

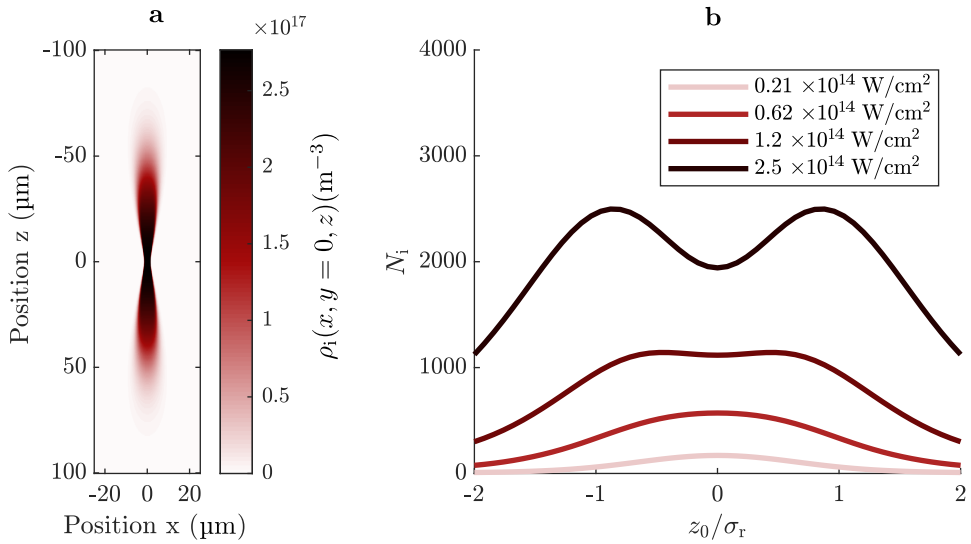


**Fig. B.1: Calculated ion density in a locally ionized thermal cloud.**
**a.** A fraction of a thermal cloud with a density of $\rho_{\mathrm{th}} = 2.8 \times 10^{17}\,\mathrm{m}^{-3}$ is ionized by a single femtosecond pulse with a wavelength of 590 nm and a beam waist of 1 µm at a peak intensity of $I_0 = 1.2 \times 10^{14}\,\mathrm{W/cm}^2$ and the calculated ion density in the central $xz$-plane at $y = 0$ of the atomic cloud is plotted. Darker colors indicate a higher density. In contrast to the cylindrical ion density when a BEC is used as target (see fig. 3.2), here the ion density shows a distinct hourglass shape. **b.** Number of ionized atoms $N_{\mathrm{i}}$ plotted against the vertical position $z_0$ of the focus of the femtosecond laser pulse in respect to the center of the cloud and in units of the cloud radius $\sigma_{\mathrm{r}}$ for peak intensities of $0.21 \times 10^{14}\,\mathrm{W/cm}^2$, $0.62 \times 10^{14}\,\mathrm{W/cm}^2$, $1.2 \times 10^{14}\,\mathrm{W/cm}^2$ and $2.5 \times 10^{14}\,\mathrm{W/cm}^2$. For the two lowest intensities the maximum of the ion yield is achieved, when the center of the cloud and the center of the focus of the femtosecond laser pulse are vertically aligned ($z_0 = 0$). For high peak intensities, a vertical shift of $z_0 \approx \sigma_{\mathrm{r}}$ leads to the highest ion count. This has to be taken into consideration when the focus height of the femtosecond laser beam is aligned onto the target.

## Danksagung

Eine Doktorarbeit in der Experimentalphysik ist nicht ohne Unterstützung einer Vielzahl von Personen möglich und jede noch so ausführliche Danksagung wird wahrscheinlich unvollständig bleiben. Hier aber zumindest ein Versuch:

Mein Dank geht an Klaus Sengstock und Markus Drescher die mit dem *Ultracold and Ultrafast*-Projekt ein wirklich spannendes Kooperationsprojekt ins Leben gerufen haben. Ich bin froh, meine Doktorarbeit genau an diesem Projekt angetreten zu haben. Dadurch, dass ihr beide ein großes Interesse an dem Projekt zeigt, hatte ich als Doktorand das Glück einer echten Doppelbetreuung und habe enorm von eurer Expertise in diesen doch sehr unterschiedlichen Fachgebieten profitiert.

Danken möchte ich auch Juliette Simonet und Philipp Wessels-Staarmann. Ihr leistet in der direkten Koordination und Leitung des Projektes, der Betreuung von Studenten und der wissenschaftlichen Alltagsarbeit wirklich Großes und sorgt darüber hinaus für eine ausgezeichnete Teamatmosphäre. Neben den zahlreichen wertvollen Diskussionen und direkten Hilfestellungen bin ich besonders dankbar, dass ihr euch immer für mich und meine Mitpromovierenden eingesetzt habt und uns damit den Rücken für unsere Forschungsprojekte freigehalten habt.

Des Weiteren danke ich Tobias Kroker, der mit mir die ersten Schritte in Richtung Plasmaphysik an unserem Experiment machte. Unzähligen gemeinsame Stunden im Labor zum Trotz hat die gemeinsame Arbeit viel Freude bereitet.

Dank geht auch an Julian Fiedler für seine wertvolle stoische Genauigkeit, die viele Messungen erst möglich gemacht hat, und an Jette Heyer, die die Zukunft des Experiments geplant hat und auch sonst immer eine gute Idee oder ein gutes Gespräch parat hat. Es hat unheimlich viel Spaß gemacht mit euch beiden zusammenzuarbeiten.

Zudem danke ich den zahlreichen motivierten Bachelor- und Masterstudenten die an unserem Projekt tätig waren - hier insbesondere Linn Hamester, die mit mir den Aufbau für die Graue Melasse in unser Experiment integriert hat.

Weiterer Dank geht an Ellen Gloy und an das CUI-Office, die jegliche administrativen Prozesse erleichtert haben.

Zu guter Letzt danke ich meinen Eltern für ihre Unterstützung in allen Lebenslagen und meiner Frau Jella Großmann.

# Bibliography


[1]M. H. Anderson, J. R. Ensher, M. R. Matthews, C. E. Wieman, and E. A. Cornell, "Observation of Bose-Einstein condensation in a dilute atomic vapor", Science **269**, 198–201 (1995).

[2]C. C. Bradley, C. A. Sackett, J. J. Tollett, and R. G. Hulet, "Evidence of Bose-Einstein condensation in an atomic gas with attractive interactions", Physical Review Letters **75**, 1687–1690 (1995).

[3]K. B. Davis, M. .-. Mewes, M. R. Andrews, N. J. van Druten, D. S. Durfee, D. M. Kurn, and W. Ketterle, "Bose-Einstein condensation in a gas of Sodium atoms", Physical Review Letters **75**, 3969–3973 (1995).

[4]R. P. Feynman, "Simulating physics with computers", International Journal of Theoretical Physics **21**, 467–488 (1982).

[5]M. R. Andrews, C. G. Townsend, H.-J. Miesner, D. S. Durfee, D. M. Kurn, and W. Ketterle, "Observation of Interference Between Two Bose Condensates", Science **275**, 637–641 (1997).

[6]M. R. Andrews, D. M. Kurn, H.-J. Miesner, D. S. Durfee, C. G. Townsend, S. Inouye, and W. Ketterle, "Propagation of Sound in a Bose-Einstein Condensate", Physical Review Letters **79**, 553–556 (1997).

[7]C. Chin, R. Grimm, P. Julienne, and E. Tiesinga, "Feshbach resonances in ultracold gases", Reviews of Modern Physics **82**, 1225–1286 (2010).

[8]M. Saffman, T. G. Walker, and K. Mølmer, "Quantum information with Rydberg atoms", Reviews of Modern Physics **82**, 2313–2363 (2010).

[9]I. Bloch, "Ultracold quantum gases in optical lattices", Nature Physics **1**, 23–30 (2005).

[10]M. Lewenstein, A. Sanpera, V. Ahufinger, B. Damski, A. Sen(De), and U. Sen, "Ultracold atomic gases in optical lattices: mimicking condensed matter physics and beyond", Advances in Physics **56**, 243–379 (2007).

[11]D. Jaksch, C. Bruder, J. I. Cirac, C. W. Gardiner, and P. Zoller, "Cold Bosonic Atoms in Optical Lattices", Physical Review Letters **81**, 3108–3111 (1998).

[12]M. Greiner, O. Mandel, T. Esslinger, T. W. Hänsch, and I. Bloch, "Quantum phase transition from a superfluid to a Mott insulator in a gas of ultracold atoms", Nature **415**, 39–44 (2002).

[13]C. Weitenberg and J. Simonet, "Tailoring quantum gases by Floquet engineering", Nature Physics **17**, 1342–1348 (2021).

[14]W. S. Bakr, J. I. Gillen, A. Peng, S. Fölling, and M. Greiner, "A quantum gas microscope for detecting single atoms in a Hubbard-regime optical lattice", Nature **462**, 74–77 (2009).

[15]J. F. Sherson, C. Weitenberg, M. Endres, M. Cheneau, I. Bloch, and S. Kuhr, "Single-atom-resolved fluorescence imaging of an atomic Mott insulator", Nature **467**, 68–72 (2010).

[16]C. Gross and W. S. Bakr, "Quantum gas microscopy for single atom and spin detection", Nature Physics **17**, 1316–1323 (2021).

[17]L. Asteria, H. P. Zahn, M. N. Kosch, K. Sengstock, and C. Weitenberg, "Quantum gas magnifier for sub-lattice-resolved imaging of 3D quantum systems", Nature **599**, 571–575 (2021).

[18]M. Stecker, H. Schefzyk, J. Fortágh, and A. Günther, "A high resolution ion microscope for cold atoms", New Journal of Physics **19**, 043020 (2017).

[19]C. Veit, N. Zuber, O. A. Herrera-Sancho, V. S. V. Anasuri, T. Schmid, F. Meinert, R. Löw, and T. Pfau, "Pulsed ion microscope to probe quantum gases", Physical Review X **11**, 011036 (2021).

[20]T. Brabec and F. Krausz, "Intense few-cycle laser fields: Frontiers of nonlinear optics", Reviews of Modern Physics **72**, 545–591 (2000).

[21]D. Strickland and G. Mourou, "Compression of amplified chirped optical pulses", Optics Communications **55**, 447–449 (1985).

[22]U. Keller, G. W. 'tHooft, W. H. Knox, and J. E. Cunningham, "Femtosecond pulses from a continuously self-starting passively mode-locked Ti:sapphire laser", Optics Letters **16**, 1022 (1991).

[23]A. H. Zewail, "Laser femtochemistry", Science **242**, 1645–1653 (1988).

[24]A. H. Zewail, "Femtochemistry: Atomic-scale dynamics of the chemical bond", The Journal of Physical Chemistry A **104**, 5660–5694 (2000).

[25]R. Kienberger, E. Goulielmakis, M. Uiberacker, A. Baltuska, V. Yakovlev, F. Bammer, A. Scrinzi, T. Westerwalbesloh, U. Kleineberg, U. Heinzmann, M. Drescher, and F. Krausz, "Atomic transient recorder", Nature **427**, 817–821 (2004).

[26]M. Drescher, M. Hentschel, R. Kienberger, M. Uiberacker, V. Yakovlev, A. Scrinzi, T. Westerwalbesloh, U. Kleineberg, U. Heinzmann, and F. Krausz, "Time-resolved atomic inner-shell spectroscopy", Nature **419**, 803–807 (2002).

[27]M. Y. Ivanov, R. Kienberger, A. Scrinzi, and D. M. Villeneuve, "Attosecond physics", Journal of Physics B: Atomic, Molecular and Optical Physics **39**, R1–R37 (2006).

[28]M. Protopapas, C. H. Keitel, and P. L. Knight, "Atomic physics with super-high intensity lasers", Reports on Progress in Physics **60**, 389–486 (1997).

[29]B. Walker, B. Sheehy, L. F. DiMauro, P. Agostini, K. J. Schafer, and K. C. Kulander, "Precision measurement of strong field double ionization of Helium", Physical Review Letters **73**, 1227–1230 (1994).

[30]P. Lambropoulos, P. Maragakis, and J. Zhang, "Two-electron atoms in strong fields", Physics Reports **305**, 203–293 (1998).

[31]T. Takekoshi, G. M. Brooke, B. M. Patterson, and R. J. Knize, "Absolute Rb one-color two-photon ionization cross-section measurement near a quantum interference", Physical Review A **69**, 053411 (2004).

[32]M. Schuricke, G. Zhu, J. Steinmann, K. Simeonidis, I. Ivanov, A. Kheifets, A. N. Grum-Grzhimailo, K. Bartschat, A. Dorn, and J. Ullrich, "Strong-field ionization of lithium", Physical Review A **83**, 023413 (2011).

[33]P. Wessels, B. Ruff, T. Kroker, A. K. Kazansky, N. M. Kabachnik, K. Sengstock, M. Drescher, and J. Simonet, "Absolute strong-field ionization probabilities of ultracold rubidium atoms", Communications Physics **1**, 32 (2018).

[34]T. Killian, T. Pattard, T. Pohl, and J. Rost, "Ultracold neutral plasmas", Physics Reports **449**, 77–130 (2007).

[35]M. Lyon and S. L. Rolston, "Ultracold neutral plasmas", Reports on Progress in Physics **80**, 017001 (2017).

[36]T. C. Killian, S. Kulin, S. D. Bergeson, L. A. Orozco, C. Orzel, and S. L. Rolston, "Creation of an ultracold neutral plasma", Physical Review Letters (1999).

[37]N. Chamel and P. Haensel, "Physics of neutron star crusts", Living Reviews in Relativity **11**, 10 (2008).

[38]S. Ichimaru, "Strongly coupled plasmas: high-density classical plasmas and degenerate electron liquids", Reviews of Modern Physics **54**, 1017–1059 (1982).

[39]I. Waki, S. Kassner, G. Birkl, and H. Walther, "Observation of ordered structures of laser-cooled ions in a quadrupole storage ring", Physical Review Letters **68**, 2007–2010 (1992).

[40]J. J. Bollinger, J. M. Kriesel, T. B. Mitchell, L. B. King, M. J. Jensen, W. M. Itano, and D. H. E. Dubin, "Laser-cooled ion plasmas in Penning traps", Journal of Physics B: Atomic, Molecular and Optical Physics **36**, 499–510 (2003).

[41]M. Jensen, T. Hasegawa, J. Bollinger, and D. Dubin, "Rapid heating of a strongly coupled plasma near the solid-liquid phase transition", Physical Review Letters **94**, 025001 (2005).

[42]J. H. Chu and L. I, "Direct observation of Coulomb crystals and liquids in strongly coupled rf dusty plasmas", Physical Review Letters **72**, 4009–4012 (1994).

[43]D. Gericke and M. Murillo, "Disorder-induced heating of ultracold plasmas", Contributions to Plasma Physics **43**, 298–301 (2003).

[44]T. K. Langin, G. M. Gorman, and T. C. Killian, "Laser cooling of ions in a neutral plasma", Science **363**, 61–64 (2019).

[45]K. Niffenegger, K. A. Gilmore, and F. Robicheaux, "Early time properties of ultracold neutral plasmas", Journal of Physics B: Atomic, Molecular and Optical Physics **44**, 145701 (2011).

[46]F. Penning, "Die Glimmentladung bei niedrigem Druck zwischen koaxialen Zylindern in einem axialen Magnetfeld", Physica **3**, 873–894 (1936).

[47]W. Paul, "Electromagnetic traps for charged and neutral particles", Reviews of Modern Physics **62**, 531–540 (1990).

[48]D. J. Wineland, R. E. Drullinger, and F. L. Walls, "Radiation-pressure cooling of bound resonant absorbers", Physical Review Letters **40**, 1639–1642 (1978).

[49]W. Neuhauser, M. Hohenstatt, P. E. Toschek, and H. Dehmelt, "Localized visible $Ba^+$ mono-ion oscillator", Physical Review A **22**, 1137–1140 (1980).

[50]D. Wineland and W. M. Itano, "Spectroscopy of a single Mg+ ion", Physics Letters A **82**, 75–78 (1981).

[51]Z. Idziaszek, T. Calarco, P. S. Julienne, and A. Simoni, "Quantum theory of ultracold atom-ion collisions", Physical Review A **79**, 010702 (2009).

[52]T. Dieterle, M. Berngruber, C. Hölzl, R. Löw, K. Jachymski, T. Pfau, and F. Meinert, "Inelastic collision dynamics of a single cold ion immersed in a Bose-Einstein condensate", Physical Review A **102**, 041301 (2020).

[53]A. T. Grier, M. Cetina, F. Oručević, and V. Vuletić, "Observation of cold collisions between trapped ions and trapped atoms", Physical Review Letters **102**, 223201 (2009).

[54]M. Cetina, A. T. Grier, and V. Vuletić, "Micromotion-induced limit to atom-ion sympathetic cooling in Paul traps", Physical Review Letters **109**, 253201 (2012).

[55]J. Joger, H. Fürst, N. Ewald, T. Feldker, M. Tomza, and R. Gerritsma, "Observation of collisions between cold Li atoms and $Yb^+$ ions", Physical Review A **96**, 030703 (2017).

[56]T. Feldker, H. Fürst, H. Hirzler, N. V. Ewald, M. Mazzanti, D. Wiater, M. Tomza, and R. Gerritsma, "Buffer gas cooling of a trapped ion to the quantum regime", Nature Physics **16**, 413–416 (2020).

[57]P. Weckesser, F. Thielemann, D. Wiater, A. Wojciechowska, L. Karpa, K. Jachymski, MichałTomza, T. Walker, and T. Schaetz, "Observation of Feshbach resonances between a single ion and ultracold atoms", Nature **600**, 429–433 (2021).

[58]A. Härter and J. H. Denschlag, "Cold atom–ion experiments in hybrid traps", Contemporary Physics **55**, 33–45 (2014).

[59]M. Tomza, K. Jachymski, R. Gerritsma, A. Negretti, T. Calarco, Z. Idziaszek, and P. S. Julienne, "Cold hybrid ion-atom systems", Reviews of Modern Physics **91**, 035001 (2019).

[60]N. Zuber, V. S. V. Anasuri, M. Berngruber, Y.-Q. Zou, F. Meinert, R. Löw, and T. Pfau, "Observation of a molecular bond between ions and Rydberg atoms", Nature **605**, 453–456 (2022).

[61]T. Dieterle, M. Berngruber, C. Hölzl, R. Löw, K. Jachymski, T. Pfau, and F. Meinert, "Transport of a single cold ion immersed in a Bose-Einstein condensate", Physical Review Letters **126**, 033401 (2021).

[62]C. Zipkes, S. Palzer, C. Sias, and M. Köhl, "A trapped single ion inside a Bose–Einstein condensate", Nature **464**, 388–391 (2010).

[63]S. Schmid, A. Härter, and J. H. Denschlag, "Dynamics of a cold trapped ion in a Bose-Einstein condensate", Physical Review Letters **105**, 133202 (2010).

[64]J. M. Schurer, P. Schmelcher, and A. Negretti, "Ground-state properties of ultracold trapped bosons with an immersed ionic impurity", Physical Review A **90**, 033601 (2014).

[65]J. M. Schurer, A. Negretti, and P. Schmelcher, "Capture dynamics of ultracold atoms in the presence of an impurity ion", New Journal of Physics **17**, 083024 (2015).

[66]G. E. Astrakharchik, L. A. P. Ardila, R. Schmidt, K. Jachymski, and A. Negretti, "Ionic polaron in a Bose-Einstein condensate", Communications Physics **4**, 94 (2021).

[67]T. Secker, R. Gerritsma, A. W. Glaetzle, and A. Negretti, "Controlled long-range interactions between Rydberg atoms and ions", Physical Review A, 10.1103/PhysRevA.94.013420 (2016).

[68]H. Doerk, Z. Idziaszek, and T. Calarco, "Atom-ion quantum gate", Physical Review A **81**, 012708 (2010).

[69]T. Kroker, "Interfacing quantum gases with femtosecond laser pulses: from strong-field ionization to ultracold plasma", PhD thesis (Universität Hamburg, 2021).

[70]C. Bostedt, M. Adolph, E. Eremina, M. Hoener, D. Rupp, S. Schorb, H. Thomas, A. R. B. de Castro, and T. Möller, "Clusters in intense FLASH pulses: ultrafast ionization dynamics and electron emission studied with spectroscopic and scattering techniques", Journal of Physics B: Atomic, Molecular and Optical Physics **43**, 194011 (2010).

[71]T. Gorkhover, M. Adolph, D. Rupp, S. Schorb, S. W. Epp, B. Erk, L. Foucar, R. Hartmann, N. Kimmel, K.-U. Kühnel, D. Rolles, B. Rudek, A. Rudenko, R. Andritschke, A. Aquila, J. D. Bozek, N. Coppola, T. Erke, F. Filsinger, H. Gorke, H. Graafsma, L. Gumprecht, G. Hauser, S. Herrmann, H. Hirsemann, A. Hömke, P. Holl, C. Kaiser, F. Krasniqi, J.-H. Meyer, M. Matysek, M. Messerschmidt, D. Miessner, B. Nilsson, D. Pietschner, G. Potdevin, C. Reich, G. Schaller, C. Schmidt, F. Schopper, C. D. Schröter, J. Schulz, H. Soltau, G. Weidenspointner, I. Schlichting, L. Strüder, J. Ullrich, T. Möller, and C. Bostedt, "Nanoplasma dynamics of single large Xenon clusters irradiated with superintense X-ray pulses from the Linac coherent light source free-electron laser", Physical Review Letters **108**, 245005 (2012).

[72]Y. Kumagai, H. Fukuzawa, K. Motomura, D. Iablonskyi, K. Nagaya, S.-i. Wada, Y. Ito, T. Takanashi, Y. Sakakibara, D. You, T. Nishiyama, K. Asa, Y. Sato, T. Umemoto, K. Kariyazono, E. Kukk, K. Kooser, C. Nicolas, C. Miron, T. Asavei, L. Neagu, M. S. Schöffler, G. Kastirke, X.-j. Liu, S. Owada, T. Katayama, T. Togashi, K. Tono, M. Yabashi, N. V. Golubev, K. Gokhberg, L. S. Cederbaum, A. I. Kuleff, and K. Ueda, "Following the birth of a nanoplasma produced by an ultrashort hard-X-ray laser in Xenon clusters", Physical Review X **8**, 031034 (2018).

[73]N. Takei, C. Sommer, C. Genes, G. Pupillo, H. Goto, K. Koyasu, H. Chiba, M. Weidemüller, and K. Ohmori, "Direct observation of ultrafast many-body electron dynamics in an ultracold Rydberg gas", Nature Communications **7**, 13449 (2016).

[74]G. Vitrant, J. M. Raimond, M. Gross, and S. Haroche, "Rydberg to plasma evolution in a dense gas of very excited atoms", Journal of Physics B: Atomic and Molecular Physics **15**, L49–L55 (1982).

[75]T. F. Gallagher, P. Pillet, M. P. Robinson, B. Laburthe-Tolra, and M. W. Noel, "Back and forth between Rydberg atoms and ultracold plasmas", Journal of the Optical Society of America B **20**, 1091 (2003).

[76]M. Robert-de-Saint-Vincent, C. S. Hofmann, H. Schempp, G. Günter, S. Whitlock, and M. Weidemüller, "Spontaneous Avalanche Ionization of a Strongly Blockaded Rydberg Gas", Physical Review Letters **110**, 045004 (2013).

[77]N. Vanhaecke, D. Comparat, D. A. Tate, and P. Pillet, "Ionization of Rydberg atoms embedded in an ultracold plasma", Physical Review A **71**, 013416 (2005).

[78]J. Heyer, "A coincidence electron velocity map imaging and ion microscopy unit for ultracold atoms", Master thesis (Universität Hamburg, 2021).

[79]B. Ruff, "Ultracold gases in strong light fields of femtosecond laser pulses", PhD thesis (Universität Hamburg, 2017).

[80]M. Schröder, "Entwicklung und Aufbau einer optischen Pinzette für ultrakalte Atome", Bachelor thesis (Universität Hamburg, 2015).

[81]S. Pehmöller, "Aufbau und Test eines bildgebenden Elektronendetektors für Ionisationsexperimente im Laser-Doppelfokus", Bachelor thesis (Universität Hamburg, 2015).

[82]M. S. Neundorf, "Aufbau und Charakterisierung einer 2D-Strahllagenstabilisierung", Bachelor thesis (Universität Hamburg, 2016).

[83]T. Anlauf, "Aktive Magnetfeldkompensation für Photoionisation am ultrakalten Quantengas", Bachelor thesis (Universität Hamburg, 2016).

[84]J. Fiedler, "Aufbau einer Detektoreinheit zum Nachweis von Materiewelleninterferenz langsamer Elektronen", Bachelor thesis (Universität Hamburg, 2017).

[85]J. Heyer, "Abbildungssysteme für Ultrakalte Quantengase", Bachelor thesis (Universität Hamburg, 2018).

[86]D. Imeri, "Eine Detektionseinheit für geladene Teilchen als Schnittstelle zwischen ultrakalten Atomen und Femtosekundenlaserpulsen", Bachelor thesis (Universität Hamburg, 2019).

[87]L. H. Hamester, "Graue Melasse zum Sub-Dopplerkühlen von Rubidium-87", Bachelor thesis (Universität Hamburg, 2020).

[88]H. Krüger, "Aufbau und Charakterisierung einer Hybridfalle für ultrakalte Quantengase", Master thesis (Universität Hamburg, 2015).

[89]T. Kroker, "Photoionisation ultrakalter $^{87}$Rb-Atome in starken Laserfeldern", Master thesis (Universität Hamburg, 2016).

[90]S. Pehmöller, "Aufbau eines abgeschirmten Elektronen und Ionendetektionssystems zur Materiewelleninterferometrie", Master thesis (Universität Hamburg, 2017).

[91]J. Butlewski, "A quantum gas machine for local photoionization of ultracold $^{87}$Rb on ultrafast time-scales", Master thesis (Universität Hamburg, 2018).

[92]M. Pfau, "Aufbau einer Dipolfalle zur Untersuchung von Solitonen in einem Rubidium Bose-Einstein Kondensat", diploma thesis (Universität Hamburg, 2013).

[93]E. L. Raab, M. Prentiss, A. Cable, S. Chu, and D. E. Pritchard, "Trapping of neutral Sodium atoms with radiation pressure", Physical Review Letters **59**, 2631–2634 (1987).

[94]Y.-J. Lin, A. R. Perry, R. L. Compton, I. B. Spielman, and J. V. Porto, "Rapid production of $^{87}$Rb Bose-Einstein condensates in a combined magnetic and optical potential", Physical Review A **79**, 063631 (2009).

[95]D. E. Pritchard, "Cooling neutral atoms in a magnetic trap for precision spectroscopy", Physical Review Letters **51**, 1336–1339 (1983).

[96]V. L. A. Dietz, "Gittermonochromator zum Strecken ultrakurzer Lichtpulse", Bachelor thesis (Universität Hamburg, 2021).

[97]J. Dalibard and C. Cohen-Tannoudji, "Laser cooling below the Doppler limit by polarization gradients: simple theoretical models", Journal of the Optical Society of America B **6**, 2023 (1989).

[98]G. Grynberg and J.-Y. Courtois, "Proposal for a magneto-optical lattice for trapping atoms in nearly-dark states", Europhysics Letters (EPL) **27**, 41–46 (1994).

[99]M. Weidemüller, T. Esslinger, M. A. Ol'shanii, A. Hemmerich, and T. W. Hänsch, "A novel scheme for efficient cooling below the photon recoil limit", Europhysics Letters (EPL) **27**, 109–114 (1994).

[100]D. Boiron, C. Triché, D. R. Meacher, P. Verkerk, and G. Grynberg, "Three-dimensional cooling of cesium atoms in four-beam gray optical molasses", Phys. Rev. A **52**, R3425–R3428 (1995).

[101]T. Esslinger, F. Sander, A. Hemmerich, T. W. Hänsch, H. Ritsch, and M. Weidemüller, "Purely optical dark lattice", Opt. Lett. **21**, 991–993 (1996).

[102]S. Rosi, A. Burchianti, S. Conclave, D. S. Naik, G. Roati, C. Fort, and F. Minardi, "Λ-enhanced grey molasses on the $D_2$ transition of Rubidium-87 atoms", Scientific Reports (2018).

[103]A. T. Grier, I. Ferrier-Barbut, B. S. Rem, M. Delehaye, L. Khaykovich, F. Chevy, and C. Salomon, "Λ-enhanced sub-Doppler cooling of lithium atoms in $D_1$ gray molasses", Phys. Rev. A **87**, 063411 (2013).

[104]D. Steck, "Rubidium 87 D Line Data, available online at http://steck.us/alkalidata (revision 2.2.2, 9 July 2021)", (2001).

[105]J. Bergmann, "Rydberg dressing of a Bose-Einstein condensate for the trapping of a single ion", Master thesis (Universität Hamburg, 2020).

[106]T. Kroker, M. Großmann, K. Sengstock, M. Drescher, P. Wessels-Staarmann, and J. Simonet, "Ultrafast electron cooling in an expanding ultracold plasma", Nature Communications **12**, 596 (2021).

[107]M. Krems, J. Zirbel, M. Thomason, and R. D. DuBois, "Channel electron multiplier and channelplate efficiencies for detecting positive ions", Review of Scientific Instruments **76**, 093305 (2005).

[108]*COMSOL Multiphysics® v. 5.4. www.comsol.com. COMSOL AB, Stockholm, Sweden.*

[109]G. LEUCHS and H. WALTHER, "5 - Angular distribution of photoelectrons and light polarization effects in multiphoton ionization of atoms", in *Multiphoton Ionization of Atoms*, edited by S. CHIN and P. LAMBROPOULOS (Academic Press, 1984), pp. 109–132.

[110]T. C. Killian and S. L. Rolston, "Ultracold neutral plasmas", Physics Today **63**, 46–51 (2010).

[111]D. Ciampini, M. Anderlini, J. H. Müller, F. Fuso, O. Morsch, J. W. Thomsen, and E. Arimondo, "Photoionization of ultracold and Bose-Einstein-condensed Rb atoms", Physical Review A **66**, 043409 (2002).

[112]L. Pitaevskii and S. Stringari, *Bose-Einstein Condensation*, International Series of Monographs on Physics (Clarendon Press, 2003).

[113]P. McQuillen, T. Strickler, T. Langin, and T. C. Killian, "Ion temperature evolution in an ultracold neutral plasma", Physics of Plasmas **22**, 033513 (2015).

[114]W. Li, M. W. Noel, M. P. Robinson, P. J. Tanner, T. F. Gallagher, D. Comparat, B. L. Tolra, N. Vanhaecke, T. Vogt, N. Zahzam, P. Pillet, and D. A. Tate, "Evolution dynamics of a dense frozen Rydberg gas to plasma", Physical Review A **70**, 042713 (2004).

[115]T. C. Killian, M. J. Lim, S. Kulin, R. Dumke, S. D. Bergeson, and S. L. Rolston, "Formation of Rydberg atoms in an expanding ultracold neutral plasma", Physical Review Letters **86**, 3759–3762 (2001).

[116]N. Šibalić, J. Pritchard, C. Adams, and K. Weatherill, "ARC: An open-source library for calculating properties of alkali Rydberg atoms", Computer Physics Communications **220**, 319–331 (2017).

[117]L. G. Silvestri, L. J. Stanek, G. Dharuman, Y. Choi, and M. S. Murillo, "Sarkas: A fast pure-python molecular dynamics suite for plasma physics", Computer Physics Communications **272**, 108245 (2022).

[118]W. C. Swope, H. C. Andersen, P. H. Berens, and K. R. Wilson, "A computer simulation method for the calculation of equilibrium constants for the formation of physical clusters of molecules: Application to small water clusters", The Journal of Chemical Physics **76**, 637–649 (1982).

[119]S. Hamaguchi, R. T. Farouki, and D. H. E. Dubin, "Phase diagram of Yukawa systems near the one-component-plasma limit revisited", The Journal of Chemical Physics **105**, 7641–7647 (1996).

[120]M. K. Warrens, G. M. Gorman, S. J. Bradshaw, and T. C. Killian, "Expansion of ultracold neutral plasmas with exponentially decaying density distributions", Physics of Plasmas **28**, 022110 (2021).

[121]M. Mizoguchi, Y. Zhang, M. Kunimi, A. Tanaka, S. Takeda, N. Takei, V. Bharti, K. Koyasu, T. Kishimoto, D. Jaksch, A. Glaetzle, M. Kiffner, G. Masella, G. Pupillo, M. Weidemüller, and K. Ohmori, "Ultrafast creation of overlapping Rydberg electrons in an atomic BEC and Mott-insulator lattice", Physical Review Letters **124**, 253201 (2020).

[122]A. Punnoose and A. M. Finkel'stein, "Metal-insulator transition in disordered two-dimensional electron systems", Science **310**, 289–291 (2005).

[123]A. Y. Kuntsevich, Y. V. Tupikov, V. M. Pudalov, and I. S. Burmistrov, "Strongly correlated two-dimensional plasma explored from entropy measurements", Nature Communications **6**, 7298 (2015).

[124]Y. Chew, T. Tomita, T. P. Mahesh, S. Sugawa, S. de Léséleuc, and K. Ohmori, "Ultrafast energy exchange between two single Rydberg atoms on a nanosecond timescale", Nature Photonics **16**, 724–729 (2022).

[125]J. Frohn, "Optischer Aufbau zur Erzeugung eines sub-Mikrometer Doppelfokus", Bachelor thesis (Universität Hamburg, 2014).

[126]J. Fiedler, "Lasersystem zum Rydberg-Dressing eines Bose-Einstein-Kondensats", Master thesis (Universität Hamburg, 2020).

[127]A. T. J. B. Eppink and D. H. Parker, "Velocity map imaging of ions and electrons using electrostatic lenses: Application in photoelectron and photofragment ion imaging of molecular oxygen", Review of Scientific Instruments **68**, 3477–3484 (1997).

[128]M. Anwar, M. Wieland, and M. Drescher, "A THz streak camera based on a highly efficient velocity map imaging spectrometer in collinear geometry", Measurement Science and Technology **31**, 035901 (2020).

[129]K. Fehre, D. Trojanowskaja, J. Gatzke, M. Kunitski, F. Trinter, S. Zeller, L. P. H. Schmidt, J. Stohner, R. Berger, A. Czasch, O. Jagutzki, T. Jahnke, R. Dörner, and M. S. Schöffler, "Absolute ion detection efficiencies of microchannel plates and funnel microchannel plates for multi-coincidence detection", Review of Scientific Instruments **89**, 045112 (2018).